Thermodynamic Optimization of Evaporators with Zeotropic Refrigerant Mixtures

F. Ragazzi and C. O. Pedersen

ACRC TR-74

April 1995

For additional information:

Air Conditioning and Refrigeration Center
University of Illinois
Mechanical & Industrial Engineering Dept.
1206 West Green Street
Urbana, IL 61801

(217) 333-3115

Prepared as part of ACRC Project 29
Experimental Breadboard for Testing Residential
Air Conditioning Systems Using R-22 Alternatives
C. O. Pedersen, Principal Investigator

The Air Conditioning and Refrigeration Center was founded in 1988 with a grant from the estate of Richard W. Kritzer, the founder of Peerless of America Inc. A State of Illinois Technology Challenge Grant helped build the laboratory facilities. The ACRC receives continuing support from the Richard W. Kritzer Endowment and the National Science Foundation. The following organizations have also become sponsors of the Center.

Acustar Division of Chrysler
Amana Refrigeration, Inc.
Brazeway, Inc.
Carrier Corporation
Caterpillar, Inc.
Delphi Harrison Thermal Systems
E. I. du Pont de Nemours & Co.
Eaton Corporation
Electric Power Research Institute
Ford Motor Company
Frigidaire Company
General Electric Company
Lennox International, Inc.
Modine Manufacturing Co.
Peerless of America, Inc.
U. S. Army CERL
U. S. Environmental Protection Agency
Whirlpool Corporation

For additional information:

Air Conditioning & Refrigeration Center
Mechanical & Industrial Engineering Dept.
University of Illinois
1206 West Green Street
Urbana IL 61801

217 333 3115

THERMODYNAMIC OPTIMIZATION OF EVAPORATORS WITH ZEOTROPIC REFRIGERANT MIXTURES

Franco Ragazzi, Ph.D.
Department of Mechanical and Industrial Engineering
University of Illinois at Urbana-Champaign, 1995
C.O. Pedersen, Advisor

A study was conducted to determine the influence of heat exchanger design on the performance of residential air-conditioning systems using zeotropic mixtures as HCFC-22 alternatives.

A computer simulation of the evaporator was developed to model various evaporator designs, and was validated with experimental data collected under controlled air and refrigerant conditions with both HCFC-22 and a zeotropic mixture of HFC-32/HFC-134a/HFC-125 (23%/52%/25%). The model predictions of heat transfer, pressure drop, and temperature profiles were in very good agreement with the experimental data.

An effectiveness-type model for combined heat and mass transfer was developed and implemented in the simulation, resulting in increased computational speed and stability. The model was compared to two others in the literature, and their predictions of the total rate of heat transfer were found to be in reasonable agreement. A discretized solution of the differential heat and mass transfer equations resulted in the best latent load predictions.

An irreversibility-based objective function, chosen to quantify evaporator thermodynamic performance, showed a clear dependency on design and operating conditions. A trade-off between irreversibilities due to heat transfer and air pressure drop was found with an increasing number of exchanger rows, and the presence of a minimum suggested a possible optimum design. The effects of refrigerant circuitry and glide matching on exchanger performance were also investigated.

Finally, a link was established between the second-law optimization of the evaporator and its actual performance in a full air-conditioning system. The evaporator model was implemented in a system simulation, and its thermodynamic performance was found to

significantly affect that of other components under certain operating conditions. A complete analysis of the interaction between all system irreversibilities is recommended, based on the results of this study.

TABLE OF CONTENTS

LIST OF TABLES

LIST OF FIGURES

NOMENCLATURE

CHAPTER 2

General Variables

Variable	Description	IP Units	SI Units
COP	System Coefficient of Performance	-	-
COP^*	Modified System Coefficient of Performance	-	-
Q_E	Evaporator Capacity	Btu	J
UA_E	Evaporator Conductance	Btu/hr.°F	W/K
UA_C	Condenser Conductance	Btu/hr.°F	W/K
$\overline{T}_{ref,E}$	Mean Refrigerant Evaporator Temperature	°F	°C
$\overline{T}_{ref,C}$	Mean Refrigerant Condenser Temperature	°F	°C
$\overline{T}_{air,E}$	Mean Air Evaporator Temperature	°F	°C
$\overline{T}_{air,C}$	Mean Air Condenser Temperature	°F	°C
MTD_E	Evaporator Mean Temperature Difference	°F	°C
MTD_C	Condenser Mean Temperature Difference	°F	°C
F	LMTD-Correction Factor	-	-

CHAPTER 3

General Variables

Variable	Description	IP Units	SI Units
t	Time	s	s
V	Volume	ft^3	m^3
P	Pressure	psi	Pa
T	Temperature	°F	°C
v	Fluid Velocity	ft/s	m/s
$\dot{m}$	Fluid Mass Flowrate	lb/hr	kg/s
h	Specific Fluid Enthalpy	Btu/lb	J/kg
h^o	Specific Fluid Methalpy	Btu/lb	J/kg
s	Specific Fluid Entropy	Btu/lb.R	J/kg.K

Variable	Description	IP Units	SI Units
e	Specific Fluid Exergy	Btu/lb	J/kg
E	Total Exergy of the Control Volume	Btu	J
S	Total Entropy of the Control Volume	Btu/R	J/K
$\dot{Q}_i$	Rate of Heat Transfer from Reservoir 'i'	Btu/hr	W
T_i	Temperature of Reservoir 'i'	R	K
$\dot{W}$	Rate of Work Transfer	Btu/hr	W
$\dot{W}_{electric}$	Rate of Electric Work Transfer	Btu/hr	W
P_0	Dead State Pressure	psi	Pa
T_0	Dead State Temperature	R	K
ϕ_0	Dead State Relative Humidity	-	-
$\dot{W}_{rev}$	Rate of Reversible Work Transfer	Btu/hr	W
$\dot{W}_{lost}$	Rate of Lost Available Work	Btu/hr	W
$\dot{S}_{gen}$	Rate of Entropy Generation	Btu/hr.R	W/K
$\dot{E}_w$	Rate of Available Work	Btu/hr	W
$\dot{E}_{w,rev}$	Maximum Rate of Available Work	Btu/hr	W
$\dot{E}_{w,lost}$	Lost Rate of Available Work	Btu/hr	W
Q_C	Load from the Cold Room	Btu/cycle	J/cycle
Q_H	Load to the Hot Room	Btu/cycle	J/cycle
W	Work per Cycle	Btu/cycle	J/cycle
T_C	Temperature of the Cold Room	R	K
T_H	Temperature of the Hot Room	R	K
W_{lost}	Lost Work per Cycle	Btu/cycle	J/cycle
E_{Q_L}	Available Work (Exergy) Content of the Heat Transfer Interaction	Btu/cycle	J/cycle
E_w	Available Work (Exergy) Content of the Work Transfer Interaction	Btu/cycle	J/cycle
$E_{w,rev}$	Available Work (Exergy) Content of the Reversible Work Transfer Interaction	Btu/cycle	J/cycle
S_{gen}	Entropy Generation per Cycle	Btu/R.cycle	J/K.cycle
η_{2nd}	Relative Second Law Efficiency	-	-
COP_{cycle}	System Coefficient of Performance for an Air-Conditioning Cycle	-	-
$\dot{Q}$	Rate of Heat Transfer from Hot to Cold Reservoir	Btu/hr	W
$\dot{B}$	Rate of work Produced by a Reversible Engine and Dissipated by a Brake	Btu/hr	W

Variable	Description	IP Units	SI Units
$\dot{W}_{lost}$	Rate of Loss of Available Work	Btu/hr	W
$\dot{C}_{min}$	Minimum Capacity Rate	Btu/hr.°F	W/K
$N_{s,min}$	Entropy Generation Number	-	-
N_Q	Entropy Generation Number	-	-
N_M	Entropy Generation Number	-	-
$HERN$	Heat Exchanger Reversibility Norm	-	-
$\varepsilon_{Reistad}$	Second Law Exchanger Effectiveness	-	-
ε_{Witte}	Second Law Exchanger Effectiveness	-	-

Subscripts

Symbol	Description
air	Air
moist air	Moist Air
condensate	Evaporator Condensate
ref	Refrigerant
in	Inlet to the Control Volume
out	Outlet to the Control Volume

CHAPTER 4

General Variables

Variable	Description	IP Units	SI Units
$\dot{m}$	Fluid Mass Flowrate	lb/hr	kg/s
P	Pressure	psi	Pa
T	Temperature	°F	°C
h, i	Enthalpy	Btu/lb	J/kg
ω	Humidity Ratio	-	-
$c_{p,a}$	Air Specific Heat	Btu/lb.°F	J/kg.K
i_{fg}	Latent Heat of Vaporization of Water	Btu/lb	J/kg
dA	Surface Area of a Discretized Element	ft^2	m^2
h_{ref}	Refrigerant Side Heat Transfer Coefficient	$Btu/hr.ft^2.°F$	$W/m^2.K$
h_a	Air Side Heat Transfer Coefficient	$Btu/hr.ft^2.°F$	$W/m^2.K$
h_D	Air Side Mass Transfer Coefficient	$lb/hr.ft^2$	$kg/s.m^2$

Variable	Description	IP Units	SI Units
η_{fin}	Fin Efficiency	-	-
$\eta_{s,T}$	Surface Efficiency Related to the Fin Temperature Distribution	-	-
$\eta_{s,\omega}$	Surface Efficiency Related to the Fin Humidity Ratio Distribution	-	-
ΔP_{calc}	Refrigerant Pressure Drop within a Discretized Element	psi	Pa
Le	Lewis Number	-	-
dq	Rate of Heat Transfer for a Discretized Element	Btu/hr	W
R	Resistance to Heat Transfer	hr.°F/Btu	K/W
U	Total Heat Transfer Conductance	Btu/hr.ft^2.°F	W/m^2.K
ε_{wet}	Equivalent Effectiveness (Sensible and Latent Effects)	-	-
j_f	Air Side J-Factor	-	-
St	Stanton Number	-	-
Pr	Prandtl Number	-	-
Re	Reynolds Number	-	-
G	Mass Flux	lb/hr.ft^2	kg/s.m^2

Subscripts

Symbol	Description
ref, r	Refrigerant
air, a	Air
ma	Moist Air
tube	Tube Wall
fin	Fin Surface
total	Total Heat Transfer Surface
ri, ro	Refrigerant Inlet/ Outlet
ai, ao	Air Inlet/ Outlet
s	Condensate Film Saturated Conditions
w	Water
wv	Water Vapor
i, o	Inside/ Outside
f	Fin

Symbol	Description
eff	Effective (Sensible and Latent Effects)
wet	Wet
max	Maximum
actual	Actual
mixed	Mixed Fluid Stream
unmixed	Unmixed Fluid Stream

Superscripts

Symbol	Description
-	Average Value

CHAPTER 5

General Variables

Variable	Description	IP Units	SI Units
$\dot{m}$	Fluid Mass Flowrate	lb/hr	kg/s
P	Pressure	psi	Pa
ΔP	Pressure Change	psi	Pa
T	Temperature	°F	°C
ΔT	Temperature Change	°F	°C
x	Quality	-	-
h	Enthalpy	Btu/lb	J/kg
ω	Humidity Ratio	-	-
ϕ	Relative Humidity	-	-
$c_{p,a}$	Air Specific Heat	Btu/lb.°F	J/kg.K
i_{fg}	Latent Heat of Vaporization of Water	Btu/lb	J/kg
$\dot{Q}$	Rate of Heat Transfer	Btu/hr	W
E	Error Term	%	%
$\dot{W}_k$	Compressor Work	W	W
COP	System Coefficient of Performance	-	-

Subscripts

Symbol	Description
r	Refrigerant
a	Air
L, s	Latent/ Sensible
c	Condensate
a + c	Air and Condensate
ref	Reference
sc, sh	Sub-Cooling/ Superheat
e	Evaporator
ei, eo	Evaporator Inlet/ Outlet
vi	Expansion Valve Inlet
sc o	Sub-Cooler Outlet
dew	Dew Conditions
bubble	Bubble Conditions

Superscripts

Symbol	Description
-	Average Value

CHAPTER 6

General Variables

Variable	Description	IP Units	SI Units
$\dot{m}$	Fluid Mass Flowrate	lb/hr	kg/s
P	Pressure	psi	Pa
T	Temperature	°F	°C
ΔT	Temperature Change	°F	°C
h	Specific Fluid Enthalpy	Btu/lb	J/kg
s	Specific Fluid Entropy	Btu/lb.°F	J/kg.K
e	Specific Fluid Exergy	Btu/lb	J/kg
$\dot{Q}$	Rate of Heat Transfer from Reservoir 'j'	Btu/hr	W
T_0	Dead State Temperature	R	K

Variable	Description	IP Units	SI Units
$\dot{S}_{gen}$	Rate of Entropy Generation	Btu/hr.R	W/K
$\dot{S}_{g,\Delta T}$	Rate of Entropy Generation (Heat Transfer across Finite Temperature Differences)	Btu/hr.R	W/K
$\dot{S}_{g,\Delta P_{ref}}$	Rate of Entropy Generation (Refrigerant Pressure Drop)	Btu/hr.R	W/K
$\dot{S}_{g,\Delta P_{air}}$	Rate of Entropy Generation (Air Pressure Drop)	Btu/hr.R	W/K
$\dot{S}_{g,mix}$	Rate of Entropy Generation (Air Mixing)	Btu/hr.R	W/K

Subscripts

Symbol	Description
r, ref	Refrigerant
a, air	Air
i, o	Inlet/ Outlet
ev, e	Evaporator
sh	Superheat
set	Set Value
mod	Model Output

Superscripts

Symbol	Description
-	Average Value

CHAPTER 1
INTRODUCTION

This project was undertaken as part of a research effort by the air-conditioning industry to investigate the replacement of HCFC-22 (chlorodifluoromethane) in residential air-conditioning systems with zeotropic refrigerant mixtures. The goal of the study was to evaluate changes in heat exchanger design aimed at improving the energy efficiency of existing systems. The first part of this chapter discusses the need to replace HCFC-22, and describes the selection of a potential substitute. The remaining sections of this introduction focus on the specific objectives of the project and trace the outline of subsequent chapters.

1.1 Environmental Concerns

HCFC-22 is a hydrochlorofluorocarbon whose release into the atmosphere causes destruction of the ozone layer and contributes to the greenhouse effect. The former is an atmospheric layer within the stratosphere in which there is an appreciable concentration of ozone (O_3), an allotropic form of oxygen which filters potentially hazardous ultra-violet radiation from the Sun [1]. It extends from a medium height of 10 to 20 km, reaching 20 to 30 km above the Equator, and has medium annual ozone concentrations ranging from 200 to 400 Dobson units. The erosion of the ozone layer has caused great environmental concern in recent years, particularly when record levels were detected over Antartica by the National Aeronautics and Space Administration in October of 1991 [2]. Even though the link between chlorinated compounds and ozone depletion has become more widely accepted in recent years, the causes responsible and the degree of its severity are a continuing source of controversy. An alternative explanation for fluctuations in the ozone level, put forward by those with a dissenting view, is based on natural, cyclic solar activity.

Whereas ozone depletion has dominated the debate over CFCs, global warming is beginning to play an increasing role in the proposed phase-out of HCFCs. In contrast to ozone depletion, global warming is questioned at its roots. Many do not recognize the occurrence of the phenomenon itself, let alone its man-made causes. What follows is a brief overview of the main sources of contempt with the current global warming theory as presented by one of its most outspoken critics [3].

Certain atmospheric gases, notably water vapor and carbon dioxide, have the capacity to absorb infrared radiation. Global warming is based on the assumption that as the atmospheric concentration of these gases rises, an increasing portion of the earth's radiation that would normally pass directly out of the lower atmosphere is instead redirected downward [3]. The correlation between CO_2 atmospheric concentration and mean surface temperature was originally estimated by Arrhenius in 1896 [4].

Since then, a variety of climate models with increasing sophistication have been developed. Criticism of earlier models was directed at the calculation of cloudiness as a climate control mechanism, as well as the abrupt increases in CO_2 concentration imposed for simulation purposes [3]. Even though those issues have been addressed, with the finding that the current mix of clouds exerts a cooling effect on the atmosphere [5], the profound discrepancy between forecasts and measurements is typically presented as proof of their unreliability.

The measurements themselves are also questioned. Confounding influences, such as industry and urbanization may be responsible for some of the warming observed, a criticism which has led to the collection of temperature data in isolated locations [6]. Some of these measurements have shown evidence of increasing cloudiness, a preeminence of night warming, and reduced or negative daytime warming.

A possible explanation for the overestimation of warming projections is based on the observed increased cloudiness [3]. If the greenhouse effect traps radiation that would otherwise leave, this should result in a cooling of the upper atmosphere. Because the models over predict the altitude at which this cooling takes place, such that there is little water vapor present, they end up under predicting the degree of cloud formation.

The preponderance of night over daytime warming is also used to attack the warming predictions. Night warming, the argument goes, would have beneficial side-effects such as increased plant growth. In addition, the combination of night warming with reduced or negative daytime warming would result in smaller daily temperature variations, a desirable effect [3].

Given the uncertainty in both the models and the experimental measurements used for their validation, in addition to the abundance and complexity of weather control mechanisms, the debate over this subject is not likely to subside in the near future. Its nature, however, is rapidly changing as the policies chosen to address the issue begin to take effect.

1.2 Replacement of HCFC-22

In response to the environmental concerns discussed above, the Montreal Protocol was signed in 1987 by twenty-four countries and the European Community to phase-out ozone-depleting, global-warming substances and to find suitable replacements [3]. CFC refrigerants were high on the list because of their significant *Ozone Depletion Potential* (*ODP*) and *Global Warming Potential* (*GWP*) values, two previously established scales used to compare the environmental impact of various refrigerants. HCFC-22, also a chlorinated compound, has a much lower *ODP* but is still undesirable due to its *GWP*.

Several factors are taken into account in the calculation of these values. The ozone depletion potential is typically a function of the amount of chlorine and bromine in a compound. The global warming potential, on the other hand, depends on its infrared absorption spectrum and atmospheric lifetime, which dictates the altitude at which it would break down if released.

The energy efficiency of the systems which use these refrigerants is also of great importance. Poor system efficiency causes secondary greenhouse effects through the release of additional carbon dioxide, assuming the combustion of fossil fuel to be the primary source of energy. The *Total Equivalent Warming Index* (*TEWI*) has been defined in order to account for both direct and indirect global warming effects. Thus energy efficiency is particularly important with HCFC-22, given that indirect effects account for 73% and 65% of the total global warming effects in commercial chillers and household refrigeration respectively [8].

Originally scheduled for the year 2020 in developed countries by the Montreal Protocol, the phase-out of HCFCs is likely to be accelerated in the United States. Following the encouraging progress of the CFC phase-out, the European Union has moved its own deadline up to 2015 [9]. In this country, the Clean Air Act of 1990 has designated 2010 and 2020 as the dates for the production phase-out of HCFC-22 for new and servicing equipment respectively [8].

1.3 HCFC-22 Alternatives

Zeotropic blends, also known as *NARMs* (non-azeotropic refrigerant mixtures), have long been proposed as a possible substitute. They figure prominently in the list of refrigerants compiled by the ARI (American Refrigeration Institute) for the *R22 Alternative Refrigerants Evaluation Program* and have been the subject of numerous theoretical and experimental studies [10].

Zeotropes are attractive because of their low *ODP* and *GWP*, as well as their promising thermodynamic characteristics which could improve cycle efficiency. A zeotropic mixture experiences a variable temperature glide during an isobaric phase change. Under ideal circumstances, this could lead to a better match between the temperature profiles of the refrigerant and the external fluid, reducing heat exchanger irreversibilities and therefore increasing system performance.

To optimize a refrigeration system using zeotropic blends, however, it is necessary to conduct a thorough pinch point analysis for appropriate heat exchanger sizing [11]. The methodology for such an optimization is still in the early stages of development and is considered in this study.

1.4 Objective of Research

The purpose of this project was to investigate the effect of evaporator design changes on its performance. An irreversibility-based function was selected to quantify the penalties associated with various designs, and was evaluated with a computer simulation of the evaporator developed as part of this study. Several combined heat and mass transfer models were implemented in the simulation program, and experimental data was collected for two different coil designs, with pure and mixed refrigerants, in order to validate the model predictions.

1.5 References

1 Webster's New World Dictionary, Third College Edition, 1991.

2 "Ozone Loss Hits Us Where We Live", News & Comment , November 1, 1991, p.645.

[3] Michaels, P.J., “Global Warming: Failed Forecasts and Politicized Science”, Waste Management , Vol.14, No.2, pp.89-95, 1994.

[4] Arrhenius, S., “On the Influence of Carbonic Acid in the Air upon the Temperature of the Ground”, Philosoph. Magazine 41: 237-276, 1896.

[5] Ramanathan, V., et al., “Cloud-radiative Forcing and Climate: Results from the Earth Radiation Budget Experiments”, Science 243: 57-63, 1989.

[6] Bucher, A. and Dessens, J., “Secular Trend of Surface Temperature at an Elevated Observatory in the Pyrenees”, J. Climate 4: 859-868, 1991.

[7] United Nations Environmental Programme, “Montreal Protocol on substances that deplete the Ozone Layer. Final Act.”, New York: United Nations, 1987.

[8] Hourahan, G., American Refrigeration Institute (ARI), Short Course: World-wide Experiences in Using New Refrigerants, Purdue University, July 1994.

[9] Kuijpers, L., Technical University of Eiudhoven, Short Course: World-wide Experiences in Using New Refrigerants, Purdue University, July 1994.

[10] AREP- R-22 alternative refrigerants evaluation program (AREP) participants handbook, Arlington, VA: Air Conditioning and Refrigeration Institute, 1992.

[11] Didion, P.A., and D.B. Bivens, "Role of mixtures as alternatives to CFCs", International Journal of Refrigeration 13, May 1990.

[12] Didion, P.A., National Institute of Standards and Technology, Short Course: World-wide Experiences in Using New Refrigerants, Purdue University, July 1994.

CHAPTER 2
ZEOTROPES AND THE VAPOR COMPRESSION CYCLE

This chapter is divided into three sections. The first section covers the basic thermodynamics of zeotropes, and their relation to the vapor compression cycle. The second section reviews the mixture literature, and discusses the potential advantages and disadvantages of using zeotropes. Finally, the third section reviews the literature on the modeling and experimental testing of zeotrope performance in vapor compression systems.

2.1 Zeotrope Thermodynamics and the Vapor Compression Cycle

2.1.1 Zeotropic versus Azeotropic Mixtures

The majority of the refrigerants currently in use are pure fluids, such as HCFC-22, or so-called azeotropic mixtures of two or more fluids. Pure refrigerants differ from mixtures in that their temperature remains constant while undergoing an isobaric phase change. Mixtures of two or more refrigerants of differing boiling points, on the other hand, are characterized by a temperature glide during a similar phase change. Certain refrigerant mixture combinations exhibit nearly isothermal behavior during constant-pressure phase change for a specific bulk concentration. Depending on the magnitude of their temperature glides, mixtures are classified as azeotropic and non-azeotropic, or simply zeotropic .

The mechanisms responsible for the temperature glide of mixtures are typically explained with the help of a temperature versus concentration diagram [1]. Figure 2.1 shows such a phase-diagram for an arbitrary binary mixture with a maximum boiling-point azeotrope.

For a typical bulk concentration X_Z, this mixture exhibits zeotropic behavior. As its temperature is varied within the range of the liquid/ vapor envelope (two-phase region), the concentration of the liquid and vapor vary while the bulk concentration X_Z remains constant. During an evaporation process, the more volatile component, A, will evaporate more readily, increasing its concentration in the vapor phase. The resulting enrichment of the less volatile component, B, in the liquid phase, increases the boiling point of the liquid. The shift in the boiling point of the remaining liquid phase is the temperature glide for the mixture.

The mixture shown in Figure 2.1 is special in that it exhibits azeotropic behavior for a particular bulk concentration, X_A. Most azeotropic mixtures have a boiling point greater than that of its components. In some cases, the azeotropic boiling point may be lower than that of its components, but never in-between [2].

Arguments similar to those used in the discussion of a binary mixture apply to mixtures with three or more components. The size of the maximum temperature glide for a given refrigerant combination depends on the relative magnitudes of the boiling points of its components. In addition, the observed temperature glide is a function of bulk composition and refrigerant pressure.

The relation between the boiling points of the mixture components influences the temperature profile of the zeotropic phase change, as well as its endpoints. Temperature non-linearities associated with binary mixtures with a dominant low or high boiling point refrigerant may be corrected with the addition of a third component having a boiling point in-between that of the two original components. This effect has been investigated with the goal of reducing pinch-points in heat exchangers resulting from non-linearities in the temperature profile of zeotropic refrigerant mixtures [3]. Pinch-points occur when the temperature difference between the two fluids is reduced to zero or becomes negative. Figure 2.2 shows a conceptual view of mixture temperature non-linearity for an arbitrary refrigerant mixture.

2.1.2 Ideal Reversible Thermodynamic Cycles

Ideal cycles are typically used to evaluate the performance of a given refrigerant as the working fluid in a vapor-compression refrigeration system. The corresponding cycle for no-glide refrigerants is the Carnot cycle, an ideal reversible thermodynamic cycle operating between isothermal reservoirs. The Lorenz cycle, also an ideal reversible thermodynamic cycle but operating between non-isothermal reservoirs, is used for zeotropic refrigerant blends. Figure 2.3 shows the temperature-entropy diagrams for the two cycles with the corresponding external fluid temperature profiles.

An advantage of looking at temperature-entropy diagrams is that the areas associated with various refrigerant processes directly correspond to the amounts of heat and work transferred to and from the refrigerant system. The areas under the low and high-temperature paths are equal to the heat absorbed and rejected by the cycle, whereas the area enclosed by the cycle is equal to the work input. Performance of refrigeration cycles is typically measured with a *Coefficient of Performance*, or *COP*, as defined in Equation (2.1).

$$COP = \frac{Cooling\ Load}{Work} \tag{2.1}$$

The comparison of Lorenz and Carnot cycle performances is difficult due to its dependence on the choice of characteristic evaporating and condensing temperatures [4]. For the Carnot cycle, the heat exchange process with the low and high-temperature reservoirs occurs at a constant temperature. For the Lorenz cycle, on the other hand, it takes place at a variable temperature. The performance of the Lorenz cycle may outperform or under-perform that of the Carnot cycle depending on the choice of temperature used to represent the heat exchange process. Some of the candidates considered are the heat exchanger inlet, outlet and mean refrigerant temperatures.

The constant loading method, recommended by McLinden and Radermacher [4], allows a more fair comparison between fluids with different cycle characteristics by requiring a constant ratio of capacity to total heat transfer area. Representing the condenser and evaporator by their overall conductances, UA_C and UA_E, the constant loading constraints may be expressed as,

$$\frac{Q_E}{UA_E + UA_C} = constant\ (= value\ for\ baseline\ refrigerant) \tag{2.2}$$

$$\overline{T}_{ref,E} = constant\ (= value\ for\ baseline\ refrigerant) \tag{2.3}$$

Whereas the first constraint alone can be satisfied by distributing the heat transfer area between the two heat exchangers in an infinite number of ways, the need for a given evaporator refrigerant temperature results in a specific evaporator size. This approach is well suited for theoretical calculations, but is difficult to implement in laboratory testing since it involves a modified system for each new fluid.

As shown in Figure 2.3, the heat exchange in a real vapor compression cycle occurs at a finite temperature difference between the refrigerant and the external fluid. The heat transfer irreversibilities, represented by the shaded areas, are a function of the match between the temperature profiles of both fluids. Even though similar fluid glides typically result in matched temperature profiles, a distinction should be made at this point between the two. Glide in this context refers to the change in temperature of a fluid between the inlet and outlet of a heat exchanger. Glide matching occurs when both fluids experience similar temperature changes. The matching of their temperature profiles, on the other hand, is measured with some kind of mean temperature difference, in order to account for local temperature variations between the endpoints of the exchanger.

2.2 Advantages and Disadvantages of Zeotropes

2.2.1 Advantages of Zeotropes

In addition to the increase in energy efficiency associated with the reduction of heat exchanger irreversibilities, zeotropes offer the ability to control system capacity through composition shifting. A brief discussion of this and other potential benefits of zeotropes is presented below.

Temperature Glide Matching

The relation between temperature glide matching and energy efficiency may be explained in a number of ways. One approach consists of obtaining analytical expressions for system *COP* as a function of the temperature difference between the two fluids. This was done by Rice [5] based on a modified Carnot analysis, as shown in Equation (2.4).

$$COP^* = \frac{\overline{T}_{ref,C}}{\overline{T}_{ref,C} - \overline{T}_{ref,E}} \tag{2.4}$$

The source and sink external fluid temperatures used in the traditional Carnot analysis are replaced by mean refrigerant-side heat exchanger temperatures, calculated as a function of the average external fluid temperatures and a representative fluid-to-fluid temperature difference.

Several definitions have been proposed for the last term. Kedzierski and Didion [6] used average mean temperature differences (*AMTD*) in an earlier study, whereas Rice adopted mean temperature differences (*MTD*) based on the log-mean temperature difference (*LMTD*) and an LMTD-correction factor (*F*) for non-counterflow heat exchanger configurations [7]. For the calculation of average external fluid temperatures, entropically averaged external fluid temperatures are typically approximated by arithmetic averages, as recommended by Alefeld [8]. The mean refrigerant temperature equations used by Rice were

$$\overline{T}_{ref,E} = \overline{T}_{air,E} - \frac{MTD_E}{F} \tag{2.5a}$$

$$\overline{T}_{ref,C} = \overline{T}_{air,C} + \frac{MTD_C}{F} \tag{2.5b}$$

Regardless of the conventions used in the modified *COP* calculation, the dependency of system performance on glide matching becomes apparent from Equations (2.5a) and (2.5b). As the temperature difference between the two fluids is reduced in the evaporator or the condenser, the corresponding mean refrigerant temperature increases or decreases respectively. Both changes lead to an improvement in system *COP*.

A more practical approach is to consider temperature glide matching as a means to operate at higher or lower evaporator and condenser refrigerant temperatures (i.e. pressures) respectively. Again, either option leads to lower compressor pressure ratios with corresponding reductions in compressor work and increases in system efficiency.

For a fixed mixture glide, the relative advantage of using a zeotropic blend over a no-glide refrigerant is determined by the slope of the air temperature profile. The effect of moderate and high air-flow rates on system performance for a specific zeotrope was considered by Smith [1] for two-stage evaporators used in refrigerator applications. The two cases are depicted in Figure 2.4 for a single-stage evaporator application.

For high air-flow rates, the air temperature profile becomes almost flat, giving a thermodynamic advantage to no-glide refrigerants over zeotropes. The zeotrope system is restricted to operate at lower evaporator pressures than the no-glide system to avoid a pinch-point at the exit of the evaporator.

For moderate air-flow rates the situation is reversed. Zeotrope systems can operate at higher evaporator pressures than their no-glide counterparts without concerns about pinch-points, as long as the slope of the air temperature profile remains smaller than that of the zeotropic mixture.

Simulation results presented by Smith [1], based on the assumption of equal evaporator and condenser glides for a R22/R123 *NARM*, show the system performance to reach a maximum for matching air and zeotrope glides. This and the observations discussed above regarding the relative advantage of using zeotropic mixtures over no-glide refrigerants are shown in Figure 2.5.

Didion and Bivens [3] found the heat exchanger irreversibility reductions associated with glide matching to be a function of the temperature lift for a given application, as well as the zeotropic mixture glide. Thus, for the same glide, a low lift application (e.g. air-conditioning) would have a greater percentage improvement than a high lift application (e.g. refrigeration), even though the absolute savings may be the same for both cases.

Other Advantages of Zeotropes

Zeotropic mixtures offer other attributes which can be used to increase the performance of specific applications. One of them is the ability to control system capacity by adjusting the mixture composition. Capacity control is achieved by regulating the suction side pressure, which calls for mixture components with boiling points as far apart as possible. Unfortunately, this is incompatible with the need for gliding temperature intervals below a range of approximately 30 °F, due to practical considerations. Several solution circuits have been proposed by Radermacher [9] to eliminate the inherent requirement of complete phase changes in the heat exchangers. The general approach is to shift the composition of the mixture by selectively removing liquid or vapor during the phase change process, thereby changing the thermodynamic characteristics of the mixture.

The use of inter-cooling with zeotropic mixtures in two-stage evaporator systems also leads to improvements in energy efficiency. Inter-cooling between the high and low-temperature evaporators allows the low-side pressure to be raised, by freeing up heat exchanger pinch-points. Performance improvements with zeotropic mixtures in such a system may be obtained with both moderate and high air-flow rates [1].

2.2.2 Disadvantages of Zeotropes

Heat Transfer Coefficient Degradation

One major disadvantage of zeotropic mixtures is the degradation of their heat transfer coefficients, which are lower than those of pure refrigerants. This effect is more pronounced under the low heat and mass flux flow conditions typical of refrigerators. For operating conditions in the range of air-conditioning applications, Bivens and Yokozeki [10] reported a minor heat transfer coefficient degradation. Their calculations of heat transfer coefficients were based on condenser and evaporator experimental data for HCFC-22 and a zeotropic blend of HFC-32/HFC-125/HFC-134a (30/10/60%).

Jung et al. [11] identified the loss of effective wall superheat, the variation in physical properties due to mixing, and mass transfer resistance as some of the agents responsible for the degradation of mixture heat transfer coefficients in the annular flow regime. Two distinct regions exist in this regime, each one dominated by a different heat transfer mechanism: nucleate boiling and convective evaporation. As observed by Wattelet et al. [12], the heat transfer coefficient shows a strong dependence on heat flux in the nucleate boiling region, whereas quality is the principal flow parameter in the convective region.

Jung et al. drew the following conclusions regarding the factors responsible for the degradation of the mixture heat transfer coefficients. In the convective region, they found the variation in physical properties due to mixing to be most significant. An additional contribution was attributed to mass transfer resistance, resulting from the formation of concentration gradients within the liquid and vapor phases in the absence of appropriate mixing.

The loss of effective wall superheat was found to be an important factor in the nucleate boiling region. As quality is increased in annular flow, the effective wall superheat decreases due to the lower thermal resistance of the thinning liquid film, and the enhanced convection associated with higher vapor velocities. Eventually, the effective wall superheat falls below the minimum superheat required for bubble formation resulting in suppressed nucleate boiling.

Nucleate boiling is fully suppressed for both pure and mixed refrigerants beyond certain transition qualities, but those transition qualities are much lower for mixtures. This discrepancy may be explained by considering the phase change process for a zeotropic mixture. As the more volatile components diffuses away from the tube wall, the remaining liquid is enriched in the higher boiling point components which leads to a reduction in the effective superheat at the wall.

Other Disadvantages of Zeotropes

A number of practical concerns must be addressed before the widespread acceptance of zeotropic mixture. Some are safety issues, such as toxicity and flammability. The latter has been addressed in recent years by considering the extreme case of vapor, as opposed to liquid, charging of systems. Oil and material compatibility are also important. Many zeotropic blends proposed as replacements for HCFC-22 are incompatible with mineral oils, and require its replacement with alternatives such as polyolester oils.

Preferential leaks may lead to changes in the composition of a mixture which could significantly alter its performance. Another concern related to mixture composition is fractionation, the undesired variation in mixture composition within the system. Other performance penalties may be related to a higher operating superheat. The lack of a clearly identifiable change in the slope of the evaporating refrigerant temperature may reduce the reliability of the traditional method of sensing superheat by temperature. Any increases in superheat to avoid slugging of the compressor would result in further performance penalties.

2.3 Literature Review: System Performance of Zeotropes

Since no pure refrigerants exist as a drop-in replacement for HCFC-22, recent research efforts have been aimed at finding suitable refrigerant mixtures which could be used in existing air-conditioning and refrigeration systems. These efforts, which include computer simulations and experimental testing of potential alternatives, are unlikely to result in a single substitute for HCFC-22, but rather in a set of them, each better suited for a particular application. A recurring conclusion of both experimental and theoretical studies has been the need for hardware changes in system design in order to accommodate individual refrigerant characteristics.

2.3.1 Computer Simulation Studies

Computer system simulations, used by Domanski and Didion [13] and Fischer and Sand [14] among others, are a useful tool for the screening of alternative refrigerants even though the accuracy of their results is limited by the assumptions upon which they are based. For example, the semi-theoretical model used by Domanski et al. did not include transport properties, and assumed a pure cross-flow representation of heat transfer in the heat exchangers with the same overall heat transfer coefficient. The choice of pure cross-flow heat exchangers would yield conservative zeotrope performance predictions if the use of counterflow heat exchangers is expected. The opposite is true of simulations with pure counterflow heat exchangers, when applied to real systems with cross-flow heat exchangers.

Even though it is important to keep all the modeling assumptions in mind, these kind of simulation results are very useful for the screening of several replacement candidates. Didion et al. compared volumetric capacity, system *COP* and compressor discharge temperatures and pressures for nine HCFC-22 alternatives: two pure refrigerants, one azeotrope and six zeotropes with temperature glides ranging from 5.4 °C (9.7 °F) to 20.6 °C (37.2 °F). They did so using both a drop-in evaluation (in which only the expansion device is adjusted in the original system) and a modified system evaluation (based on the method of equal heat exchanger loading proposed by McLinden and Radermacher [4] and previously discussed in section 2.1.2), and presented their results on a relative basis to HCFC-22. Of particular interest to the present study are their heat pump simulation results obtained with a zeotropic blend of HFC-32/HFC-125/HFC-134a (30/10/60%) in the cooling mode. Under average operating conditions, the predicted system capacity and *COP* for the zeotrope system are both equal to 98% of those for the HCFC-22 system under the constant loading assumption. These changes are accompanied by a drop in both pressure and temperature at the compressor exit.

Fischer and Sand [14] conducted a more exhaustive screening for chlorine-free HCFC-22 alternative refrigerant mixtures using a simplified system simulation. In their study, they considered a total of 57,541 different binary and ternary blend compositions obtained from a sample of twenty-two chlorine and bromine-free pure refrigerants which were selected based on their normal boiling points. Thirteen blends with temperature glides lower than 5.55 °C (10 °F) were identified as promising HCFC-22 replacement candidates with regards to efficiency, capacity, operating pressure and flammability. Testing with a ternary blend of HFC-32/HFC-125/HFC-134a resulted in *COP* and capacity improvements of up to 4% and 20% respectively under typical air-conditioning operating conditions.

2.3.2 Experimental Evaluation

Experimental testing of alternative refrigerants with existing systems may also provide incomplete information. With the drop-in method, a new refrigerant is evaluated in a machine designed for the original refrigerant, thus giving no indication of the potential performance improvement for that particular fluid.

In agreement with modeling predictions, capacity and performance levels comparable to those of HCFC-22 were measured experimentally by Shiflett [15] in a split system residential heat pump charged with an HFC-32/HFC-125/HFC-134a (23/25/52%) zeotropic mixture. Their tests were conducted using environmentally controlled chambers to maintain the dry and wet bulb temperatures for the indoor and outdoor coils at conditions prescribed by ARI standards. Compared with HCFC-22, the ternary mixture provided similar cooling and heating capacities with a 3-4% reduction in energy efficiency, lower compressor discharge temperatures and higher compressor discharge pressures.

Similar trends were observed by Corr et al. [16] during their testing of a HFC-32/HFC-125/HFC-134a (23/25/52%) zeotropic mixture in a glycol/water chiller. A relevant finding of their study was the absence of detrimental effects on system performance associated with a change in lubricant. This was determined by comparing data obtained with HCFC-22 using both the original mineral oil in the system, and a polyolester oil. Another interesting observation was a reduction in refrigeration effect caused by additional evaporation between the evaporator exit and the compressor suction. The entrainment of liquid droplets at the evaporator outlet was reported for low superheat values.

The same ternary mixture was tested by Mumpower and Shiflett [17] using a compressor calorimeter. The focus of their study was to determine the use of mean heat exchanger temperatures to simulate cross-flow heat exchanger performance for mixtures with significant temperature glides. At condensing and evaporating temperatures of 110 °F (43.3 °C) and 0 °F (-17.8 °C), the reported condenser and evaporator glides for the HFC-32/HFC-125/HFC-134a (23/25/52%) zeotropic mixture are 9.1 °F and 9.4 °F respectively.

Their results showed no measurable effect on capacity or energy efficiency when defining superheat from either the mean or dew point temperature of the zeotrope. Subcooling, on the other hand, should be defined from the mean condensing temperature such that the sub-cooled liquid refrigerant temperatures for HCFC-22 and the mixture are the same. Several tests were run with the zeotropic mixture over a wide range of evaporator and condenser temperatures and compared to HCFC-22, resulting in 6% higher to 4% lower capacity and 2% higher to 3% lower energy efficiency.

Whereas the encouraging results of drop-in tests have contributed to a wider acceptance of zeotropic mixtures by the air-conditioning and refrigeration industry, their predicted energy efficiency improvement potential remains to be validated experimentally. Soft-optimized tests were conducted by Spatz and Zheng [18] for this purpose. Their goal was to determine the influence of re-circuiting the heat exchangers in order to approach a more counterflow arrangement between the air and the refrigerant flows, and to evaluate the addition of liquid-suction heat exchangers.

The results obtained with a re-circuited "A" coil evaporator using a HFC-32/HFC-125/HFC-134a (23/25/52%) zeotropic mixture were somewhat disappointing, with a slight performance reduction for the counterflow coil attributed to poor air-side flow distribution. Similar trends were observed under both ARI Tests "A" and "B" conditions, which correspond to outdoor temperatures of 95 °F and 82 °F respectively. The indoor conditions were the same for both tests, 80 °F dry bulb and 67 °F wet bulb temperature. In all cases, the performance of the zeotropic blend relative to that of HCFC-22 was also a function of compressor type. Testing with a scroll compressor resulted in comparable capacity to HCFC-22 with a 5% drop in energy efficiency, whereas drops in both capacity and efficiency were reported for a system operating with a reciprocating compressor.

Several tests of this kind were reviewed by the Air-Conditioning and Refrigeration Institute (ARI) as part of the *R-22 Alternative Refrigerants Evaluation Program* (AREP). The changes made to the original systems included lubricant, compressor displacement, refrigerant charge, expansion device opening, heat exchanger circuiting and size, compressor speed and the size of the accumulators [19]. The performance achieved with the alternative refrigerant was normalized using that of HCFC-22 in the unmodified system.

The majority of the tests reviewed were conducted with refrigerant blends of HFC-32/HFC-125 and HFC-32/HFC-125/HFC-134a. Of particular interest to this study are the results obtained with an HFC-32/HFC-125/HFC-134a (23/25/52%) mixture, chosen to replace the original HFC-32/HFC-125/HFC-134a (30/10/60%) mixture to reduce flammability risks. The reported capacity and efficiency ratios range from 0.93 to 1.01 and 0.90 to 0.97 respectively.

2.3.3 Modifications in System Design

A major advantage of zeotropes over pure refrigerants remains the fact that they would benefit more from hardware changes. Theoretical work by Rice [5] with heat pumps predicted performance improvement opportunities to be primarily in the cooling mode. Rice recommended concentrating on reducing the mean temperature difference of the evaporator, the heat exchanger with the largest external air glide. A closer look at evaporator design modifications is also motivated by their impact on dehumidification. Adding heat transfer area tends to force the air temperature profile to conform more closely to that of the refrigerant. With zeotropes, the evaporator air would experience sufficient temperature drop to accomplish dehumidification, as noted by Atwood [20]. Having found zeotropic mixture replacements which perform equally or slightly better than HCFC-22, the challenge remains to obtain further efficiency improvements through system design optimization. Didion summarized the current focus of the research with these words:

> "Zeotropic refrigerant mixtures offer other attributes which can be utilized to increase the performance of specific applications ... But due to the needs of the times, widespread acceptance of these mixtures probably depends mostly on their ability to improve steady-state full and part load efficiency of air-conditioning or refrigeration systems ..." [2]

2.4 Summary

This chapter discussed the choice of zeotropic refrigerant mixtures as potential replacements for HCFC-22. The basic thermodynamics of zeotropes, and their relation to the vapor compression cycle were introduced.

In addition, a review of the most recent efforts to evaluate the performance capabilities of HCFC-22 substitutes, including both computer simulations and experimental testing, was also presented. A conclusion drawn from these studies is the need for hardware modifications, particularly those related to evaporator design, in order to take full advantage of the potential thermodynamic benefits of zeotropes. The remaining chapters look at how this was done for stationary air-conditioning applications.

2.5 References

[1] Smith, M.K., “Analysis and Optimization of a Dual-load Vapor Compression Cycle Using Non-azeotropic Refrigerant Mixtures", Ph.D. Thesis, University of Illinois at Urbana-Champaign, 1993.

[2] Didion, P.A., National Institute of Standards and Technology, Short Course:World-wide Experiences in Using New Refrigerants, Purdue University, July 1994.

[3] Didion, P.A., and D.B. Bivens, "Role of mixtures as alternatives to CFCs", International Journal of Refrigeration 13, May 1990.

[4] McLinden, M. and R. Radermacher, “Methods for comparing the performance of pure and mixed refrigerants in the vapor compression cycle”, International Journal of Refrigeration, Vol.10, pp. 318-325, November, 1987.

[5] Rice, C.K., “Influence of HX Size and Augmentation on Performance Potential of Mixtures in Air-to-air Heat Pumps”, ASHRAE Transactions, Vol. 99, Pt. 2, 1993.

[6] Kedzierski, M.A., and D.A. Didion, Personal communication reported by Rice, C.K5.

[7] Holman, J.P., Heat Transfer, 3d ed. New York: McGraw-Hill, 1972.

[8] Alefeld, G., “Efficiency of Compressor Heat Pumps and Refrigerators Derived from the Second Law of Thermodynamics”, International Journal of Refrigeration 10(6): 331-341, 1987.

[9] Radermacher, R., “Advanced Versions of Heat Pumps with Zeotropic Refrigerant Mixtures”, ASHRAE Transactions, Vol.92, Pt. 2A, 1991.

[10] Bivens, D.B., and A. Yokozeki, “Heat Transfer of Refrigerant Mixtures”, Proceedings International Refrigeration Conference at Purdue , Purdue University, July 1994.

[11] Jung, D.S., M. McLinden, R. Radermacher, and D. Didion, “A Study of Flow Boiling Heat Transfer with Refrigerant Mixtures”, International Journal of Heat and Mass Transfer, Vol. 32, No. 9, pp. 1751-1764, 1989.

[12] Wattelet, J.P., “Heat Transfer Flow Regimes of Refrigerants in a Horizontal-Tube Evaporator”, Ph.D. dissertation, University of Illinois at Champaign-Urbana, 1994.

[13] Domanski, P.A., and Didion, D.A., "Thermodynamic evaluation of R-22 alternative refrigerant and refrigerant mixtures", ASHRAE Transactions, Vol.99, Pt.2, 1993.

14 Fischer, S.K., and Sand, J.R., "Screening analysis for chlorine-free alternative refrigerants to replace R-22 in air-conditioning applications", ASHRAE Transactions, Vol.99, Pt.2, 1993.

15 Shiflett, M.B., “HCFC-22 Alternatives for Air Conditioners and Heat Pumps”, Proceedings International Refrigeration Conference, Purdue University, July 1994.

16 Corr, S., Gilbert, B., Dekleva, T., Low, R., Murphy, F.T., and Davies, G., “Trials with Zeotropic Refrigerants as Replacements for R-22 in an Instrumented Glycol/water Chiller”, Proceedings International Refrigeration Conference , Purdue University, July 1994.

17 Mumpower, K.N., and Shiflett, M.B., “Calorimeter Experiments with SUVAR AC9000”, Proceedings International Refrigeration Conference , Purdue University, July 1994.

18 Spatz, M.W., and Zheng, J., “Experimental Evaluation of R-22 Alternative Refrigerants in Unitary Air Conditioning Equipment”, Proceedings International Refrigeration Conference, Purdue University, July 1994.

19 Godwin, D.S., “Results of Soft-Optimized System Tests in ARI’s R-22 Alternative Refrigerants Evaluation Program”, Proceedings International Refrigeration Conference , Purdue University, July 1994.

20 Atwood, T. "The ABCs of NARBs (Non-azeotropic Refrigerant Blends)", ASHRAE Transactions, Paper HI-85-18 No. 1, 1985, pp.909-917.

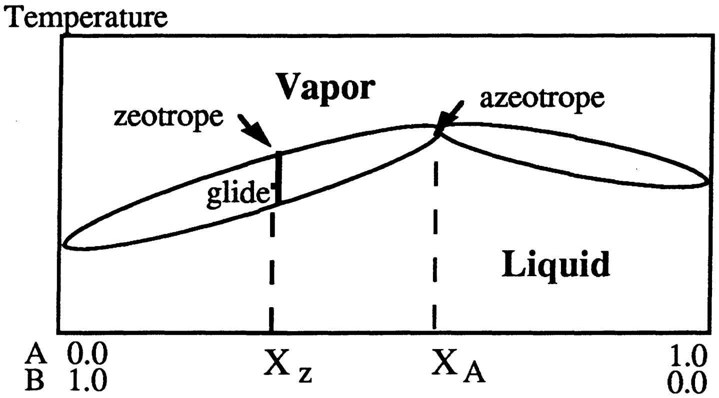

Figure 2.1 Temperature versus Concentration Diagram for a Binary Refrigerant Mixture at Constant Pressure [1]

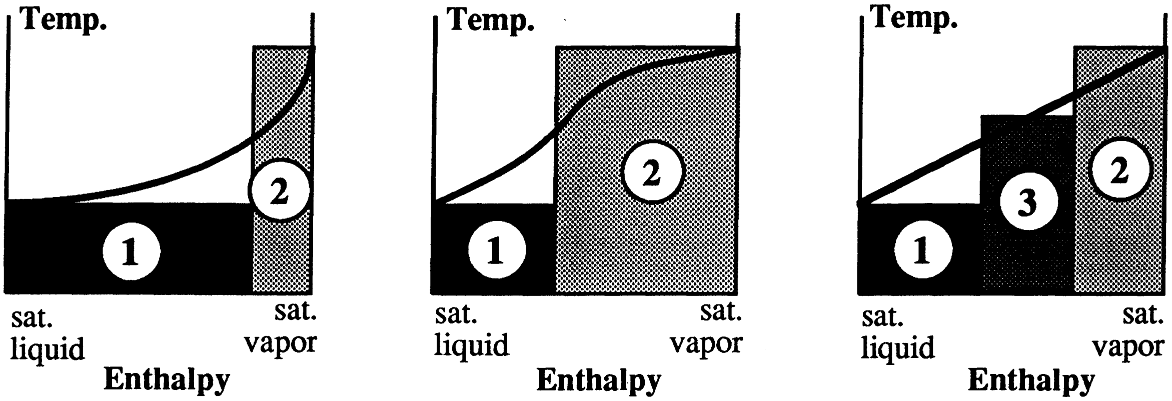

Figure 2.2 Mixture Temperature Non-linearity and its Possible Correction [2]

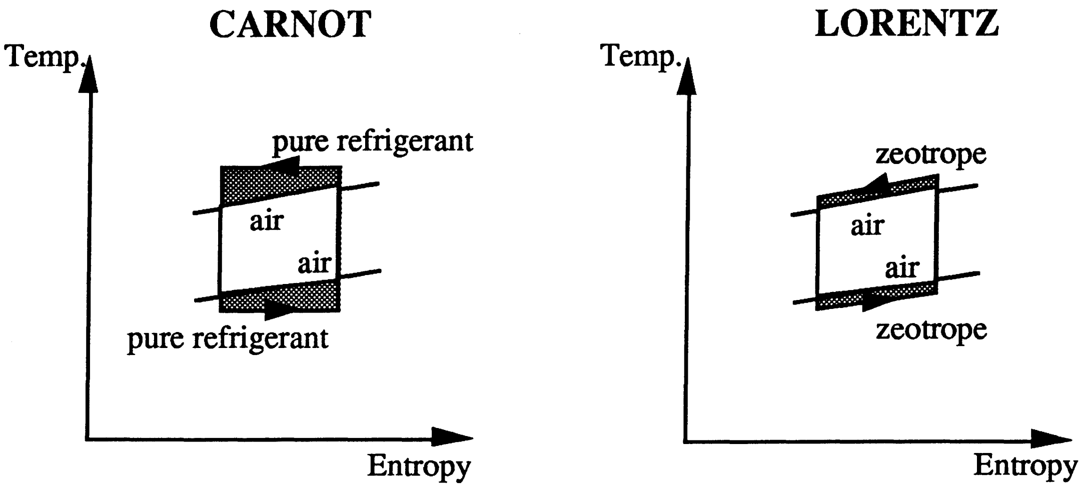

Figure 2.3 Advantage of Lorenz Cycle (zeotropes) over Carnot Cycle (no-glide refrigerants)

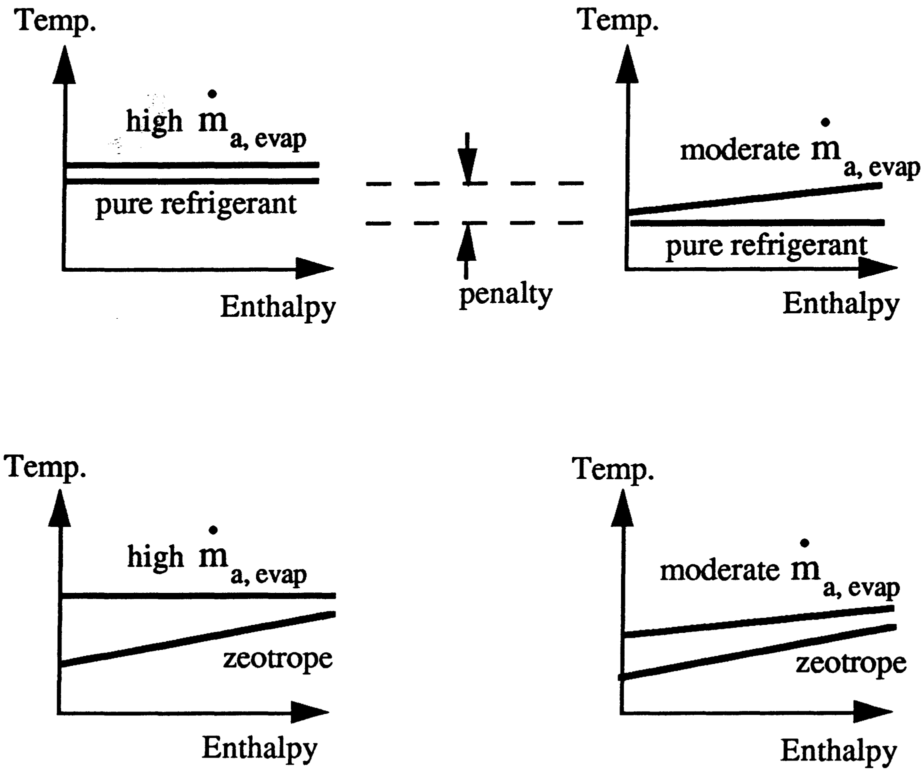

Figure 2.4 Evaporator Temperature Profiles for No-glide and Zeotropic Refrigerants for Moderate and High Air Flowrates

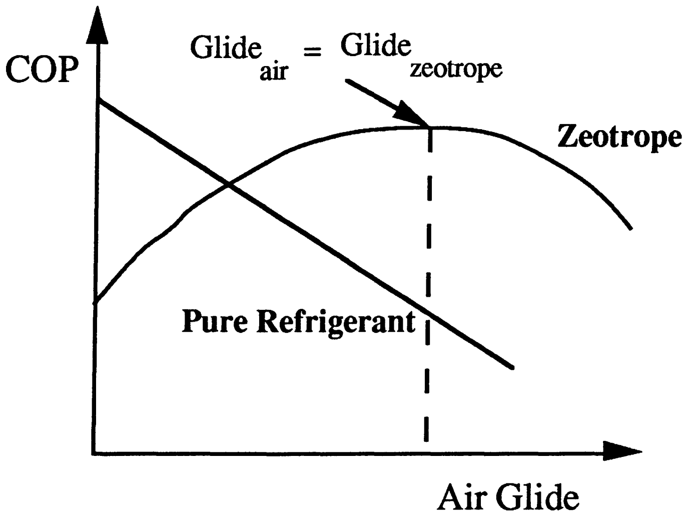

Figure 2.5 Effect of Air Glide on System Performance for a Specific Zeotrope versus a Pure Refrigerant (assuming equal evaporator and condenser zeotropic glides) [1]

CHAPTER 3
THERMODYNAMIC OPTIMIZATION

This chapter is divided into three sections. The first section introduces some of the terms used in the irreversibility minimization analysis, as well as the link between irreversibility reduction and increased system efficiency. The second section reviews the literature on heat exchanger optimization, and discusses the criteria used to quantitatively measure heat exchanger performance. Finally, the third section describes the methodology proposed for the design optimization of heat exchangers operating with gliding refrigerants.

3.1 Exergy Destruction and System Performance

As noted by Bejan [1] ,"work" is an important commodity in the field of engineering thermodynamics, whether the purpose of a process or device is to extract work from various sources or to accomplish the most with that which is already available. A fraction of the available work is lost during any such process due to system irreversibilities, a loss that can be measured in units of entropy generation. The lost-work theorem , which relates the generation of entropy to the destruction of available work, is summarized in the following section. A more detailed presentation may be found in Bejan [1].

3.1.1 Lost Available Work or Exergy

Figure 3.1 depicts an arbitrary multi-port open system, in thermal contact with any number of heat reservoirs of temperatures T_i (i = 0,1,2,..,n). The system is in contact with the atmosphere (T_0 ,P_0), which acts as a pressure reservoir as well.

For such a system, the first and second laws yield

$$\frac{dE}{dt} = \sum_{i=0}^{n} \dot{Q}_i - \dot{W} + \Sigma_{in} \dot{m} \cdot h^o - \Sigma_{out} \dot{m} \cdot h^o \tag{3.1}$$

$$\dot{S}_{gen} = \frac{dS}{dt} - \sum_{i=0}^{n} \frac{\dot{Q}_i}{T_i} - \Sigma_{in} \dot{m} \cdot s + \Sigma_{out} \dot{m} \cdot s \geq 0 \tag{3.2}$$

where h_0 in Equation (3.1) represents the enthalpy group $\left(h+\frac{v^2}{2}+gz\right)$.

The work transfer rate, $\dot{W}$, includes any possible mode of work transfer $\left(P\,\frac{dV}{dt}, \dot{W}_{electric}, etc\right)$. Combining the first and second law Equations (3.1) and (3.2), this work transfer rate may be expressed as an explicit function of the degree of thermodynamic irreversibility of the system, $\dot{S}_{gen}$,

$$\dot{W} = -\frac{d}{dt}(E - T_0 S) + \sum_{i=1}^{n} \left(1 - \frac{T_0}{T_i}\right)\dot{Q}_i + \\ \Sigma_{in}\, \dot{m}(h^0 - T_0 s) - \Sigma_{out}\, \dot{m}(h^0 - T_0 s) - T_0 \dot{S}_{gen} \tag{3.3}$$

In the reversible limit the work transfer rate becomes

$$\dot{W}_{rev} = -\frac{d}{dt}(E - T_0 S) + \sum_{i=1}^{n} \left(1 - \frac{T_0}{T_i}\right)\dot{Q}_i + \\ \Sigma_{in}\, \dot{m}(h^0 - T_0 s) - \Sigma_{out}\, \dot{m}(h^0 - T_0 s) \tag{3.4}$$

Hence, the irreversible operation of the system results in a certain amount of work being destroyed, equal in magnitude to $\dot{W}_{rev} - \dot{W}$. The lost work theorem, referred to by Bejan as the *Gouy-Stodola* theorem, shows the proportionality that exists between the respective rates of lost available work and entropy generation

$$\dot{W}_{lost} = T_0 \dot{S}_{gen} \tag{3.5}$$

It is important to notice that, regardless of the sign of $\dot{W}$ and $\dot{W}_{rev}$, the lost work must always be greater or equal to zero to avoid a violation of the second law.

The fraction of $\dot{W}$ which is available for consumption is defined as the rate of available work ($\dot{E}_w$), equal to the system work ($\dot{W}$) minus the work exchanged between the system and the atmospheric pressure reservoir P_0. For the irreversible process described in Figure 3.1,

$$\begin{aligned}\dot{E}_w &= \dot{W} - P_0\frac{dV}{dt} \\ &= -\frac{d}{dt}\left(E + P_0V - T_oS\right) + \sum_{i=1}^{n}\left(1-\frac{T_0}{T_i}\right)\dot{Q}_i + \\ &\quad \Sigma_{in}\ \dot{m}\left(h^0 - T_0 s\right) - \Sigma_{out}\ \dot{m}\left(h^0 - T_0 s\right) - T_0\dot{S}_{gen}\end{aligned} \tag{3.6}$$

As expected, the rate of available work reaches a maximum value in the reversible limit,

$$\dot{E}_{w,rev} = \dot{W}_{rev} - P_0\frac{dV}{dt} \tag{3.7}$$

The atmospheric work $P_0\frac{dV}{dt}$ is absent in most flow systems of engineering interest. Its presence, however, can result in absolute values of $\dot{E}_w$ greater than those of $\dot{W}$.

3.1.2 Exergy Balance for an Open System

The same mass flow, heat and work transfer processes considered in Figure 3.1 may be described in terms of exergy transfers. Exergy enters the control volume via mass flow and heat transfer, and leaves via mass flow and the delivery of useful work. For a system operating irreversibly, the exergy delivered differs from its reversible ceiling value by an amount equal to the loss of available work,

$$\dot{W}_{lost} = \dot{E}_{w,rev} - \dot{E}_w = \dot{E}_{w,lost} \tag{3.8}$$

Even though the concept of exergy has been applied in this discussion to a work producing process, exergy can also be used to describe the state of a fluid given the choice of an appropriate reference point. The enthalpy of a fluid, for example, is defined in terms of the energy removal per unit mass of fluid required to reach a specified reference state at which the enthalpy is assumed equal to zero. Similarly, the exergy of a fluid is defined as the exergy that would be produced while undergoing a reversible process, at the end of which the fluid would be in equilibrium with a specified reference or dead state (P_0 ,T_0).

Thus, the concept of exergy destruction within an open system is still applicable, even when no heat or work transfer interactions are present between the control volume and its surroundings. For a simplified open system with no work transfer operating under steady-state conditions, the equation for its associated entropy generation may be reduced to

$$\dot{S}_{gen} = \sum_{i=1}^{n} \left(1 - \frac{T_0}{T_1}\right)\frac{\dot{Q}_i}{T_0} + \\ \Sigma_{in}\, \dot{m}\frac{(h^0 - T_0 s)}{T_0} - \Sigma_{out}\, \dot{m}\frac{(h^0 - T_0 s)}{T_0} \tag{3.9}$$

3.1.3 Exergy Destruction in an Air-Conditioning Cycle

An air-conditioning cycle is typically analyzed as a closed system in thermal communication with two heat reservoirs. As shown in Figure 3.2, the system removes a load (Q_C) from a cold room at T_L and rejects a larger load (Q_H) to the warmer ambient conditions at T_H.

The same cycle may be treated both in terms of energy and exergy transfers. Figures 3.3a and 3.3b show the energy conservation and exergy destruction that take place within the control volume enclosing the air-conditioning system. The exergy flow associated with the condenser heat transfer rate is ignored in Figure 3.3b, by choosing the warmer ambient conditions (T_H) as the dead state.

The lost work for the cycle can be evaluated by performing an exergy balance on the same control volume,

$$W_{lost} = E_{Q_L} - E_w = Q_L\left(1 - \frac{T_H}{T_L}\right) - (-W) \tag{3.10}$$

and the total work input required becomes

$$W = Q_L\left(\frac{T_H}{T_L} - 1\right) + W_{lost} \tag{3.11}$$

Equation (3.11) indicates a penalty in terms of required compressor work, which depends on the degree of irreversibility of the system. The nature of this dependency may be more closely examined by looking at the second-law efficiency of the system and its effect on its coefficient of performance. Following an approach similar to that used by Bejan in his analysis of a refrigerator cycle [1], the resulting first and second-law measures of efficiency for an air-conditioning system may be shown to be

$$\eta_{2nd} = \frac{-E_{w,rev}}{-E_w} = \frac{-E_{Q_L}}{-E_{Q_L} + T_H S_{gen}} \tag{3.12}$$

and

$$COP_{cycle} = \frac{Q_L}{W} = \frac{\eta_{2nd}}{T_H / T_L - 1} \tag{3.13}$$

It is clear from Equation (3.13) that system *COP* is strongly dependent on the quality of the energy transformations occurring within the system. Thus, a minimization of the total system irreversibility should maximize the coefficient of performance.

3.2 Heat Exchanger Optimization: A Literature Review

Performance evaluation criteria for heat exchanger design, such as initial and operating costs, maximum exchanger effectiveness and minimum volume, lead toward different aspects of optimization: economical, energy, and dimensional respectively for the examples just mentioned [2]. The thermodynamic optimization of heat exchangers, based on irreversibility loss minimization, has become generally accepted since the work of Bejan [3]. With this approach, the component is thermodynamically isolated from the rest of the system. Reduced component irreversibilities are expected to result in reduced system irreversibilities, neglecting any inter-dependence between the irreversibilities of various components. Although this principle is generally acceptable, its violation may lead to paradoxes as illustrated by Bejan [4].

For a typical two-fluid heat exchanger with no heat leaks, an exergy analysis reduces to a balance between the exergy transfers via the inlet and outlet mass flows of both fluids, as shown in Figure 3.4.

In fact, the expression for the net entropy generation within the exchanger becomes further simplified as the exergy terms (*e*) are replaced by functions of enthalpy (*h*) and entropy (*s*) according to $e(P,T) = h(P,T) - T_o s(P,T)$. The final form of the entropy generation then becomes

$$\dot{S}_{gen} = \dot{m}_{ref}(s_{ref,in} - s_{ref,out}) + \dot{m}_{air}(s_{air,in} - s_{air,out}) \tag{3.14}$$

Bejan considered an air-to-air heat exchanger in his analysis, and used analytical expressions to calculate its irreversibility based on simplified equations for the entropy of perfect gases [3]. Similar approximations have been used by other authors to evaluate the entropy change of perfect gases and incompressible liquids. As shown by Carrington [5], however, the complexity of analytical entropy expressions is drastically increased for multi-component fluids, when mixing effects are taken into account.

3.2.1 Sources of Irreversibility in a Heat Exchanger

Several competing mechanisms are responsible for the entropy generation within a heat exchanger, and their most desirable trade-off results in the thermodynamic optimum [4]. A major advantage of using analytical expressions to calculate the entropy generation is that the terms corresponding to the various sources of irreversibility are easily identifiable for comparison. Bejan was able to decouple the entropy generation due to frictional dissipation from that due to heat transfer across a finite temperature difference for certain special cases.

Whereas the presence of viscous dissipation irreversibilities is intuitively obvious, that is not necessarily the case for heat transfer irreversibilities. Bejan offered a simple explanation by taking a closer look at the heat transfer mechanism within the heat exchanger wall.

A first law analysis, shown to the left of Figure 3.5, gives no insights regarding the presence of irreversibilities. An arbitrary amount of heat ($\dot{Q}$) leaves the hot reservoir and an equal amount enters its colder counterpart. An equivalent arrangement is considered to the right of Figure 3.5, which is identical to that of the previous figure from a first law standpoint. In this example, however, an imaginary reversible engine operates between the two reservoirs. The finite amount of work produced, $\dot{B}$, is dissipated as heat by a brake and ultimately absorbed by the cold reservoir, such that the total amount of heat transferred to that reservoir remains unchanged. This mental exercise shows that any heat transfer process across a finite temperature difference is accompanied by a corresponding loss of available work, given by

$$\dot{W}_{lost} = \left(1 - \frac{T_L}{T_H}\right)\dot{Q} \tag{3.15}$$

An additional source of irreversibility was identified by Bejan for heat exchangers that are not balanced and counterflow, which he referred to as remanent or flow-imbalance irreversibilities (a heat exchanger is considered balanced when the capacity flowrates of both fluids, the product of the mass flow rate of the fluid times its average specific heat, are equal in magnitude). This term is an unavoidable irreversibility contribution due to flow configuration which depends on operating conditions. Analytical results presented by Bejan showed the remanent irreversibility to be consistently greater for parallel flow than for counterflow configurations for all capacity flowrate ratios. As that ratio approaches infinity, a situation commonly encountered in real exchangers as one of the fluids undergoes a phase change, the remanent term reaches a maximum value regardless of flow configuration.

Others sources of irreversibility in a heat exchanger arise from the mixing of air streams with dissimilar temperatures that occurs between rows. For an exchanger operating with multi-component refrigerant mixtures, the mixing that occurs within the refrigerant stream is a source of irreversibility as well.

The dehumidification process associated with evaporators operating under wet conditions is also inherently irreversible. Theoretical work by San et al. [6], which considered the influence of design parameters on combined heat and transfer processes, may be of particular importance for the design of heat and mass exchangers.

3.2.2 Relevant Design and Operating Parameters

The dependence of the irreversibility function on dimensional and operating parameters varies from one type of irreversibility to the next. For example, in the case of forced convection heat transfer through a smooth tube [7], a reduction in tube diameter lowers the heat transfer irreversibilities while increasing those due to fluid friction. Hence, the entropy generation function may be dominated by one or the other depending on the value of the tube diameter. As a result of such competing effects, the dependence of the overall exchanger irreversibility on design parameters is often non-monotonic. Another interesting result is that the relative contribution of each irreversibility source need not be the same at the optimum.

Similar trade-offs between heat transfer and fluid friction are produced by varying other heat exchanger dimensions such as fin and tube spacing, or by selecting different operating conditions. The ratio of fluid temperatures approaching the exchanger, or the Reynolds number of one of the fluids, are examples of non-dimensional variables based on the operating conditions which greatly affect the entropy generation function.

3.2.3 Entropy Generation Numbers

As both dimensional and operating parameters are varied, it is important to compare the associated entropy generation results in a consistent fashion. One way to do so is by picking a baseline case, using its entropy generation value as a reference. This was the option chosen by Bejan in his tube diameter optimization study, with the least irreversible case as a baseline [7].

An alternative approach, favored as the complexity of parametric studies increases with an increasing number of non-dimensional parameters, is to define an entropy generation number. Several such numbers have been proposed following the use of the minimum capacity flowrate by Bejan in the denominator for unbalanced heat exchangers. Some of these are described in Table 3.1.

Table 3.1 Entropy Generation Numbers

Definition	Author	Comments
$N_{s,min} = \dot{S}_{gen} / \dot{C}_{min}$	A., Bejan	
$N_{s,min} = \dot{S}_{gen} / \dot{C}_{min}$	G., Grazzini, F., Gori	

Definition	Author	Comments
$N_Q = \dot{S}_{gen} / \dot{S}_{gen,Q}$	G., Grazzini, F., Gori	$\dot{S}_{gen,Q} = \dot{Q}(1/T_{1,in} - 1/T_{2,in})$ Entropy generation resulting from heat transfer between the two stream inlet temperatures
$N_M = \dot{S}_{gen} / \dot{S}_{gen,max}$	G., Grazzini, F., Gori	$\dot{S}_{gen,max} = \dot{S}_{gen,Q} + \dot{m}_1 \cdot \dot{s}_{g\ 1,max} + \dot{m}_2 \cdot \dot{s}_{g\ 2,max}$ Entropy generation resulting from the free expansion of the fluid from inlet pressure to zero (for a liquid) or near-zero (for a vapor)

Grazzini and Gori investigated the dependence of these entropy generation numbers on heat exchanger *NTU* (number of heat transfer units) for various inlet temperature and capacity flow rate ratios [9]. Their results were generated for an air-to-air counterflow heat exchanger and showed some interesting trends.

The first number considered was the original entropy number, $N_{S,min}$, the heat transfer entropy generation per degree of temperature difference of the fluid with the minimum capacity flowrate. For balanced capacity flowrates (or a capacity flowrate ratio close to unity) it has a maximum and a minimum at low and intermediate *NTU* values respectively, both of which become less pronounced as the capacity flowrate ratio approaches zero. The same observation was made for two different inlet temperature ratios.

Two additional entropy generation numbers were defined as part of the same study. The first one, N_M, was based on the maximum possible entropy generation as described in Table 3.1, and showed trends similar to those of $N_{S,min}$. However, while $N_{S,min}$ indicated that a more balanced exchanger would be less irreversible for any operating point, the relative magnitudes of N_M for the balanced and the unbalanced cases depend on the range of *NTU*.

The performance of the second new entropy generation number, N_Q, was the most promising. This function presented only a minimum over the entire range of capacity flowrate ratios, and consistently increased as the exchanger became more unbalanced. The difference in trends described above serves as a reminder that a non-dimensional number must be carefully chosen depending on the type of comparison to be made. The choice of that number alone may influence the results of the study.

3.2.4 Optimization Constraints

Considerations related to material cost and heat exchanger volume often result in a constrained thermodynamic optimization. Bejan investigated both the independent and combined effects of area and volume constraints on the optimization of the entropy generation number. These reduced the number of degrees of freedom, effectively limiting the number of variables which could be adjusted during the minimization effort. As expected, the degree of irreversibility for an air-to-air exchanger decreased with both increasing area and volume.

Sekulic and Herman [9] proposed fixing the operating point of the heat exchanger. It involves holding *NTU*, the capacity flowrate ratio and the flow configuration constant, while varying selected non-dimensionalized design variables. In general, this amounts to holding the heat exchanger effectiveness constant, which in turn fixes the heat transfer irreversibility component [3]. Thus, the total irreversibility becomes a function of the fluid friction contributions associated with each of the fluid streams, both of which are coupled through the constant-*NTU* constraint.

3.2.5 Other Measures of Irreversibility

Several ways of quantifying the irreversibility in a heat exchanger have been proposed, in addition to the entropy generation numbers discussed above. In a recent study, Sekulic introduced a new measure of the quality of energy transformation within the heat exchanger [2]. This quantity is referred to as the heat exchange reversibility norm, defined as

$$HERN = 1 - \frac{\dot{S}_{gen,actual}}{\dot{S}_{gen,worst\ case}} \tag{3.16}$$

While the minimum of the entropy generation function is well defined and equal to zero for the reversible case, the choice of a most disadvantageous case is much more arbitrary. Sekulic considered the adiabatic mixing of the two fluid streams, neglecting the irreversibility contributions due to fluid friction. The dependence of the resulting function on heat exchanger *NTU* was investigated for several cross flow and counterflow configurations.

As expected, the dependence of *HERN* on the flow configuration decreases as the capacity flowrate ratio approaches zero. It is surprising, however, that with the exception of the zero capacity flowrate case, *HERN* approaches different limiting values as the size of the exchanger increases to infinity.

Reistad [11] introduced a measure of heat exchanger irreversibility based on a second law effectiveness. This quantity describes the quality of the exergy transfer between the two fluid streams, and is defined as

$$\varepsilon_{Reistad} = \frac{exergy\ lost\ by\ cold\ stream}{exergy\ gained\ by\ warm\ stream} \tag{3.17}$$

Another important contribution made by Reistad in a more recent study with Aceves-Saborio and Ranasinghe [12], was the finding of a finite area optimal counterflow exchanger, following the inclusion of an additional irreversibility term to account for the exergy of the material of construction of the exchanger.

Similar second law efficiencies were used by Moran [13] and Witte [14], in order to put the magnitude of the total irreversibility in perspective. The entropy generation was non-dimensionalized with respect to the heat exchanger capacity, a convenient choice for the comparison of different exchangers operating at equal capacity,

$$\varepsilon_{Witte} = 1 - \frac{T_o \dot{S}_{gen}}{\dot{Q}} \tag{3.18}$$

While this efficiency has an upper limit equal to unity for the reversible limit, it is curious to note that it could have negative values for exchangers working at cryogenic temperatures [4].

3.2.6 Other Optimization Considerations

In addition to developing a good understanding of how heat exchanger irreversibilities vary with various parameters, it is also important to determine the order of magnitude of those changes as well as their impact on manufacturing and operational costs.

Bejan proposed minimizing the irreversibilities associated with the heat exchanger operation without considering its capital cost, or the possibility of having different monetary values for the different irreversibility contributions. As shown by Aceves-Saborio et al., the inclusion of other considerations in the optimization, such as the material of construction, may significantly affect the nature of the results.

London [15] presented a thermo-economic analysis which points out the importance of taking into account the interdependence between the operational irreversibilities of the entire system. In his approach, the order of magnitude of each entropy generation contribution is compared to that of the compressor work requirements.

Zubair et al. [16] introduced a more complete objective function in their thermo-economic optimization of two-phase heat exchangers. A cost function was defined, including fixed capital costs and variable operating costs dependent on both heat transfer and pressure drop irreversibilities, with separate but arbitrary unit monetary costs for each type of irreversibility. This type of work is extremely important in that it attempts to bridge the gap between a purely thermodynamic heat exchanger optimization and more realistic cost considerations. Such an approach becomes increasingly vital in cases where the optima based on economic and thermodynamic considerations differ substantially.

Table 3.2 provides a summary of the major studies discussed in this section related to the field of thermodynamic optimization

Table 3.2 Heat Exchanger Thermodynamic Optimization Studies

Author	Description of study	Comments
A, Bejan 1977 [17]	• Analysis of gas-to-gas counterflow heat exchangers	• Sources of irreversibility identified and evaluated

Author	Description of study	Comments
J.Y., San W.M., Worek Z., Lavan 1987 [6]	• Theoretical study of entropy generation for limiting cases of heat and mass transfer	• Isothermal convective mass transfer in a channel considered
S.M., Zubair P.V., Kadaba R.B., Evans 1985 [16]	• Method developed for optimizing two-phase heat exchangers	• Thermo-economic analysis, including heat exchanger and irreversibility costs
G., Grazzini F., Gori 1988 [10]	• Theoretical analysis of counterflow heat exchangers	• Both liquids and gases • New non-dimensional entropy generation parameters introduced
L.C., Witte 1988 [14]	• Heat exchanger optimization based on 2nd Law efficiency dependence on size	• Pressure drop irreversibilities neglected • Alternative 2nd Law efficiency defined • Irreversibility costs evaluated
S., A-Saborio J., Ranasinghe G.M., Reistad 1989 [12]	• Heat exchanger optimization accounting for the exergy of construction	• Counterflow exchangers with perfect gas fluids only
D.P., Sekulic 1990 [2]	• Quality of heat exchange process estimation for various exchanger designs	• Pressure drop irreversibilities neglected • Maximum irreversibility case considered for normalization

3.3 Evaporators with Zeotropes: An Optimization Methodology

The use of an irreversibility loss function in the optimization of heat exchangers operating with single and two-phase pure refrigerants was discussed in the previous sections. A similar approach may be applied to the design of evaporators with gliding mixed refrigerants.

As shown in Figure 3.6, a control volume is drawn around the evaporator, such that only those exergy transfers via the mass flow of moist air, refrigerant and liquid condensate need to be considered in the analysis.

Neglecting heat leaks, the entropy generation resulting from an exergy balance on this control volume is equal to

$$T_0\dot{S}_{gen} = \dot{m}_{air}\cdot(e_{moist\ air,in} - e_{moist\ air,out} - \omega\cdot e_{condensate,out}) + \dot{m}_{ref}\cdot(e_{ref,in} - e_{ref,out}) \tag{3.19}$$

where the exergies of the entering and leaving fluid streams are indicated by the subscripts "i " and "o " respectively.

The direct evaluation of entropy changes, as opposed to their inclusion in an exergy balance, has been recommended by London [15] to avoid the need for an arbitrary reference state (P_0 ,T_0). For this study, which includes the analysis of wet evaporators, the use of exergies may be justified for several reasons

First of all, the presence of the liquid condensate outlet stream is not matched by a similar inlet counterpart, even though a mass balance across the control volume is satisfied due to changes in the moisture content of the air streams. It is therefore confusing to talk about the entropy change of the condensate stream, whereas the use of local exergy values references each of the fluid states to an arbitrary reference state.

In addition, typical outside ambient conditions are an obvious choice for the dead state used in air-conditioning applications. The same set of dead state conditions were used all throughout the optimization study, thus avoiding any dependence of the results an that choice.

The selection of atmospheric dead state conditions is fairly arbitrary, as pointed out by Bejan [18]. Whereas P_0 =1 atm is an obvious choice for the pressure, a convention for T_0 and ϕ_o is not yet in place. Bejan reviewed four different dead states used in earlier studies, and settled on that proposed by Szargut and Styrlska [19]. The same dead state definition was used in the current study, represented by

$$\begin{aligned} T_0 &= 25\ ^oC\ (298.15K) \\ P_0 &= 1\ atm\ (0.101325\ MPa) \\ \phi_0 &= 0.6\ (\omega_0 = 0.0119) \end{aligned} \tag{3.20}$$

3.4 Summary

This chapter addresses the need to evaluate the thermodynamic performance of heat exchangers. Definitions of some of the terms used in the irreversibility analysis are presented, along with the link between system irreversibility and efficiency.

This is followed by a review of the literature on exchanger optimization, including efforts to separate and quantify the various sources of irreversibility within an exchanger.

Finally, a methodology is proposed for the design optimization of evaporators with gliding refrigerants, operating with combined heat and mass transfer.

3.5 References

1 Bejan, A., *Advanced Engineering Thermodynamics*, John Wiley & sons, Inc., chapter 3, 1988.

2 Sekulic, D.P., "The 2nd Law quality of energy transformation in a heat exchanger", Journal of Heat Transfer-Transactions of the ASME, Vol.112, N2, p295-300, 1990.

3 Bejan, A., "The concept of irreversibility in heat exchanger design: counterflow heat exchangers for gas-to-gas applications", Journal of Heat Transfer, Transactions of the ASME, Vol.99, pp.374-380, August 1977.

4 Bejan, A., *Advanced Engineering Thermodynamics*, John Wiley & sons, Inc., chapter 11, 1988.

5 Carrington, C.G., and Sun, Z.F., "Second law analysis of combined heat and mass transfer phenomena", Int. J. Heat Mass Transfer, Vol.34, No.11, pp.2767-2773, 1991.

6 San, J.Y., Worek, W.M., and Lavan, Z., "Entropy generation in convective heat transfer and isothermal convective mass transfer", Journal of Heat Transfer, Transactions of the ASME, Vol.109, pp.647-651, August 1987.

7 Bejan, A., Second law analysis in heat transfer, Energy , Vol. 5, pp.721-732, 1980.

8 Sarangi, S., and Chowdhury, K., “On the generation of entropy in counterflow heat exchangers”, Cryogenics 63-65, 1982.

9 Sekulic, D.P., and C.V. Herman, “One approach to irreversibility minimization in compact cross flow heat exchanger design”, Intl. Comm. Heat Mass Transfer , 13, 23-32, 1986.

[10] Grazzini, G., and Gori, F., "Entropy parameters for heat exchanger design", Int. J. Heat Mass Transfer, Vol.31, No.12, pp.2547-2554, 1988.

[11] Reistad, G.M., “Availability: Concepts and Applications”, Ph.D. thesis, University of Wisconsin, Madison, 1970.

[12] Aceves-Saborio, S., Ranasinghe, J., and Reistad, G.M., "An extension to the irreversibility minimization analysis applied to heat exchangers", Journal of Heat Transfer-Transactions of the ASME, Vol.111, N1, p29-36, 1989

[13] Moran, M.J., Availability analysis: A guide to efficient energy use , Prentice-Hall, Englewood Cliffs, NJ, p.100, 1982.

[14] Witte, L.C., "The influence of availability costs on optimal heat exchanger design", Journal of Heat Transfer-Transactions of the ASME, Vol.110, N4A, p830-835, 1988.

[15] London, A.L., "Economics and the second law: an engineering view and methodology", International Journal of Heat and Mass Transfer, Vol.25, No6, pp743-751, 1982.

[16] Zubair, S.M., Kadaba, P.V., and Evans, R.B., "2nd-Law-based thermo-economic optimization of 2-phase heat exchangers", Journal of Heat Transfer-Transactions of the ASME, Vol.109, N2, p287-294, 1987.

[17] Bejan, A., "The concept of irreversibility in heat exchanger design: counterflow heat exchangers for gas-to-gas applications", Journal of Heat Transfer, Transactions of the ASME, Vol.99, pp.374-380, August 1977.

[18] Bejan, A., *Advanced Engineering Thermodynamics*, John Wiley & sons, Inc., chapter 5, 1988.

[19] Szargut, J., and Styrylska, T., “Die exergetische Analyse von Prozessen der feuchten Luft”, Heiz.-Lueft-Haustech , Vol. 20, pp. 173-178, 1969.

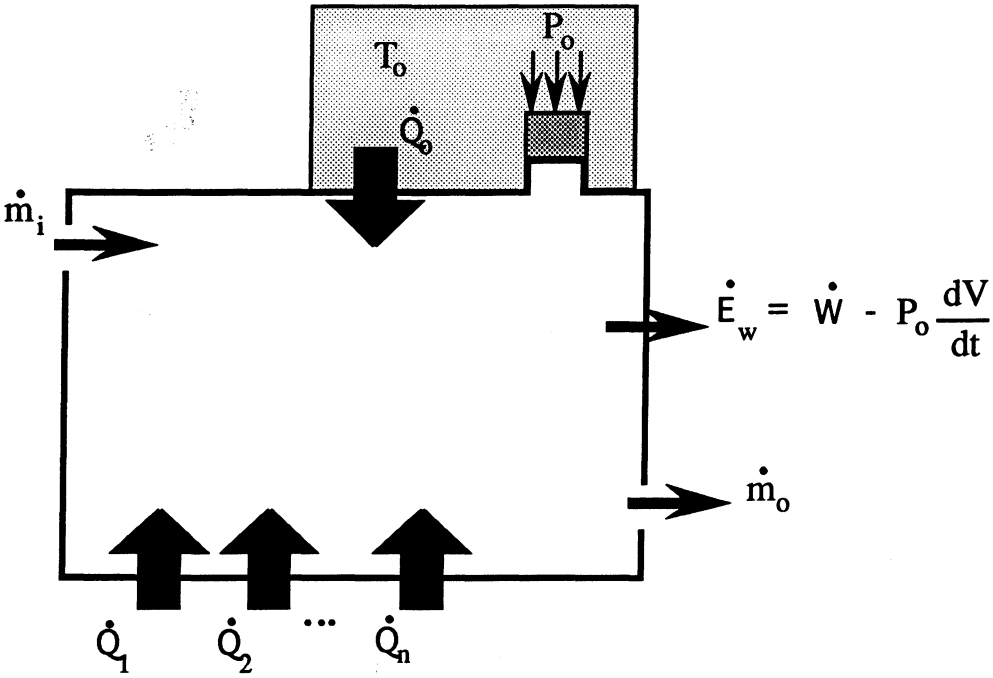

Figure 3.1 Open System in Thermal Contact with "n" Reservoirs [1]

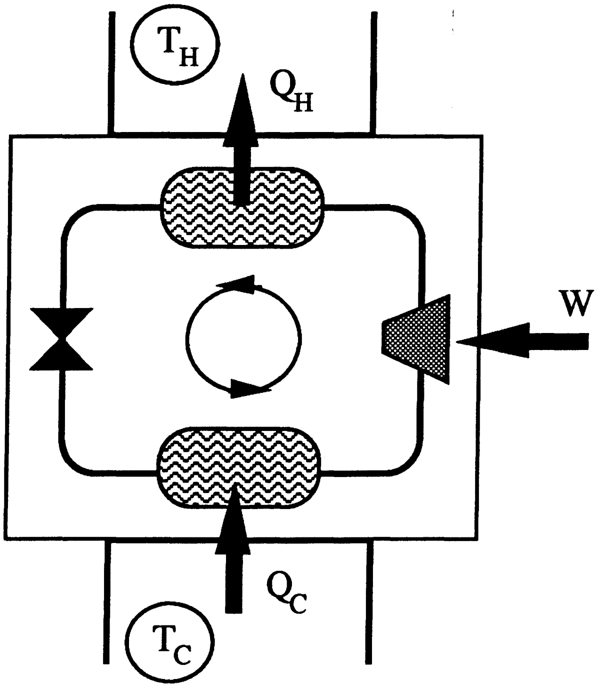

Figure 3.2 A Typical Air-Conditioning Cycle

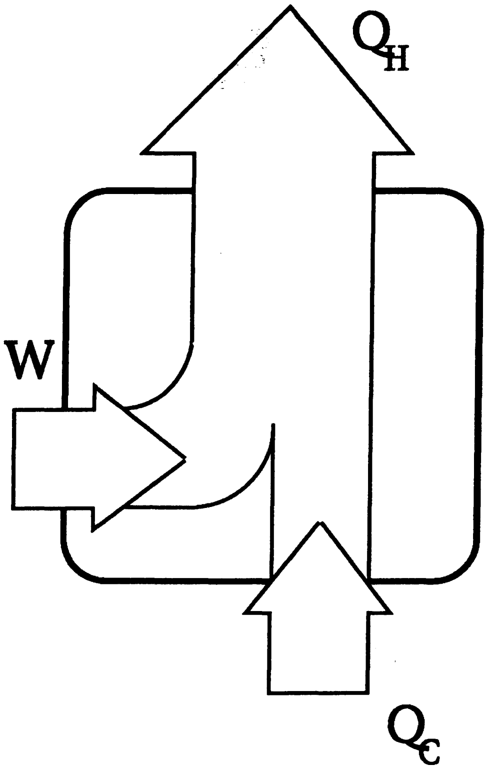

Figure 3.3a Energy Conservation [1]

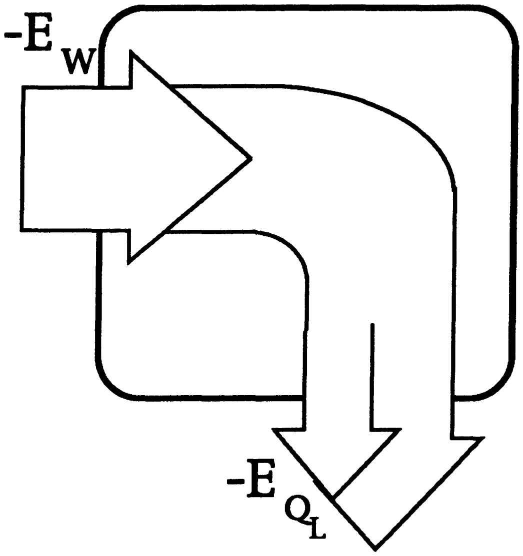

Figure 3.3b Exergy Destruction [1]

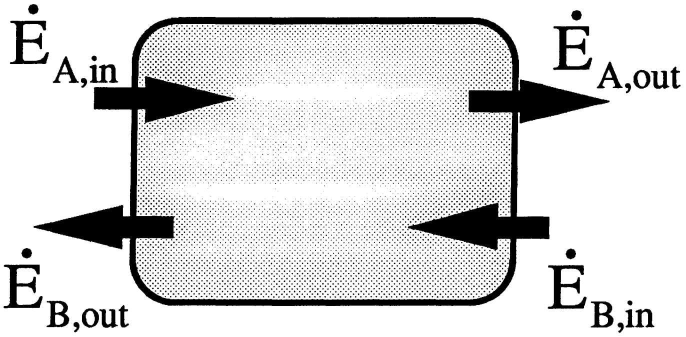

Figure 3.4 Generic Heat Exchanger with Fluids A and B Only (no condensate)

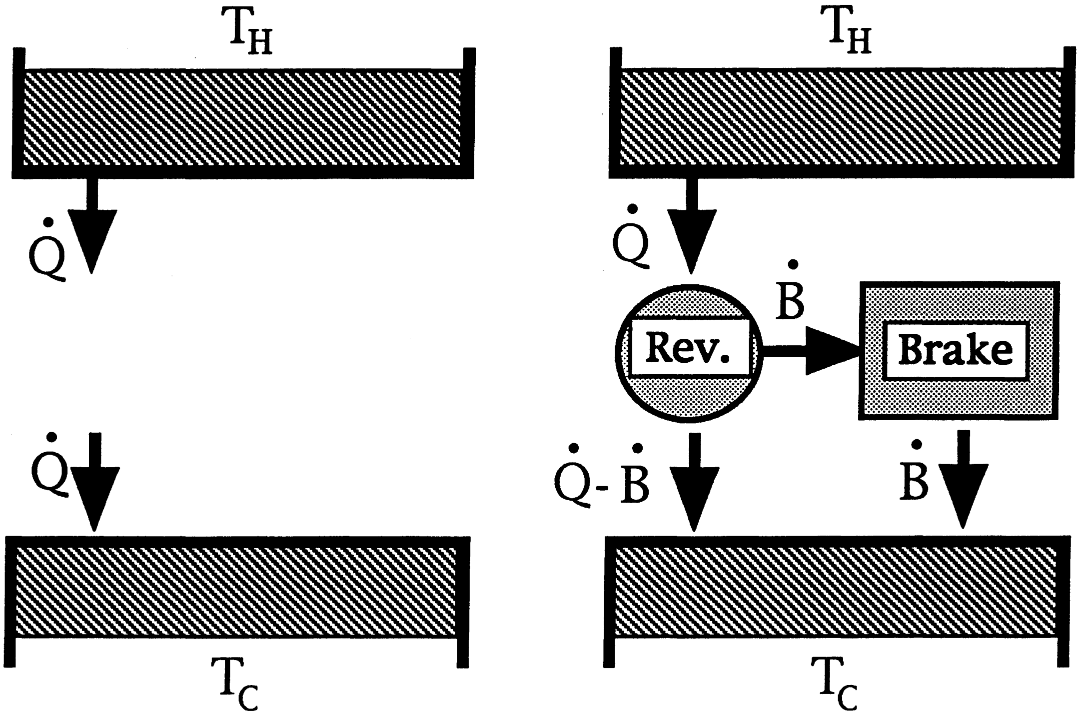

Figure 3.5 Irreversibilities Associated with Heat Transfer across a Finite Temperature Difference [4]

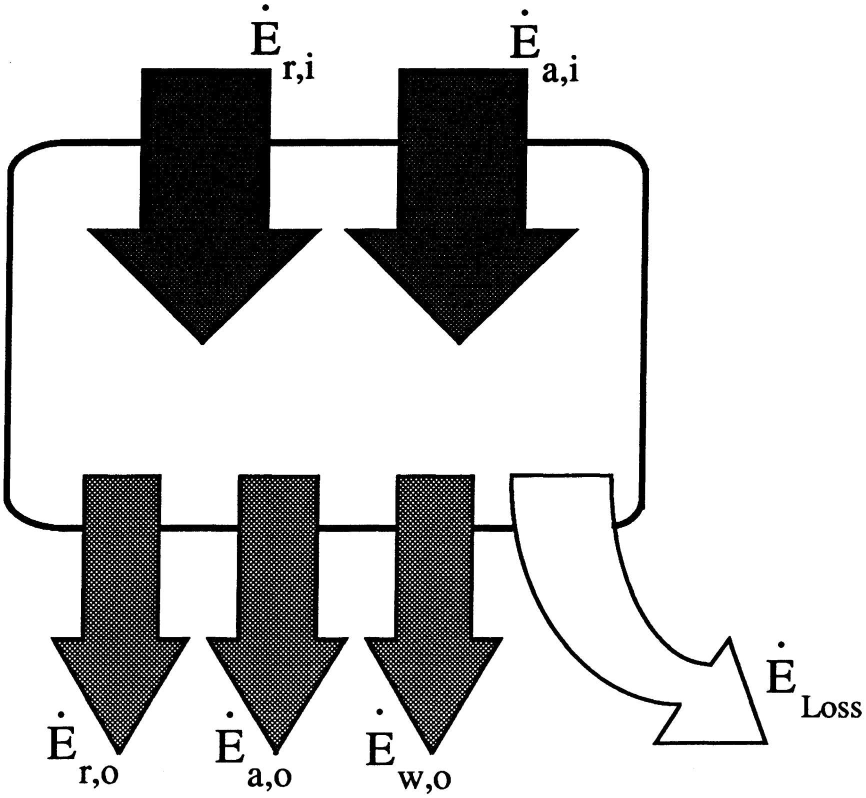

Figure 3.6 Evaporator Exergy Flow

CHAPTER 4

HEAT EXCHANGER MODELING

The case for selecting an irreversibility-based function in the thermodynamic optimization of heat exchangers was presented in Chapter 3. A common feature of the studies reviewed in that chapter is the modeling of heat transfer and pressure drop performance characteristics using sets of simultaneous algebraic equations.

For the present study, a more detailed heat exchanger model was developed and implemented in the optimization scheme to evaluate the irreversibility objective function. The model is based on fundamental principles and a finite difference approach, and is applicable to an arbitrary coil geometry with both pure and mixed refrigerants. A review of the literature on evaporator modeling is presented in the first section of this chapter. The second section describes the structure of the present model and the choice of a solution scheme.

The third section presents several methods used to model combined heat and mass transfer, and details their implementation in the model. A discussion of other local performance related calculations, such as refrigerant pressure drop, heat transfer correlations and fluid properties, is included in the fourth section. The evaluation of global exchanger performance parameters obtained with first and second law-based analysis is described in this section as well.

The fifth section summarizes the interfacing capabilities of the model. Finally, the sixth and seventh sections describe the simulation and design modes of the model, and its implementation in a full air-conditioning system computer simulation.

4.1 Evaporator Modeling: A Literature Review

Several evaporator models have been proposed in the literature, with a great diversity of modeling approaches, solution schemes and inherent assumptions. The level of complexity of a computer simulation is typically dictated by its intended purpose, subject to other unavoidable constraints such as computational speed. Thus, the main features of each model were reviewed with the intent of evaluating their applicability to the modeling effort which was part of this investigation.

Many models use a discretized equivalent exchanger geometry in order to simplify the analysis, while retaining a reasonable level of accuracy. Hill et al. [1] chose an equivalent single-pass cross flow exchanger, whereas Mirth et al [2] and Kahn [3] preferred an equivalent pure counterflow exchanger discretized in the direction of air flow. An alternative approach proposed by Oskarsson et al. [4] is to model a single representative tube of the heat exchanger.

Given the importance of design variables in the present study, an effort was made to keep the geometric characteristics of the coil in the analysis, along the lines of more detailed simulations by Domanski [5] and Poz [6]. Their models accomplished this by simulating the performance of each heat exchanger tube individually, an approach followed in the current model.

In all the models reviewed, the discretization of the heat exchanger performance equations yielded a set of algebraic equations. Elmahdy [7] and Kahn approximated the differential equations associated with each and every exchanger element using numerical derivatives, and solved the resulting set of algebraic equations simultaneously in matrix form.

Oskarsson et al., Hill et al. and Mirth et al. used an iterative approach to solve the governing heat, mass transfer and refrigerant pressure drop equations related to each heat exchanger element, as well as the overall evaporator solution.

The current model applies a simultaneous Newton-Raphson solution to a similar set of equations, an approach previously used with success in the modeling of condensers [8]. An iterative algorithm was adopted for the overall evaporator solution, as described in the following section. The main features of the models reviewed in this section are summarized in Table 4.1.

Table 4.1 Literature Review of Evaporator Models

Author	Approach	Comments
A.H., Elmahdy [7]	• Coupled heat, mass transfer equations solved numerically	
J.M., Hill S.M., Jeter 1991 [1]	• Discretized equivalent single pass cross-flow exchanger • Iterative exchanger solution	• Analytical solutions to the conservation equations within a control volume • Combined heat and mass transfer effectiveness for isothermal refrigerant volumes • Linearized air process path • Arbitrary but variable Lewis number
D.R., Mirth S., Ramadhyani D.C., Hittle 1993 [2]	• Pure counterflow heat exchanger discretized in the air direction • Iterative exchanger solution	• Enthalpy as driving potential for combined heat and mass transfer
A.Y., Khan 1994 [3]	• Pure counterflow heat exchanger discretized in the air direction • Coupled heat, mass transfer equations solved numerically • Iterative exchanger solution	• Variable Lewis number
S.P., Oskarsson K.I., Krakow S., Lin 1990 [4]	• Finite element model of a representative tube • Iterative solution for each element	• Thermal resistance network • Equivalent air heat transfer coefficient • Linearized air process path
P.A., Domanski 1989 [5]	• Tube-by-tube analysis • Iterative exchanger solution	• Thermal resistance network • Equivalent air heat transfer coefficient • Lewis number= 1.0 • 50% air mixing
M.Y., Poz J.C., Conklin 1994 [6]	• Tube-by-tube analysis	• Enthalpy as driving potential for combined heat and mass transfer • Linear and quadratic approximation for T_{ref}, analytical solutions for the air outlet conditions • Lewis number= 1.0
F. Ragazzi C.O. Pedersen 1995 (current model)	• Tube-by-tube analysis • Finite difference analysis of each tube • Local simultaneous solution • Iterative exchanger solution	• Three different heat and mass transfer models • Variable Lewis number • Variable air mixing

4.2 Structure of the Current Model

The model developed for the present study is based on a segment-by-segment solution, where a segment is defined as an entire heat exchanger tube or a portion of it. Its ability to simulate arbitrary flow configurations is greatly increased by allowing the user to describe the position of all segments relative to each other. This is done by specifying the dependence of the air and refrigerant inlet conditions to each segment on the outlet conditions of all other segments.

The main features of the solution algorithm are summarized in Figure 4.1, and presented in this section in general form. Due to the structured nature of the computer code, each major step in the solution scheme corresponds to a separate subroutine.

The objective of the iterative solution is to converge on a set of inlet air temperatures to all segments in the exchanger, so as to satisfy a previously specified set of relationships between the inlet and outlet air and refrigerant conditions of all segments. These temperatures, which are initially assumed equal to that of the air approaching the exchanger, change while the solution scheme progresses until convergence is reached. As shown in Figure 4.2.1, the values of the air inlet temperature to each and every segment are compared before and after each main iteration. If a change in at least one of these variables is recorded, the program moves on to analyze the performance of each and every segment one more time. The order in which it does so depends on the segment numbering by the user, but typically follows the direction of refrigerant flow. This logic is carried out in subroutine *hx_soln.*

Each segment is divided into an arbitrary number of modules, as shown in Figure 4.2, whose inlet conditions must be evaluated before analyzing the segment. The task of evaluating the module inlet conditions belongs to subroutine *seg_init* and consists of two parts. First of all, the air and refrigerant inlet conditions to the segment are evaluated by subroutine *seg_init* according to the pre-established tracing scheme. Energy and mass balances are enforced, as the air streams leaving specified neighboring segments mix to form the air stream approaching that particular segment, in order to obtain the desired air inlet enthalpies and humidity ratios. An energy balance is also enforced on the mixing refrigerant streams to evaluate the entering state of that fluid. Changes in the refrigerant pressure, due to frictional losses and elevation changes associated with return bends preceding a segment, are included in the evaluation of the refrigerant inlet conditions to a segment.

The second task of subroutine *seg_init* is to initialize all modules. The air inlet conditions to all modules in a given segment are assumed equal, and so they may be initialized once the air inlet conditions to the segment are available. On the refrigerant side, the inlet conditions to all modules in the segment are unknown, but those at the inlet to the segment may be used as initial guesses. Each module in the segment is initialized by subroutine *mod_init.*

Once initialized, each and every module in the segment is analyzed in sequential order by subroutine *seg_soln.* This subroutine evaluates the inlet conditions to the module, based on the most recent value of those at the outlet of the preceding module, and applies a simultaneous Newton-Raphson solution to the coupled heat, mass transfer and refrigerant pressure drop equations associated with each module. This algorithm is included in subroutine *nrsoln.*

The set of residual equations used in the simultaneous solution depends on the type of exchanger performance analysis selected by the user. Four different sets of equations are listed in subroutines *res_epsdry, res_epswet, res_disc* and *res_uawet,* corresponding to different types of analysis which are discussed in the following section.

4.3 Evaporator Heat and Mass Transfer Modeling

Analyzing the performance of evaporators is further complicated when they operate under wet conditions. One approach is to obtain a numerical solution of the discretized differential equations associated with heat and mass transfer, as done by Elmahdy [7]. This solution scheme was implemented in the current model, using arithmetically averaged air and refrigerant temperatures for each exchanger module.

Several simplifications of the original differential equations have been proposed, based on different assumptions, resulting in a variety of alternative heat and mass transfer models. Mirth [9] compiled a fairly extensive review of two such models, the *single* and *dual potential* methods, and compared their accuracy to that of a third improved method developed to handle partially wet fins. The single potential method is recommended by the industry standard [10] , whereas the dual potential method is a simpler alternative proposed by McQuiston [11]. Part of that review is reproduced in this section, along with a description of two additional methods, based on a resistance network and an exchanger effectiveness respectively, which were implemented in the current model.

4.3.1 Discretized Heat and Mass Transfer Equations

A complete set of differential equations, based on energy and mass balances, may be used to describe the combined heat and mass transfer processes associated with an infinitely small exchanger element. Discretization, excluding time-dependent effects, results in a set of numerical equations which may be solved in conjunction with the refrigerant pressure drop equation, for the five unknown variables h_{ro}, P_{ro}, T_{ao}, ω_{ao}, and $\overline{T}_s$.

$$\dot{m}_{ref} \cdot (h_{ro} - h_{ri}) = \dot{m}_{air} \cdot (h_{ai} - h_{ao}(T_{ao}, \omega_{ao})) \tag{4.1}$$

$$\dot{m}_{ref} \cdot (h_{ro} - h_{ri}) = h_{ref} \cdot dA_i \cdot (\overline{T}_s - \overline{T}_r(h_{ro}, P_{ro})) \tag{4.2}$$

$$\dot{m}_{ref} \cdot (h_{ro} - h_{ri}) = \dot{m}_{air} \cdot c_{p,a} \cdot (T_{ai} - T_{ao}) + \dot{m}_{air} \cdot (\omega_{ai} - \omega_{ao}) \cdot i_{fg} \tag{4.3}$$

$$\begin{aligned} \dot{m}_{ref} \cdot (h_{ro} - h_{ri}) = {} & \eta_{s,T} \cdot h_a \cdot dA_o \cdot (\overline{T}_a(T_{ao}) - \overline{T}_s) + \\ & \eta_{s,\omega} \cdot h_D \cdot dA_o \cdot (\overline{\omega}_a(\omega_{ao}) - \overline{\omega}_s(\overline{T}_s)) \cdot i_{fg} \end{aligned} \tag{4.4}$$

$$\Delta P_{calc}(h_{ro}, P_{ro}) = P_{ri} - P_{ro} \tag{4.5}$$

The surface efficiencies associated with the temperature and humidity ratio distributions, $\eta_{s,T}$ and $\eta_{s,\omega}$, are functions of the temperature and humidity ratio fin efficiencies, $\eta_{f,T}$ and $\eta_{f,\omega}$. These two surface efficiencies are assumed equal to each other in the analysis, and are replaced by a single surface efficiency, η_s. An additional simplification of the equations listed above relies on the heat and mass transfer analogy [12], which relates the air heat transfer and mass transfer coefficients.

$$h_D = \frac{h_a}{c_{p,a} \cdot Le^{1-n}} \qquad ,n = 1/3 \tag{4.6}$$

4.3.2 Single and Dual Potential Methods

Several alternative methods have been proposed in the literature to reduce the complexity of the system of equations presented above. A summary of the single and dual potential methods, used by Mirth in his comparison, is presented in this section.

The derivation of both methods may be divided into three major steps. First of all, an equation for the total heat transfer rate for a general increment of wet exchanger area is developed, according to the assumptions made in each method, as described in Table 4.2.

Table 4.2 Local Heat Transfer Rates: Single and Dual Potential Methods

	Single Potential Method	**Dual Potential Method**
General Equation	$dq = [h_a(T_a - T_s) + h_D(\omega_a - \omega_s)(i_{wv}(T_a) - i_w(T_s))]dA$	
General Assumptions	$i_{fg} = i_{wv}(T_a) - i_w(T_s)$ [9] $h_D = h_a / c_{p,ma} Le^{1-n} \quad , \; n = 1/3$ [12]	
Method-Dependent Assumptions	$(\omega_s - \omega_a) i_{fg} (1 - Le^{n-1}) << (i_a - i_s)$	$R_{ref} << R_{air}$
Local Heat Transfer Rate	$dq = \frac{h_a}{c_{p,ma}}(i_a - i_s)dA$	$dq = h_D i_{fg}(\omega_a - \omega_s)dA + U(T_a - T_w)dA$ $1/U = (1/h_a) + A_{air}R_{tube} + (A_{air}/h_{ref}A_{ref})$

These expressions are then applied to an incremental fin area to obtain and solve a differential equation describing the temperature distribution along the fin. With the fin temperature distribution at hand, it is then possible to derive an expression for the fin efficiency using a solution similar to that obtained by Gardner [13] for dry fins. Fin efficiencies are used to model the reduction in heat transfer associated with a finned surface, relative to that of a primary surface, which is caused by a drop in the driving temperature difference between the air and the fin surface. Different fin efficiency expressions are obtained for each method, as shown in Table 4.3.

Table 4.3 Fin Efficiency: Single and Dual Potential Methods

	Single Potential Method	**Dual Potential Method**
General Assumptions	$\eta_{fin,hexagonal\ cell} \cong \eta_{fin,annular}$ [14] $\eta_{fin,annular} \cong \eta_{fin,straight,L_{eq}}$ [15]	
Local Heat Transfer Rate for dA_{fin}	$dq_{fin} = \frac{h_a}{c_{p,ma}}(i_a - i_{s,fin})dA_{fin}$	$dq_{fin} = [h_a(T_a - T_{s,f}) + (h_a/c_{p,ma}Le^{1-n})i_{fg} * (\omega_a - \omega_{s,f})]dA_{fin}$
Method-Dependent Assumptions	$dq_{fin} = h_{eff}(T_{wb,a} - T_{s,f})dA_{fin}$ $h_{eff} = h_a \cdot m'/c_{p,ma}$ $m' = \frac{i_a - i_{s,f}}{T_{wb,a} - T_{s,f}}$ $m' \cong \frac{di}{dT}\ at\ \overline{T}_s$ [16]	[11] $C_{base} = \frac{\omega_{f,base} - \omega_a}{T_{f,base} - T_a}$ or [9] $C_{avg} = \frac{C_{base} + C_{tip}}{2}$

	Single Potential Method	Dual Potential Method
Fin Efficiency	$\eta_{fin} = \frac{tanh(mL_f)}{mL_f}$ $m^2 \cong \frac{2h_{eff}}{k_f \delta_f}$	$\eta_{fin} = \frac{tanh(ML_f)}{ML_f}$ $M^2 = function(C)$ $\cong constant$

Finally, the total heat transfer for the heat exchanger may be calculated according to the method selected. With the single potential method, the total heat transfer rate is based on the *log-mean enthalpy potential* of the exchanger [17], making it difficult to separate its sensible and latent contributions. The dual potential method proposed by McQuiston, on the other hand, allows for the independent evaluation of each contribution. The sensible term is obtained with a resistance-type equation based on the temperature difference between the refrigerant and the air temperatures. The latent term, on the other hand, depends on the humidity ratio potential between the saturated condensate and the air conditions. Both calculations include the air resistance, and therefore the fin efficiency previously discussed.

Mirth applied both methods, in addition to his own, to a discretized cooling coil using water as a refrigerant. The capacity predictions obtained with the single potential method were within 1% of those obtained with his more fundamentally sound approach. The dual potential method, however, consistently over predicted the exchanger capacity by 4-8% [9].

Mirth traced the source of these erroneous predictions back to the fundamental assumptions made by McQuiston, namely a negligible refrigerant side resistance and an approximated proportionality constant, C_{base}. The capacity results were improved to within 1% of those of the single potential method using a different proportionality constant, C_{avg}, based on both tip and base fin conditions.

4.3.3 Thermal Resistance with Equivalent Air Heat Transfer Coefficient

In the current evaporator simulation, the coil is discretized in the direction of refrigerant flow. Hence, the rate of heat transfer from air to refrigerant for a given module may be expressed in terms of a *composite wall* type thermal resistance equation using the local temperature driving potential, as described by Oskarsson [18].

$$dq = \frac{\overline{T}_a - \overline{T}_r}{\dfrac{1}{(h_a + h_L) \cdot dA_o \cdot \eta_s} + \dfrac{1}{h_{ref} \cdot dA_i}} \tag{4.7}$$

where

$$h_L = \frac{h_a \cdot i_{fg}}{c_{p,ma} \cdot Le^{1-n}} \cdot \frac{\overline{\omega}_a - \overline{\omega}_s}{\overline{T}_a - \overline{T}_s} \quad , \ (n = 1/3) \tag{4.8}$$

Arithmetic averages over the whole exchanger module are used in Equations (4.7) and (4.8) for the condensate surface temperature and humidity ratio, and the air and refrigerant temperatures.

The fin efficiency accounts for the non-uniformity of the temperature distribution within a fin. The surface efficiency, η_s, on the other hand, accounts for the bare tube surface areas associated with the module.

$$\eta_s = 1 - \frac{dA_{fin}}{dA_{total}} \left(1 - \eta_{fin}\right) \tag{4.9}$$

Additional equations, corresponding to the heat transfer rate based on the air enthalpy change and a to resistance network between the air and the condensate surface, are

$$dq = \dot{m}_{air} \cdot (i_{ai} - i_{ao}) \tag{4.10}$$

and

$$dq = \frac{\overline{T}_a - \overline{T}_s}{\dfrac{1}{(h_a + h_L) \cdot dA_o \cdot \eta_s}} \tag{4.11}$$

The number of independent unknown variables may be reduced with the assumption of a linearized de-humidification process. This amounts to defining the condensate surface state as the intersection between the saturation curve and an extension of the straight line passing through the inlet and outlet air states on the psychometric chart, as shown in Figure 4.3. The linearization of the air path is justified by the fact that an exchanger module is likely to follow a fraction of the total air path associated with the entire evaporator.

With this assumption, the air outlet humidity ratio can be expressed as a function of other unknown variables.

$$\omega_{ao} = \overline{\omega}_s + (\omega_{ai} - \overline{\omega}_s) \cdot \frac{T_{ao} - \overline{T}_s}{T_{ai} - \overline{T}_s} \tag{4.12}$$

where the saturation humidity ratio is a function of the condensate saturation temperature alone.

This completes a set of simultaneous equations, with the air outlet, refrigerant outlet and surface temperatures as unknowns. A simultaneous Newton-Raphson solver is used in the current model to solve these and the refrigerant pressure drop equations, as opposed to the successive substitution solution implemented by Oskarsson. Regardless of the choice of solution scheme, the slope of the air path is re-evaluated at each iteration step as the condensate temperature converges towards a solution.

4.3.4 Equivalent Evaporator Effectiveness for Wet Coils

A major disadvantage of the resistance network approach is that it requires driving potentials representative of the entire module. Whether these be log-mean or arithmetic averages, they are certain to involve both the air and refrigerant outlet conditions, thus increasing the number of unknown variables and the complexity of the solution. One way to simplify the heat transfer rate calculations in the analysis of discretized coils is to apply the effectiveness-NTU method [19], which is based on the inlet temperature driving potential. This solution scheme was successfully implemented in the simulation of condensers and evaporators operating under dry surface conditions, treating each module as a separate heat exchanger [8].

Applying this method to processes involving combined heat and mass transfer is more complicated. Hill proposed a generalized effectiveness-NTU heat flux equation for combined heat and mass transfer applicable to each finite volume element of a discretized coil, with the assumption of isothermal refrigerant within that volume. In the absence of mass transfer, the equations reduce to the more common effectiveness-NTU expressions associated with heat exchangers with infinite capacity ratios, such as those operating with two-phase pure refrigerants.

A similar generalized effectiveness-NTU heat flux equation for combined heat and mass transfer is proposed for heat exchangers with finite capacity ratios. This is needed to analyze evaporator modules with single phase or two-phase zeotropic refrigerants, accounting for gradients in the refrigerant temperature within those modules. The derivation presented by Ragazzi [39] is an extension of the work of Hill [1], and was based on the analysis of dry exchangers by Kays and London [19].

An equivalent effectiveness was defined for the wet coil case, namely

$$\varepsilon_{wet} = \frac{dq_{\,actual}}{dq_{\,max}} \tag{4.13}$$

As in the dry case, different expressions were obtained for the effectiveness depending on which fluid has the minimum capacity rate. With Γ as defined by Ragazzi [39], the effectiveness equations corresponding to $\dot{C}_{min} = \dot{C}_a = \dot{C}_{unmixed}$ and $\dot{C}_{min} = \dot{C}_r = \dot{C}_{mixed}$ reduced to,

$$\varepsilon_{wet} = \frac{c_1}{(1-c_2)} \cdot \frac{\dot{C}_r}{\dot{C}_a} \cdot \left(1 - exp\left(-\frac{(1-c_2)}{c_1} \cdot \frac{\Gamma \cdot \dot{C}_a}{\dot{C}_r}\right)\right) \tag{4.14}$$

$$\varepsilon_{wet} = \frac{c_1}{(1-c_2)} \cdot \left(1 - exp\left(-\frac{(1-c_2)}{c_1} \cdot \frac{\Gamma \cdot \dot{C}_a}{\dot{C}_r}\right)\right) \tag{4.15}$$

The total rate of heat transfer can be calculated with,

$$dq = \varepsilon_{wet} \cdot \dot{C}_{min} \cdot \left(T_{ai} + \frac{c_0}{c_1} - (1 - \frac{c_2}{c_1}) \cdot T_{ri}\right) \tag{4.16}$$

In the absence of mass transfer, the equations derived above reduce to the more familiar effectiveness-NTU equations listed in Kays and London [19] for cross flow heat exchangers with one fluid mixed.

4.4 Local Exchanger Performance Calculations

All the methods discussed above involve the calculation of air and refrigerant side heat transfer coefficients. This section describes the approach used to evaluate these coefficients locally for each heat exchanger module under various types of operating internal and external conditions. In addition, the calculation of local refrigerant pressure drops is discussed for both single and two-phase pure or mixed refrigerants.

4.4.1 Air-Side Heat Transfer

The air-side convective heat transfer coefficient is typically based on a j-factor, defined as

$$j_f = St \cdot Pr^{2/3} \tag{4.17}$$

Substituting for the Stanton number, St, the air-side heat transfer coefficient becomes,

$$h_a = \frac{j_f \cdot c_{p,a} \cdot G_{max}}{Pr^{2/3}} \tag{4.18}$$

where G_{max} is the air mass flux based on the minimum free-flow area.

The value of the non-dimensional j-factor is influenced by the presence of dehumidification, and the variation in airflow patterns from one row to the next. Global and local j-factor correlations for dry and wet coils are presented in the following sections.

4.4.1.1 Average Dry J-factors

Several j-factor correlations are available in the literature for coils with various fin types operating under dry conditions. These correlations relate the j-factor to the air Reynolds number based on the minimum free-flow area, *Re*, and the coil geometrical dimensions. In general, a single correlation is used to provide average j-factor values for heat exchangers with four or more rows, neglecting any j-factor dependency on the number of rows. Rich [20] examined the effect of the number of rows on heat transfer performance in his analysis of coils with less than four rows. For such coils, the row number is included in the average j-factor correlations, along with the air Reynolds number and the value of the j-factor obtained for the four row case.

McQuiston [21] analyzed experimental results from several investigators, including his own, and presented j-factor correlations for four-row coils, as well as for coils with less than four rows. A different correlation, proposed by Gray and Webb [22], was used by Domanski et al. [5] and Hill et al. [1], and was implemented in the current model. Gray et al. developed their correlation for flat finned heat exchangers, and introduced a correction factor for exchangers with less than four rows,

$$j_{f,N} = j_{f,4} \cdot 0.991 \cdot \left[2.24 \cdot Re^{-0.092} \cdot \left(\frac{N}{4} \right)^{-031} \right]^{0.607 \cdot (4-N)} \tag{4.19}$$

where $j_{f,4}$ is the j-factor obtained for $N \geq 4$.

Elmahdy [7], on the other hand, assumed a general relationship between the heat transfer j-factor and the air Reynolds number,

$$j_f = c_{f,1} \cdot Re^{c_{f,2}} \tag{4.20}$$

The values of $c_{f,1}$ and $c_{f,2}$ may be considered constant for a particular coil over the Reynolds number range $200 < Re < 1500$ [7]. A regression analysis with previously published test data of twenty different heat exchangers was used to obtain expressions for $c_{f,1}$ and $c_{f,2}$ in terms of non-dimensional parameters related to the physical dimensions of the coil.

A similar effort to generalize results obtained with experimental data was made by Mirth [2]. Mirth developed a Nusselt number correlation based on dry-surface experimental data collected with five different cooling coils. The non-dimensional parameters involved in this correlation include the air Prandtl and Reynolds numbers, as well as several variables related to the coil dimensions.

The general approach in the development of the aforementioned correlations consists of data collection with several coils, the formulation of an air side heat transfer correlation, and its validation with experimental data from the literature. Some of the problems associated with each of these steps should be considered when applying such correlations to an unknown coil. First of all, there are experimental errors associated with the collection of the original data, in addition to those introduced by the curve-fit itself. More importantly, the formulation of the correlation may have been tailored to the analysis of the coils tested in a particular study. This includes the choice of parameters, such as the length used in the Reynolds number. If this length does not vary substantially from one of the coils tested to the next, for example, the correlation may incorrectly suggest a lack of dependency of the j-factor on this particular parameter.

Other errors may be incurred in the validation of the correlation with experimental data from the literature. The accuracy of the reported data should be questioned, together with the definitions of variables such as Nusselt numbers or heat transfer coefficients. Finally, fin type is an important consideration when selecting a heat transfer coefficient correlation, and the values of the non-dimensional parameters describing the fin shape and size should be within the range of the correlation.

4.4.1.2 Average Wet J-factors

Condensate formation on the fin surface not only adds a latent load to the overall heat transfer equation, but may also affect the value of the air side convective heat transfer coefficients. Efforts to account for this effect range from the development of separate wet j-factor correlations to the substitution of wet with dry heat transfer coefficients.

Oskarsson et al. [4] chose the latter approach, whereas Elmahdy [7] introduced a correction factor to relate the wet and dry j-factors. This correction factor was correlated in terms of the air Reynolds number using his own experimental data, in order to generalize the validity of the wet j-factor correlation.

Mirth [2] conducted a thorough analysis of his experimental data, collected under both dry and wet conditions, and concluded that wet-surface heat transfer performance may be accurately predicted using dry-surface heat transfer correlations. Heat transfer predictions using dry-surface Nusselt numbers were within +/-5% of the wet-surface experimental results.

Such results are not surprising, considering the lack of sensitivity of the heat transfer predictions to variations in the air-side heat transfer correlations. This lack of sensitivity becomes more severe as the coil asymptotically approaches its maximum possible heat transfer rate for a set of given refrigerant-side conditions. On the other hand, errors in the order of 20% are involved in the calculation of air heat transfer coefficients from heat transfer data [2]. This is exacerbated in the wet-surface case by the uncertainty and non-repeatability associated with the dew point temperature measurement and the latent heat transfer rate determination.

Both the experimental and the theoretical evaluation of the latent heat transfer rate are important when using a heat exchanger model for data reduction to obtain wet-surface heat transfer coefficient correlations. First of all, it is essential to measure the latent portion of the load accurately if a correlation is to be developed by forcing the model to match the experimental data. In addition, the method chosen for the heat transfer rate calculation influences the results for a given air heat transfer coefficient. Mirth found discrepancies in the order of 5% between heat transfer rates calculated using the single and the dual potential methods described in a previous section.

While showing the wet-surface j-factor calculation to be unreliable, Mirth's results were not conclusive concerning the relative magnitude of the wet and dry j-factors. His wet-surface results are scattered, with values above and below their dry-surface counterparts. This is contrary to the findings of Eckels et al. [23], Myers [24], and Elmahdy [7], who reported an enhancement of the heat transfer coefficient under wet conditions. In general, observations of either heat transfer enhancement or degradation during condensation depend on the heat exchanger geometry and air-side Reynolds number.

Idem et al. [25] have recently looked at possible heat transfer performance enhancement due to condensate formation on the fin surfaces. Local variations in the convection coefficient, related to disturbances in the flow pattern caused by droplets or surface irregularities, is the proposed mechanism responsible for the heat transfer enhancement. For high Reynolds numbers, Hu and Jacobi [26] reported increases in the wet heat transfer coefficient .

4.4.1.3 Local J-factors

Local values of the air-side heat transfer coefficient are required in the evaporator simulation to evaluate the air side resistance to heat transfer of a module. Domanski [5] proposed a method to calculate the air-side j-factor for a module in a given row, based on the assumption that each row weights equally on the average air-side heat transfer coefficient of the entire heat exchanger. This method was adopted in the current model and is given by,

$$j_{f,row\,N} = N \cdot j_{f,N} - (N-1) \cdot j_{f,N-1} \tag{4.21}$$

where $j_{f,N}$ and $j_{f,N-1}$ are the average j-factors for heat exchangers with N and $(N-1)$ depth rows respectively.

For the analysis of an arbitrary heat exchanger module in the N^{th} row, average j-factors $j_{f,N}$ and $j_{f,N-1}$ are first evaluated with Equation (4.19) for two imaginary coils with N and $(N-1)$ rows respectively. Both average j-factors are based on the air mass flow rate over the entire heat exchanger. The local j-factor for the desired row is then calculated with Equation (4.21). Finally, the local air-side heat transfer coefficient can be obtained from the local j-factor with Equation (4.17)

4.4.2 Refrigerant-Side Heat Transfer

The refrigerant-side resistance to heat transfer is evaluated in terms of the internal surface area of the exchanger module and the average refrigerant heat transfer coefficient by subroutine *Rref_calc*. Internal enhancements are not accounted for in the current model, which is equivalent to assuming an inside surface efficiency equal to unity.

4.4.2.1 Average Refrigerant Heat Transfer Coefficients

For those modules in which no phase transition occurs, the average refrigerant heat transfer coefficient is assumed equal to the local coefficient based on the inlet refrigerant conditions to the module. When a phase transition does occur within the module, however, it is particularly important to evaluate an average refrigerant coefficient which is representative of the entire module. The presence of discontinuities in the refrigerant heat transfer coefficient may lead to convergence problems during the simultaneous solution of the coupled heat transfer and pressure drop equations associated with a transition module.

Transition modules are easily identified by comparing the inlet and outlet refrigerant qualities. When a change in refrigerant phase is determined, the fraction of the module length in the outlet phase is approximated as a function of the refrigerant enthalpies at the inlet and outlet to the module, and the dew or bubble refrigerant enthalpy, depending on the nature of the phase transition.

The resulting length fraction is then used to obtain the desired average refrigerant coefficient as a weighted sum of the local refrigerant coefficients based on the inlet and outlet refrigerant conditions to the module.

4.4.2.2 Local Refrigerant Heat Transfer Coefficients

Local heat transfer coefficients are evaluated for single and two-phase pure or mixed refrigerants using correlations from the literature. For single phase refrigerant, the model uses a familiar correlation proposed by Dittus and Boelter [27] for forced convection heat transfer and fully developed refrigerant flow inside a tube.

Many of the correlations available for evaporating refrigerant tend to lose accuracy at high refrigerant qualities, when the assumption of an annular flow regime is no longer valid. A correlation developed by Wattelet [28] for annular flow is used for qualities between 0.0 and 0.9. For evaporating refrigerant in the wavy-stratified flow regime ($0.9 < \text{quality} < 1.0$), the heat transfer coefficient is calculated as a weighted average of the two-phase coefficient for annular flow at a quality of 0.9, and the single phase coefficient for saturated vapor. This approach was first suggested by Domanski [5] and is described in subroutine *href_tp*.

The correlation proposed by Wattelet involves the calculation of the total evaporative heat transfer coefficient for pure refrigerants as a function of its convective and nucleate boiling contributions. This correlation was modified, as recommended by Bivens and Yokozeki [29] , in order to account for the heat transfer degradation resulting from mass transfer resistance. Bivens and Yokozeki developed an empirical correction factor based on data for zeotropic refrigerants from a variety of sources, and used it to adjust the coefficient obtained with a pure refrigerant correlation following an approach originally proposed by Gropp and Schlunder [30]. The generalized evaporative heat transfer correlation is described in subroutine *href_Watt.*

4.4.3 Refrigerant Pressure Drop

The change in refrigerant pressure in each evaporator module is calculated including both friction and acceleration effects. In addition, the refrigerant pressure drops in the heat exchanger return bends, associated with both gravity and friction effects, are evaluated as described in subroutine *returnbend.*

Gravity-related changes in refrigerant pressure result from the change in elevation between two horizontal heat exchanger modules connected by a return bend. For two-phase refrigerant, a homogeneous model is assumed in order to calculate an average refrigerant density based on the dew and bubble densities and the refrigerant quality. Friction effects are only included for two-phase refrigerant with a correlation proposed by Paliwoda [31].

For single phase refrigerant, the pressure drop component of a module due to friction is calculated using a friction factor in subroutine *fanningdp.* The friction factor dependence on refrigerant Reynolds number varies with flow regime, laminar or turbulent, as shown in subroutine *fannfact.*

For two-phase refrigerant, a separated flow model [32] is used to calculate the friction pressure gradient as a function of that which would result if the vapor fraction of the two-phase flow were alone in the tube. The friction pressure gradient of the vapor is based on a single phase friction factor, and the two-phase friction multiplier is evaluated using a correlation by Soliman [33].

The acceleration effects for both single and two-phase refrigerant are calculated by integrating the momentum conservation equation numerically from the module inlet to outlet conditions [8], as described in subroutine *pmom-calc*. Average refrigerant specific volumes are based on the dew and bubble specific volumes, refrigerant quality and refrigerant void fraction. The latter is calculated with one of the correlations reviewed by Butterworth [34].

4.4.4 Air and Refrigerant Properties

Every heat transfer or pressure drop calculation involves thermodynamic and thermophysical air or refrigerant properties.

Refrigerant thermophysical properties are evaluated using polynomial fits of data generated with an available computer package [35] for both pure and mixed refrigerants. Thermodynamic properties, on the other hand, are obtained using linear interpolation from tables generated with the same computer package [36].

4.4.5 Additional Performance Calculations

The modular values of several air, refrigerant and miscellaneous variables are continuously saved in storage arrays throughout the iterative exchanger solution. After convergence of the evaporator solution, these arrays are used to evaluate both local and global output parameters.

Local parameters, such as module air and refrigerant resistances to heat transfer, refrigerant pressure drop contributions and irreversibility components, are calculated in subroutine *mod_finanl*. Subroutine *hx_finanl*, on the other hand, is used to evaluate global exchanger parameters. These are based on average air and refrigerant conditions at the inlet and outlet to the exchanger, and include sensible and latent heat transfer rates, air and refrigerant pressure drops, and total irreversibility components.

The second-law analysis of the exchanger deserves particular attention. This is performed by subroutine *hx_2ndLaw* and takes into account irreversibilities related to heat transfer, pressure drop and air mixing. An effort to isolate the various contributions to the total exchanger irreversibility was made using different control volumes for the analysis of each exchanger module, as described in Chapter 6.

4.5 Evaporator Model Interfacing

For all practical purposes, the entire evaporator model may be treated as a single subroutine, *hx_model*, which evaluates the air and refrigerant outlet states for a given set of operating conditions. The geometric characteristics of the exchanger need to be specified as well with the help of files *in.hxinfo*, *in.seginfo*, and *in.lsegments*. These input files contain information related to the physical dimensions of the coil, the discretization scheme selected for its modeling, and the positioning of the exchanger modules relative to each other.

All input operations are carried out in subroutine *input*, also responsible for evaluating the exchanger operating conditions. This task depends on the intended use of the model and may be accomplished in three different ways. The first and simplest option is to simulate the operation of the exchanger for an arbitrary number of operating conditions using a single input file, *testinp_dat*. The outputs of the model are written to two types of files, *profle.out* and *finl.out*, by subroutines *output_test* and *output_final* respectively. The first type of file contains profiles of an arbitrary set of air, refrigerant and miscellaneous variables along the evaporator length, chosen by the user from a list of available local outputs. A separate *profle.out* file is created for each set of operating conditions, and labeled in numerical order. Global exchanger output variables, on the other hand, are written to a single file, *finl.out*.

The second mode of operation was developed for the validation of the computer simulation, allowing for the direct comparison of experimental and modeling results. The evaporator operating conditions are read from an arbitrary single file, *matrix_test*, which also contains the values of experimental results. Global modeling results can then be compared to their experimental counterparts and stored, along with the numerical results of that comparison, in the same file by subroutine *output_add*. This approach substantially facilitates the model validation process, and may be extended to the comparison of modeling outputs with any other set of results, experimental or otherwise. Due to the large size of file *matrix_test*, however, it may be desirable to print selected vector components, corresponding to separate variable values for various operating conditions, to a reduced output file. This is accomplished by subroutine *viewfile*. As in the previous mode of operation, local modeling results are written to separate *profle.out* files, corresponding to different sets of operating conditions.

Finally, the implementation of the evaporator model in a larger simulation program was considered, and the input process of operating conditions was modified accordingly. For this mode of operation, the use of global variables was preferred in order to make the values of the operating parameters available to the exchanger model. These global variables were added to the existing *include* files, and may be evaluated anywhere in the main simulation program. Global variables are widely used within the evaporator model in order to make the values of several general and segment-specific variables available to individual subroutines. A more complete description of these global variables is included in files *hx.inc*, *segment.inc* and *refprop.inc*.

The global output variables may also be made available to the system simulation through the use of global variables, or written to a separate output file of type *finl.out*. Once again, local modeling results are written to separate *profle.out* files, corresponding to different sets of operating conditions. The three different modes of interfacing described in this section are summarized in Figure 4.4.

4.6 Design and Simulation Modes

The first two ways of interfacing with the evaporator model described in the previous section are limited to a description of the heat transfer, pressure drop and dehumidification processes that take place within the evaporator for a given set of air and refrigerant entering conditions. This type of sequential analysis of the exchanger is referred to as the *simulation* mode. In order for the evaporator model to become a complete design tool, its capabilities were expanded so that model input and output parameters could be interchanged as variables in the exchanger solution. For example, it may be desirable to compare the performance of two different evaporator designs operating at the same heat transfer capacity rate but with a variable refrigerant pressure.

This type of variable switching, in which an arbitrary number of input parameters are allowed to float while an equal number of output parameters are held constant, was accomplished by treating the model as a non-linear function call in a set of residual equations solved using a global Newton-Raphson solution. A typical residual equation of this kind is shown below,

$$Residual^k = X^k_{out}\Big|_{set} - X^k_{out}(X^i_{in}, i = 1,n) \tag{4.22}$$

where X^k_{out} is an arbitrary output model parameter and X^i_{in} is one of n input model parameters.

A simultaneous equation solver used by Mullen [37] for the modeling of room air-conditioning systems was combined with the current evaporator model in order to obtain a *design* mode of the model. The model interfaces with the solver using global variables according to the third operating mode described in the previous section.

Additional global variables were added so that the refrigerant type, evaporator design type, and level of output interaction could be determined in an input file to the overall Newton-Raphson solver. Different input files are required by the evaporator model for each exchanger design type, and these were labeled according to a previously stipulated numbering of exchanger types. Each type corresponds to a different set of geometric dimensions and circuitry arrangements.

Selecting the level of output interaction allows the user to decide on whether or not to create local and global output variable files, an option which is also available in the *simulation* mode. The use of a generalized input file to drive the general solver greatly simplified the parametric studies involved in this investigation.

4.7 System Simulation

Both the *simulation* and *design* modes discussed above were aimed at modeling heat exchanger performance independently of system effects. Nygaard [38] has considered these effects by implementing the evaporator model along with a set of simultaneous non-linear residual equations developed to describe the performance of a full air-conditioning system. The development of the system model followed a similar approach to that of the *design* version of the evaporator model. Input and output evaporator model variables are stored globally, and additional residual equations were included to account for the other components in the system.

Some of the system results obtained by Nygaard are presented in Chapter 6 and compared to those at the component level under equivalent air-side and evaporator loading conditions.

4.8 Summary

An evaporator model was developed as part of this study, in order to evaluate the irreversibility objective function introduced in the previous chapter.

A review of the literature on evaporator modeling was presented in this chapter, followed by a description of the current simulation program. This included a description of several combined heat and mass transfer models, as well as other related heat transfer, pressure drop, and property calculations.

The last portion of the chapter described the design and simulation modes of the model, and its implementation in a full air-conditioning system simulation. The experimental validation of this model will be discussed in the next chapter.

4.9 References

[1] Hill, J.M., and S.M. Jeter, "A linear subgrid cooling and dehumidification coil model with emphasis on mass transfer", ASHRAE Transactions, 1991.

[2] Mirth, D.R., Ramadhyani, S., and Hittle, D.C., "Thermal Performance of Chilled-water Cooling Coils Operating at Low Water Velocities", ASHRAE Transactions, Vol. 99, Part 1, pp.43-53, 1993.

[3] Khan, A.Y., "Heat and mass transfer performance analysis of cooling coils at part-load operating conditions", ASHRAE Transactions, Vol.100, Pt.1, 1994.

[4] Oskarsson, S.P., K.I. Krakow, and S. Lin, "Evaporator models for operation with wet and frosted finned surfaces, part 2: Evaporator models and verification", ASHRAE Transactions, Vol. 96, Pt. 1, 1990.

5 Domanski, P.A., "EVSIM- An evaporator simulation model accounting for refrigerant and one-dimensional air distribution", NISTIR 89-4133, U.S. Dept. of Commerce, August 1989.

6 Poz, M.Y., and Conklin J.C., "Heat Exchanger Analysis for Non-azeotropic Refrigerant Mixtures", ASHRAE Transactions, V.100, Part I, 1994.

7 Elmahdy, A.H., "Analytical and experimental multi-row, finned-tube heat exchanger performance during cooling and dehumidification processes", Ph.D. dissertation, Carleton University, Ottawa, Canada, 1975.

8 Ragazzi, F., "Modular-based computer simulation of an air-cooled condenser", M.S. thesis, University of Illinois at Urbana-Champaign, 1991.

9 Mirth, D.R., "Experimental Studies and Mathematical Modeling of Chilled-Water Cooling Coils", Ph.D. thesis, Purdue University, 1993.

10 *ARI Standard 410-87, Forced-circulation air-cooling and air-heating coils*, Air-Conditioning and Refrigeration Institute, 1987.

11 McQuiston, F.C., "Fin efficiency with combined heat and mass transfer", ASHRAE Transactions, Vol. 81, Pt. 1, pp. 350-355, 1975.

12 Incropera, F., and DeWitt, D., *Fundamentals of Heat and Mass Transfer*, John Wiley and Sons, New York, 1990.

13 Gardner, K.A., "Efficiency of extended surface", ASME Transactions, Vol. 67, p.621, 1945.

14 Sparrow, E., and Lin, S., "Heat transfer characteristics of polygonal and plate fins", In. J. Heat Mass Transfer, Vol. 7, pp. 951-953, 1964.

15 Schmidt, T.E., "La Production Calorifique des Surfaces Munies D'ailettes", Annexe Du Bulletin De L'Institut International Du Froid, Annexe G-5, 1945-46.

16 Ware, H., and Hacha, T., "Heat transfer from humid air to fin and tube extended surface cooling coils", ASME Paper, no. 60-HT-17, p. 7, 1960.

17 Stoecker, W, and Jones, J., *Refrigeration and Air Conditioning*, McGraw-Hill, New York, 1982.

18 Oskarsson, S.P., K.I. Krakow, and S. Lin, "Evaporator models for operation with wet and frosted finned surfaces, part 1: Heat transfer and flow theory", ASHRAE Transactions, Vol. 96, Pt. 1, 1990.

19 Kays ,W.M., and London, A.L., Compact heat exchangers, New York: McGraw Hill Book Co., 1984.

20 Rich, D.G., "The effect of the number of tube rows on heat transfer performance of smooth plate fin-and-tube heat exchangers", ASHRAE *Transactions*, Vol.81, Part 1, 1975.

[21] McQuiston, F.C., "Finned tube heat exchangers: state of the art for the air side", ASHRAE *Transactions*, Vol.81, Part 1, 1981.

[22] Gray, D.L., and Webb, R.L., "Heat Transfer and Friction Correlations for Plate Finned-Tube Heat Exchangers Having Plain Fins", Procs. of Eigth Intl. Heat Transfer Conf., San Francisco, 1986.

[23] Eckels, P.W., and Rabas, T.J., "Dehumidification: On the correlation of wet and dry transport processes in plate finned-tube heat exchangers", Journal of Heat Transfer, Vol.109, pp.575-582, 1987.

[24] Myers, R.J., "The effect of dehumidification on the air-side heat transfer coefficient for a finned-tube coil", M.S. Thesis, University of Minnesota, Minneapolis, 1967.

[25] Idem, S.A., Jacobi, A.M., and Goldschmidt, V.W., "Heat transfer characterization of a finned-tube heat exchanger (with and without condensation)", Transactions of the ASME, Vol.112, Feb 1990.

[26] Hu, X., Zhang, L., and Jacobi, A.M., "Surface irregularity effects of droplets and retained condensate on local heat transfer to finned tubes in cross-flow", ASHRAE *Transactions*, V.100, Pt.1, 1994.

[27] Dittus, F.W., and L.M.K. Boelter, University of California Publications on Engineering, Vol.2, p.443, Berkeley, 1930.

[28] Wattelet, J.P., "Heat Transfer Flow Regimes of Refrigerants in a Horizontal-Tube Evaporator", Ph.D. dissertation, University of Illinois at Urbana-Chamapaign, 1994.

[29] Bivens, D.B., and A. Yokozeki, “Heat Transfer of Refrigerant Mixtures”, Proceedings International Refrigeration Conference at Purdue , Purdue University, July 1994.

[30] Gropp, U., and Schlunder, E.U., "The influence of liquid side mass transfer on heat transfer and selectivity during surface and nucleate boiling of liquid mixtures in a falling film", Chem. Eng. Process., Vol.20 (2), pp.103-114, 1986.

[31] Paliwoda, A., "Generalized method of pressure drop calculation across pipe components containing two-phase flow of refrigerants", Rev. Int. Froid, Vol 15, No 2, 1992.

[32] Lockhart, R.W., and R.C., Martinelli, "Proposed Correlation of Data for Isothermal Two-Phase, Two-component Flow in Pipes", Chemical Engineering Progress, Vol.45, pp.39-48, 1949.

[33] Soliman, M., J.R., Schuster, and P.J., Berenson, "A General Transfer Correlation for Annular Flow Consideration", Journal of Heat Transfer, Vol.90, pp.267-276, 1968.

[34] Butterworth, D., "A comparison of some void fraction relationships for co-current gas-liquid flow", Int. J. of Multiphase Flow, Vol.1, 1975.

[35] Gallagher, J., McLinden, M., Morrison, G., and Huber, M., "NIST thermodynamic properties of refrigerants and refrigerant mixtures - Version 4.0", National Institute of Standards and Technology, 1993.

[36] Ragazzi, F., and T.R., Nygaard, "Refrigerant Properties for Pure and Mixed Refrigerants: An Interpolation Subroutine Package", ACRC Technical Memorandum #16, University of Illinois at Urbana-Champaign, 1995.

[37] Mullen, C.E., "Room Air Conditioner System Modeling", M.S. Thesis, University of Illinois at Urbana-Champaign, 1994.

[38] Nygaard, T.R., forthcoming M.S. Thesis, University of Illinois at Urbana-Champaign, 1995.

[39] Ragazzi, F., "Thermodynamic Optimization of Evaporators with Zeotropic Refrigerant Mixtures", Ph.D. dissertation, University of Illinois at Urbana-Chamapaign, 1995.

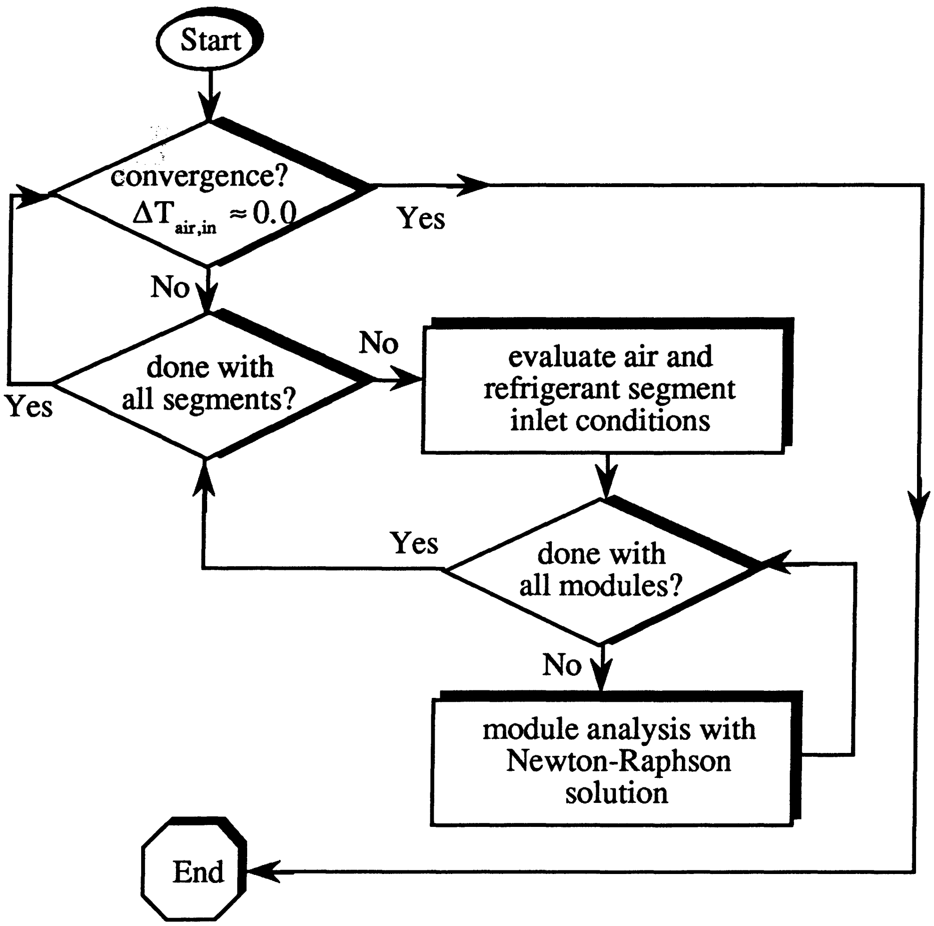

Figure 4.1 Solution Scheme of the Evaporator Model

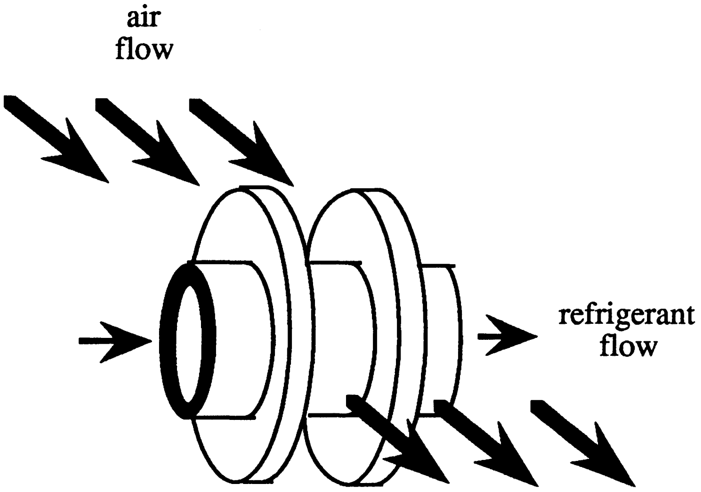

Figure 4.2 Typical Evaporator Module with Equivalent Circular Fins

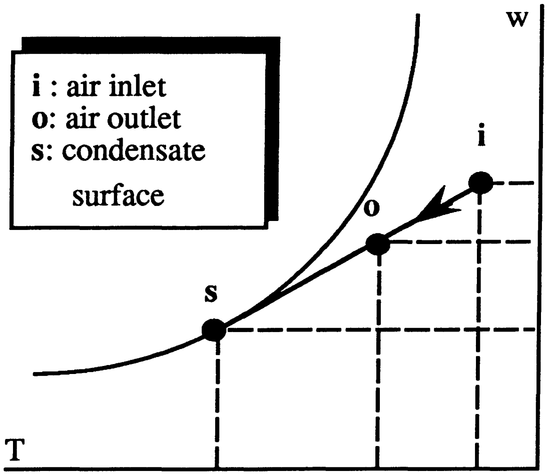

Figure 4.3 Linearized Air De-humidification Path on the Psychometric Chart

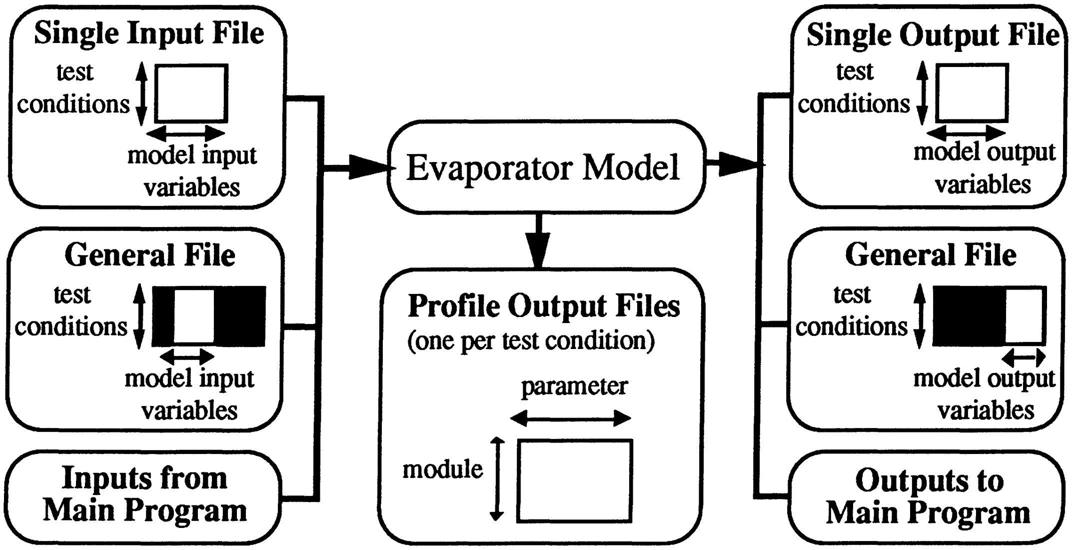

Figure 4.4 Evaporator Model Interfacing

CHAPTER 5
MODEL VALIDATION

An experimental study of an air-conditioning system operating with pure and mixed refrigerants was undertaken to validate the evaporator model developed as part of this research project. The most pertinent details of the experimental facility are presented in the first section of this chapter, along with a description of the data acquisition procedure and the mechanisms used to control the system operating conditions.

The second section summarizes the experimental results obtained with two different evaporator coils, using HCFC-22 and a zeotropic blend of HFC-32/HFC-125/HFC-134a (23/25/52%). Finally, a comparison of experimental and theoretical results, obtained with different heat and mass transfer models, is presented in the third section with an emphasis on the independence of the model from experimental data.

5.1 Experimental Test Facility

The purpose of the experimental setup was to obtain heat transfer and pressure drop data with various evaporator designs for a wide range of controlled air and refrigerant operating conditions. It included instrumented air and refrigerant loops, shown in Figure 5.1, and a removable evaporator test section.

An overview of the experimental test facility is presented in this section, with a brief description of its major components, the evaporator coils tested, the computerized data acquisition system, and the control capabilities. A more detailed description of the electrical components, the built-in control and safety electrical circuitries, and the calibration and installation of the measurement devices, may be found in the account of a related study by Nygaard [1].

5.1.1 Air Side

The air loop, aimed at adjusting the mass flowrate, temperature and humidity content of the air flowing over the evaporator to desired values, is shown in Figure 5.2.

Air flow was provided by a blower controlled through the use of a variable speed drive, which was connected to a 7.5 horsepower fan motor. The air leaving the fan was expanded into a plenum 1.0668 m high and 0.9144 m wide, with an expansion of less than 12°. Two wire screens were placed within the first 0.762 m long section of the plenum, in order to provide a uniform velocity profile of the air before it passed through a pair of flow nozzles. These were 152.4 mm (6 in.) in diameter, in combination with either a 139.7 m (5.5 in.) or a 68.275 m (2.688 in.) in diameter, depending upon the flow rate.

The air mass flow rate was determined by measuring the pressure drop across the nozzle bank with two sets of pressure taps placed upstream and downstream of the nozzles. Each set included four taps, located in the middle of each of the four sides of the plenum, to obtain an average reading. The nozzle pair with the smallest nozzle diameters was selected for low air mass flow rates, to ensure that the measured air pressure drop was of the same order of magnitude as the range of the air pressure transducer. The air mass flow rate was calculated using relations recommended by ASHRAE [2] which were incorporated in subroutine *airflow* of the data reduction program.

After passing through the nozzles, the air went through another set of wire screens, placed in the remaining 1.143 m long section of the plenum. A 0.4572 m long contraction was used to connect the plenum to a 0.508 m by 0.508 m duct section, and additional wire screens were added near the inlet of the duct to reduce the turbulence caused by the contraction. Two electric heaters were placed in the 1.2192 m long duct section. The first heater produced a controlled 0-5.78 kW load, based on feedback from a thermocouple placed at the inlet to the evaporator test section. The second heater was used to provide an optional 5.5 kW baseline load. Details related to the physical features of the heaters, the wiring diagrams, and the built-in safety switch linked to an airflow measuring device were reported by Nygaard [1].

After exiting the heater section, the air stream went through a 90° turn equipped with turning vanes. It then passed through a fixed blade mixer, to eliminate temperature gradients, and entered another 0.508 m by 0.508 m, 1.143 m long duct section. A steam injection port, connected to an immersion heater-type humidifier, was placed downstream of the mixer. A transparent window was installed in the duct in order to visually verify that steam was not condensing on the duct walls. The humidifier was controlled based on feedback from a dew point sensor located near the entrance to the evaporator test section.

The air stream then went through another 90° turn, equipped with turning vanes, before expanding into the 0.762 m high and 0.9144 m wide evaporator test section. Two wire screens were placed in the 0.508 m long portion of the test section preceding the evaporator coil in order to provide a uniform air velocity profile. This entrance region was also equipped with a grid of nine thermocouples, and an air sampler connected to a *chilled mirror* dew point sensor. The air sampler consisted of a copper tube with uniformly spaced orifices, which was placed across the middle of the duct perpendicular to the direction of air flow. The rate of air sampling was monitored and maintained within the desired range to ensure the proper functioning of the dew point sensor.

The evaporator coil was placed in a wall behind the test section. The air pressure drop across the coil was measured using average pressures obtained by placing pressure taps on all four sides of the duct both upstream and downstream of the coil. A grid of nine thermocouples was placed downstream of the coil, followed by a fixed blade air mixer. The air was sampled after the air mixer, and its humidity content was measured with a second dew point sensor. A drain was installed below the evaporator coil in order to collect and measure the condensate runoff.

The entire evaporator test section, including the evaporator entrance and exit regions, was 1.778 m long. The air stream was then contracted into a 0.3048 m diameter duct section, equipped with dampers to control the amount of fresh air mixing. Following the damper section, the air duct was contracted further into the 0.235 m diameter blower inlet.

Heat leaks between the duct and evaporator coil, and the surrounding air space, were minimized by heavily insulating the duct and the test section with 25.4 mm (1 in.) thick foamrubber sheets.

5.1.2 Refrigerant Side

The refrigerant loop, shown in Figure 5.3, was adapted from a 3.516 kW (3 tons, or 36,000 Btu/hr) refrigeration system.

Two major modifications were made to the original system. The air-cooled condenser was replaced with a water-cooled one, in response to spatial constraints and the need to accurate control the condenser pressure. In addition, an oil separator was installed at the exit to the compressor to avoid the presence of oil in the evaporator. This eliminated the need to measure the circulating oil concentration, and to include its effects on refrigerant thermodynamic properties in the data analysis. The original mineral oil in the system was replaced with a polyolester oil due to compatibility problems associated with the zeotropic refrigerant mixture.

As the oil-free refrigerant exited the evaporator, it flowed through an accumulator and a filter before entering the compressor. A ball valve was added between the evaporator and the accumulator. This valve, along with an existing solenoid valve, was used to isolate the high and low pressure sides for leak-testing purposes. Once all the refrigerant was pumped to the high pressure side with the ball valve closed, the compressor prevented the refrigerant from flowing back to the low pressure side. At the compressor exit, the oil was removed by an oil separator, so that an oil-free sample of the vapor refrigerant circulated through the evaporator.

The refrigerant then passed through a water-cooled condenser, a receiver, and a second water-cooled heat exchanger. This exchanger allowed for the adjustment of the refrigerant sub-cooling, and ensured the flow of single phase refrigerant into the mass flow meter. A second sampling port was located prior to the flow meter, so that liquid refrigerant samples could be obtained.

Finally, a manual expansion device was used to adjust the refrigerant evaporator pressure and mass flowrate, for a given compressor speed and condenser pressure. Copper tubing 22.225 mm (7/8 in.), 15.875 mm (5/8 in.), and 9.525 mm (3/8 in.) in diameter was used for the suction, discharge, and liquid lines respectively, and all connections were made using high temperature silver solder.

The loop was fully instrumented to collect refrigerant temperature, pressure and mass flowrate data, as indicated in Figure 5.3. Foamrubber was used to insulate the refrigerant lines 0.3048 m (1 ft.) downstream and upstream of each temperature measurement in order to reduce errors in the measurement of refrigerant temperatures. The space surrounding the evaporator return bends was insulated with a fiberglass mat.

Due to the presence of additional components and measuring devices, the total system charge was different from that of the original air-conditioning system. The correct amount of charge was estimated by adding charge, with the system running, until the absence of bubbles at the sub-cooler outlet was observed. A typical refrigerant charge ranged between 4.536 and 6.804 kg (10 and 15 lb).

5.1.3 Evaporator Coils

Data for the model validation were collected with two air-cooled direct expansion evaporator coils, A and B. The first coil (A) was designed for refrigerant HCFC-22, and operating conditions typical of a 10.548 kW (3 ton, 36,000 Btu/hr) air-conditioning system. The second coil (B), was significantly different from the first one in terms of the refrigerant circuitry relative to the air stream. It was tested in order to further validate the generality of the model.

Both coils were placed in the test section normal to the horizontal air stream. Their main features are summarized in Table 5.1.

Table 5.1 Specifications of Evaporator Coils A and B

	Coil A	**Coil B**
Tube Stock	15.875 mm O.D. x 0.4572 mm (3/8 in. O.D. x 0.018 in.)	15.875 mm O.D. x 0.4572 mm (3/8 in. O.D. x 0.018 in.)
Tube Pattern	staggered 38.1 mm x 32.99 mm (1.50 in. x 1.299 in.)	staggered 38.1 mm x 32.99 mm (1.50 in. x 1.299 in.)
Finned Height †	0.6096 m (24 in.)	0.3048 m (12 in.)
Finned Length	0.6096 m (24 in.)	0.6096 m (24 in.)
Fin Thickness x Material	0.1524 mm (0.006 in.) Al	0.1524 mm (0.006 in.) Al
Fin Spacing	228.6 fins/mm (9 fins/in.)	228.6 fins/mm (9 fins/in.)
Fin Configuration	Continuous, Waffle/Ripple	Continuous, Waffle/Ripple
Number of Rows †	4	8
Feeds/Passes	2/32	2/32

† Difference between coils A and B

The entering refrigerant stream was divided into two separate streams, which then followed identical circuitries before entering the exit manifold. The circuitries of coils A and B are described in Figures 5.4a-b.

5.1.4 Data Acquisition

All data were collected using data acquisition boards which converted the 0-5 volt analog signals into digital output and sent it to a personal computer. A software package was used to sample, time-average, and record the raw data over a period of sixty seconds after the system had reached steady-state operating conditions. All calibration and data analysis calculations were done by software written in FORTRAN code [39].

Subroutine *timeavg* calculated an average for each of the measured variables, and used the standard deviation of the data as an indicator of whether or not steady-state had been reached. The calibration constants were included in a separate file, and could thus be easily changed after re-calibration of a measuring device. All calibration calculations were performed by subroutine *calibrate*. The measurements used in the data reduction are summarized in Table 5.2.

Table 5.2 Experimental Measurements

Measured Variable	**Locations**	**Device**	**Uncertainty**
Air Temperature	• Evaporator. inlet • Evaporator. outlet • Nozzle station	Ungrounded T-type Cu/Ct thermocouple	+/- 0.28 °C (+/- 0.5 °F)
Air Pressure	• Evaporator outlet/ atm • Evaporator inlet/ outlet • Nozzle outlet/ atm • Nozzle inlet/ outlet	Differential transducer	+/-1.0% full scale
Air Dew Point Temperature	• Evaporator inlet • Evaporator outlet	*Chilled mirror* dew point sensor	+/- 0.28 °C (+/- 0.5 °F)
Refrigerant Temperature	• Expansion valve inlet • Evaporator inlet • Evaporator outlet	T-type thermocouple (in-flow)	+/- 0.28 °C (+/- 0.5 °F)

Measured Variable	Locations	Device	Uncertainty
	• Expansion valve inlet • Evaporator outlet • Evaporator return bends • Oil separator outlet • Compressor inlet • Sub-cooler outlet	T-type thermocouple (surface)	+/- 0.56 °C (+/- 1.0 °F)
Refrigerant Pressure	• Expansion valve inlet • Compressor inlet • Condenser inlet	Absolute transducer	+/-1.0% full scale
	• Evaporator inlet/outlet • Condenser inlet/ sub-cooler outlet	Differential transducer	+/-1.0% full scale
Refrigerant Mass Flowrate	• Sub-cooler outlet	*Coriolis* flow meter	+/-0.2% full scale
Compressor Power Input	• Compressor inverter	*Watt* transducer	

Two different approaches were followed for the calibration of air and refrigerant thermocouples. With the first one, a representative channel from each panel was calibrated using an isothermal water-glycol bath with temperature data measured in °F. The slope of all linear regressions associated with a given panel was found to be nearly the same.

This approach was used with success, but proved tedious due to frequent changes in the offsets of each channel. In order to avoid the periodic re-calibration of each channel, a constant ice-bath reference temperature was used instead. Four thermocouples, connected to a representative channel from each panel, were immersed in an ice-bath. This and other thermocouple calibration techniques are summarized in Figures 5.5a-c.

5.1.5 Control of Operating Conditions

An effort was made to control the air and refrigerant operating conditions. This allowed for the direct comparison of experimental results obtained with pure and mixed refrigerants under similar test conditions. The main features of the test facility, related to the control of the conditions of both fluid streams, are summarized in Table 5.3.

Table 5.3 Control of Air and Refrigerant Conditions

Variable	**Control Mechanism**	**Accuracy**
Air Mass Flowrate	• Blower with variable speed control	+/- 1.26e-2 kg/s (+/- 100 lb/hr) (+/- 20 cfm)
Air Temperature (evaporator inlet)	• On/off baseline electric heater • SCR driven electric heater with PID control	+/- 0.56 °C (+/- 1.0 °F)
Air Relative Humidity (evaporator inlet)	• Immersion heater-type humidifier with PID control	+/- 1 %
Refrigerant Sub-cooling (sub-cooler outlet)	• Sub-cooler water mass flowrate	
Refrigerant Pressure (condenser outlet)	• Condenser water flow rate adjusted by pressure regulator	+/- 3.45 kPa (+/- 0.5 psi)
Refrigerant Pressure (evaporator inlet)	• Hermetic compressor with variable speed control • Manual expansion device	+/- 3.45 kPa (+/- 0.5 psi)
Refrigerant Mass Flowrate	• Hermetic compressor with variable speed control • Manual expansion device	+/- 1.26e-3 kg/s (+/- 10 lb/hr)

Nine independent temperature measurements at the evaporator inlet were used to check for air stratification. In general, all nine temperatures were within 0.28 °C (0.5 °F) of the mean inlet temperature. The thermocouple in the middle of this grid was used to provide feedback for the control of the second electric heater.

The outputs of both dew point sensors were found to agree within 0.28 °C (0.5 °F) in the absence of airflow. The output from the inlet sensor provided the feedback necessary for the control of the humidifier. Using dew point, as opposed to relative humidity, resulted in increased control accuracy. Whereas relative humidity is a function of two independent measurements, humidity ratio is only dependent on the dew point temperature. Thus, air humidity was controlled by choosing a pair of air dry bulb temperatures and humidity ratios, the latter set by adjusting the air dew point temperature, corresponding to the desired relative humidity level.

On the refrigerant side, the water mass flowrate of the sub-cooler was manually adjusted to obtain an approximate level of sub-cooling. The condenser outlet pressure was set automatically with a mechanical pressure regulator, connected to the refrigerant line, which adjusted the water mass flowrate in the condenser as shown in Figure 5.6.

The refrigerant mass flowrate and evaporator inlet pressure were set by simultaneously adjusting the compressor speed and the opening of the manual expansion device for a given choice of condenser pressure.

Additional controls were added to the system for safety reasons, to avoid over-heating and over-humidifying the air stream. On the refrigerant side, the control circuitry of the original refrigeration system was modified to maintain the high and low refrigerant pressures within tolerable ranges. Absolute refrigerant pressure measurements on both sides were used as feedback for this control.

Finally, refrigerant mixtures were periodically sampled in order to ensure the correct circulating mixture composition. The loop included two sampling ports used to collect both liquid and vapor refrigerant samples. A plastic tube was connected to each sampling valve, and its other end was placed inside a container full of water. The tube was first purged of any air or impurities, and the refrigerant was sampled through it. The refrigerant loss during this bleeding procedure did not affect the composition of the remaining system charge, since the refrigerant was sampled only while the system was operating to insure the absence of fractionation at the sampling port.

Refrigerant samples were analyzed with a gas chromatograph and mixture composition was adjusted by adding the appropriate amount of the lacking pure components. Composition measurements were found to be accurate and repeatable, and good agreement was found between the composition of liquid and vapor samples as shown in Table 5.4.

Table 5.4 Typical Refrigerant Mixture Composition Measurements

Expected Composition	Measured Composition
R-32: 23% R-125: 25% R-134a: 52%	R-32: 22.5-23.5% R-125: 24.5-25.5% R-134a: 51.5-52.5%

5.2 Experimental Results

The experimental data included both evaporator and system-related measurements. Any change in one or more of the operating variables, due to start-up or otherwise, was followed by a waiting period of no less than ten minutes to ensure the steady-state operation of the system. In general, transients caused by changes in the refrigerant operating conditions lasted longer than those related to the air-side.

The repeatability of several of the data points was verified. An additional check was provided by the energy balance between the measured evaporator rates of heat transfer, based on the air and refrigerant inlet and outlet conditions respectively.

5.2.1 Experimental Data Reduction

Reduction of the experimental data included the calculation of variables related to the air and refrigerant states, as well as evaporator and system performance. The ensuing paragraphs provide an overview of the methodology used in the analysis of the data.

5.2.1.1 Air and Refrigerant State Properties

Average air temperatures at the evaporator inlet and outlet corresponded to the numerical averages of the nine independent thermocouple measurements taken upstream and downstream of the coil. One of the thermocouples on the inlet grid formed a junction elsewhere during the course of the study, and was therefore excluded from the average in most of the analysis. The inlet and outlet humidity ratios were calculated from the mechanically averaged measured dew point temperatures at both locations. Other air properties, such as enthalpy and relative humidity, were derived from previously calculated air state variables.

On the refrigerant side, enthalpies for single phase refrigerant were calculated based on the measured temperatures and pressures. The evaporator inlet quality was calculated based on the local pressure and enthalpy, with the assumption of an isenthalpic expansion valve.

$$P_{r,ei} = P_{r,eo} + \Delta P_{r,e} \tag{5.1}$$

$$x_{r,ei} = x(P_{r,ei}, h_{r,ei}) = x(P_{r,ei}, h_{r,vi}) \tag{5.2}$$

5.2.1.2 Evaporator Total Rate of Heat Transfer

The rate of heat transfer received by the refrigerant stream was calculated based on its enthalpy increase,

$$\dot{Q}_{r,e} = \dot{m}_r \cdot \left(h_{r,eo} - h_{r,ei}\right) \tag{5.3}$$

Neglecting heat leaks to the surroundings, this rate of heat transfer was the result of several mechanisms, such as cooling of the dry air flowing over the exchanger, cooling of the water vapor which was not condensed on the finned surfaces, and the isothermal change of phase of the water vapor which was condensed on the finned surfaces

An independent expression was obtained for the fluid-to-fluid rate of heat transfer within the exchanger in terms of the inlet and outlet states of the air and condensate streams, shown in Figure 5.7.

The inlet and outlet moist air streams were treated as separate streams of dry air and entrained water vapor. A fraction of the entering water vapor stream did condense on the finned surfaces, and was assumed to exit the control volume in liquid form at the dew point temperature of the entering moist air.

The enthalpy change of the moist air stream was given by,

$$\dot{Q}_{a,e} = \dot{m}_a \cdot \left(\bar{h}_{a,ei} - \bar{h}_{a,eo}\right) \tag{5.4}$$

The air mass flowrate, $\dot{m}_{a,e}$, was calculated based on experimental data measured before the steam injector, and was assumed to represent the mass flow rate of dry air since the humidity content of the air flowing through the nozzles was typically low. This assumption was required because the air enthalpies used in Equation (5.4) were defined on a per kg (per lbm) of dry air basis.

The enthalpy of the exiting condensate stream was calculated with,

$$\dot{Q}_{c,e} = \dot{m}_a \cdot \left(\omega_{a,ei} - \omega_{a,eo}\right) \cdot c_{p,w} \cdot \left(T_{c,eo} - T_{ref}\right) \tag{5.5}$$

Since the humidity ratio is defined in terms of $kg\ H_2O/kg\ dry\ air$, the first part Equation (5.5) represents the mass flowrate of condensate. Its enthalpy per unit mass is based on the same zero-enthalpy reference point used for the calculation of moist air enthalpies, saturated liquid at T_{ref} = -17.78 °C (0 °F).

The sum of $\dot{Q}_{c,e}$ and $\dot{Q}_{a,e}$, or $\dot{Q}_{a+c,e}$, was used to evaluate the accuracy of the experimental heat balance,

$$E_{Q_e} = 100 * \left| \frac{\dot{Q}_{r,e} - \dot{Q}_{a+c,e}}{\dot{Q}_{r,e}} \right| \tag{5.6}$$

5.2.1.3 Evaporator Sensible Heat Ratio

An effort was made to identify the sensible and latent loads of evaporators operating under wet conditions. The sensible load was approximated with,

$$\dot{Q}_{a_s,e} = \dot{m}_a \cdot c_{p,a} \cdot \left(\bar{T}_{a,ei} - \bar{T}_{a,eo}\right) \tag{5.7}$$

By using a specific heat value associated with dry air in Equation (5.7), the load associated with the sensible heating of the water vapor entrained in the air stream was neglected.

The latent load was calculated as the heat released by the condensing water vapor, neglecting the heat associated with its cooling down to the tube surface temperature.

$$\dot{Q}_{a_L,e} = \dot{m}_a \cdot \left(\omega_{a,ei} - \omega_{a,eo}\right) \cdot i_{fg} \tag{5.8}$$

An uncertainty analysis, based on numerical partial derivatives and the measurement uncertainties listed in Table 5.2, was performed by subroutine *uncertainty* in order to determine the relative accuracy of the air and refrigerant-based results. The results of that analysis is summarized in Table 5.5, and show the refrigerant measurements to be substantially more reliable.

Table 5.5 Uncertainties of Calculated Experimental Variables

Variable	**Absolute Uncertainty as a % of $\dot{Q}_{r,e}$**
$\dot{Q}_{r,e}$	0.10-0.14
$\dot{Q}_{a+c,e}$	4.9-10.6
$\dot{Q}_{a_S,e}$	1.8-3.2
$\dot{Q}_{a_L,e}$	4.2-10.1

In addition to higher errors due to the nature of the measuring devices, the air side calculations involved a larger number of potentially flawed calculations. This included the mathematical averaging of the stratified air outlet temperature profile, and the one-dimensional mechanical averaging of the dew point measurements. Air leaks between the air nozzle station and the evaporator test section may also have contributed to an over-estimation of air mass flowrates.

5.2.1.4 Refrigerant Superheat and Sub-Cooling

Refrigerant sub-cooling at the exit to the sub-cooler was calculated based on the pressure and temperature measurements at that location, ($P_{r,sc\,o}$, $T_{r,sc\,o}$), according to

$$\Delta T_{sc} = T_{r,sc\,o} - T_{r,bubble}(P_{r,sc\,o}) \tag{5.9}$$

where $T_{r,bubble}$ is the bubble temperature of the refrigerant mixture at the sub-cooler outlet pressure. Similarly, refrigerant superheat at the exit to the evaporator was calculated based on the pressure and temperature measurements, $(P_{r,eo}, T_{r,eo})$,

$$\Delta T_{sh} = T_{r,eo} - T_{r,dew}(P_{r,eo}) \tag{5.10}$$

where $T_{r,dew}$ is the dew temperature of the refrigerant mixture at the evaporator outlet pressure. For a pure refrigerant , such as HCFC-22, the bubble and dew temperatures simply corresponded to its saturation temperature.

5.2.1.5 Evaporator Pressure Drop

The differential pressure transducer used to measure refrigerant pressure drop was connected directly across the evaporator coil, to exclude additional refrigerant pressure drops associated with the inlet and outlet manifolds and distributor tubes.

On the air side, pressure drop effects related to the sudden contraction and enlargements upstream and downstream of the evaporator coil were estimated and subtracted from the total experimentally measured air pressure drop. These calculations were performed by subroutine *dPahxexp_calc*, as suggested by Stoecker and Jones [3].

5.2.1.6 System Performance

The power input into the variable speed drive required to run the compressor was measured with a watt-transducer, and used to approximate the net compressor work, $\dot{W}_k$. The latter was needed to calculate the system *coefficient of performance*,

$$COP = \frac{\dot{Q}_{r,e}}{\dot{W}_k} \tag{5.11}$$

A more detailed analysis of system performance was presented by Nygaard [1], including inverter and compressor motor efficiencies. The refrigerant-based rate of heat transfer was chosen in Equation (5.11) because of its lower experimental uncertainty.

5.2.2 Experimental Data

Experimental test matrices were completed with HCFC-22 for coil A, and with a zeotropic blend of HFC-32/HFC-125/HFC-134a (23/25/52%) for coils A and B. Data were collected under controlled wet and dry conditions typical of residential air-conditioning applications, as shown in Tables 5.6a-c.

Table 5.6a Experimental Test Matrix for HCFC-22 with Coil A

		$T_{a,ei}$	26.67 °C (80 °F)	32.22 °C (90 °F)
		$\phi_{a,ei}$	.50	dry
$P_{r,ei}$	$\dot{m}_{a,e}$	$\dot{m}_{r,e}$		
689 kPa (100 psi)	0.1261 kg/s (1000 lbm/hr)	0.0504 kg/s (400 lbm/hr)	•	•
		0.06306 kg/s (500 lbm/hr)	•	•
	0.16394 kg/s (1300 lbm/hr)	0.0504 kg/s (400 lbm/hr)	•	•
		0.06306 kg/s (500 lbm/hr)	•	•
737.2 kPa (107 psi)	0.1261 kg/s (1000 lbm/hr)	0.0504 kg/s (400 lbm/hr)	o	•
		0.06306 kg/s (500 lbm/hr)	o	o
	0.16394 kg/s (1300 lbm/hr)	0.0504 kg/s (400 lbm/hr)	•	•
		0.06306 kg/s (500 lbm/hr)	o	•

• single phase refrigerant at evaporator exit
o two-phase refrigerant at evaporator exit

Table 5.6b Experimental Test Matrix for HFC-32/HFC-125/HFC-134a (23/25/52%) with coil A

		$T_{a,ei}$	26.67 °C (80 °F)			32.22 °C (90 °F)		
		$\phi_{a,ei}$	dry	.50	.65	dry	.50	.65
$P_{r,ei}$	$\dot{m}_{a,e}$	$\dot{m}_{r,e}$						
689 kPa (100 psi)	0.1261 kg/s (1000 lbm/hr)	0.0504 kg/s (400 lbm/hr)	x	●	●	●	●	●
		0.06306 kg/s (500 lbm/hr)	o	x	●	x	●	●
	0.16394 kg/s (1300 lbm/hr)	0.0504 kg/s (400 lbm/hr)	●	●	●	●	●	●
		0.06306 kg/s (500 lbm/hr)		●	●	●	●	●
757.9 kPa (110 psi)	0.1261 kg/s (1000 lbm/hr)	0.0504 kg/s (400 lbm/hr)	o	o	●	●	●	●
		0.06306 kg/s (500 lbm/hr)	o	o	x	o	●	●
	0.16394 kg/s (1300 lbm/hr)	0.0504 kg/s (400 lbm/hr)	x	o	●	●	●	●
		0.06306 kg/s (500 lbm/hr)	o		●	x	●	●

● single phase refrigerant at evaporator exit

o two-phase refrigerant at evaporator exit

x evaporator superheat < 1.39 °C (2.5 °F)

Table 5.6c Experimental Test Matrix for HFC-32/HFC-125/HFC-134a (23/25/52%) with coil B

		$T_{a,ei}$	26.67 °C (80 °F)			32.22 °C (90 °F)		
		$\phi_{a,ei}$	dry	.50	.65	dry	.50	.65
$P_{r,ei}$	$\dot{m}_{a,e}$	$\dot{m}_{r,e}$						
689 kPa (100 psi)	0.1261 kg/s (1000 lbm/hr)	0.0504 kg/s (400 lbm/hr)	o	●	●	●	●	
		0.06306 kg/s (500 lbm/hr)	o	●		●	●	
	0.16394 kg/s (1300 lbm/hr)	0.0504 kg/s (400 lbm/hr)	●	●		●	●	

		0.06306 kg/s (500 lbm/hr)	•	•		•	•	
757.9 kPa (110 psi)	0.1261 kg/s (1000 lbm/hr)	0.0504 kg/s (400 lbm/hr)	o	o		•	•	
		0.06306 kg/s (500 lbm/hr)	o	o		o	•	•
	0.16394 kg/s (1300 lbm/hr)	0.0504 kg/s (400 lbm/hr)	o	•		•	•	
		0.06306 kg/s (500 lbm/hr)	o	•		•	•	

• single phase refrigerant at evaporator exit
o two-phase refrigerant at evaporator exit (predicted by the model)

The validity of experimental measurements was checked by comparing the rates of heat transfer based on both air and refrigerant measurements. Data points with two-phase refrigerant conditions at the exit to the evaporator were excluded from that analysis, since the refrigerant enthalpy at the evaporator outlet could not be experimentally measured. In addition, data points with low superheat levels were excluded due to the possibility of entrained liquid droplets leaving the evaporator. Corr et al. [4] observed this phenomenon in their testing of zeotropic mixtures, and similarly excluded low superheat points from their analysis. The precision of the refrigerant temperature measurement was taken into account in the selection of the cut-off superheat value.

Figures 5.8a-c show the energy balances corresponding to the pure and mixed refrigerant data sets obtained with coils A and B.

5.3 Model Agreement with Experimental Data

The evaporator model produced an output equivalent to every experimental measurement, in addition to several other outputs related to local heat transfer and pressure drop performance. Some of these theoretical results are presented in this section, and compared to their experimental counterparts. These include sensible and latent rates of heat transfer, air and refrigerant pressure drops, refrigerant outlet conditions and refrigerant temperature profiles. All reported percentage errors are based on the experimental data.

$$x_{i,\%\,error} = 100 * \frac{\left| x_{i,model} - x_{i,exp.} \right|}{x_{i,exp.}} \tag{5.12}$$

Significant differences were observed among the predictions of the various heat and mass transfer models, particularly those related to the latent load. Simulation results of the *discretized differential equations,* the *composite wall thermal resistance,* and the *equivalent wet effectiveness* models are presented in this section. A Lewis number equal to unity was assumed in all models.

Taking into account the symmetry of the refrigerant circuitry, and the uniformity of the air velocity profile, the evaporator model was used to simulate only one half of the evaporator coil. Identical heat transfer performance was assumed for both halves of the coil, and the modeling outputs were multiplied by a factor of two as necessary for a direct comparison with experimental data. Air and refrigerant pressure drops were assumed equal in each half of the coil.

5.3.1 Discretized Differential Equations Model

5.3.1.1 Evaporator Rates of Heat Transfer

Based on the experimental uncertainty analysis, refrigerant-based rates of heat transfer were used in the comparison of theoretical and experimental results. Figures 5.9a-c show the prediction of total evaporator capacity for pure and mixed refrigerants. Nearly all heat transfer predictions were within +/-3% of the experimental results. The agreement between the model and the experiment is remarkable given that theoretical correlations were used to model both the air and refrigerant heat transfer coefficients.

Theoretical and experimental latent rates of heat transfer for the mixed refrigerant are plotted in Figures 5.10a-b, with a majority of the model predictions within +/-15% of the experimental data. The predictions of air outlet humidity ratios and temperatures for the same mixed refrigerant data sets are shown in Figures 5.11a-b and 5.12a-b.

Errors associated with some of the dry data points were due to the model prematurely predictiong condensation. The criteria used to identify a wet exchanger module was based on a comparison of the tube surface and the entering air dew point temperatures, and only failed when the air dew point temperature approached that of the surface. Possible explanations may be related to the slightly superheated state of the water vapor in the entering air stream, as well as the neglect of condensate thermal resistance in the model.

Since different sets of simultaneous equations are solved for dry and wet exchanger modules, identified with the criteria just described, an error associated with a single exchanger module may propagate to the rest of the evaporator. The wrong decision regarding a tube pass in a given exchanger row would result in the wrong air inlet conditions for the subsequent tube passes. Figure 5.13 shows the improvement in the air outlet temperature prediction when forcing the model to perform a dry analysis on the same experimentally dry data points plotted in Figure 5.12a.

5.3.1.2 Evaporator Refrigerant Pressure Drop

Refrigerant pressure drop results with HCFC-22 and HFC-32/HFC-125/HFC-134a (23/25/52%) are compared in Figures 5.14a-c. Errors in the prediction of refrigerant pressure drop were mostly within 20% of the experimental data.

A theoretical study was conducted in order to determine the influence of refrigerant pressure drop on the refrigerant temperature profiles. Its results are summarized in Figure 5.15.

Theoretical results include pressure drop effects due to friction in tube passes and return bends, momentum changes, and elevation changes, as indicated in Figure 5.16. Friction was the main mechanism responsible for refrigerant pressure drop for all operating conditions, and its effect became more dominant with an increasing refrigerant mass flowrate.

5.3.1.3 Evaporator Air Pressure Drop

In contrast to all of the results presented above, experimental data collected with coil A was used to obtain empirical coefficients with the goal of improving the air pressure drop predictions of the model. The data set used to obtain the empirical coefficients covered a wide range of air Reynolds numbers, to ensure the validity of the correlation in the simulation of drastically different coil designs.

Air pressure drop results calculated for the mixed refrigerant and coil A are shown in Figure 5.17, with errors in the prediction of the air pressure drop mostly within 10% of the experimental data. The pressure drop calculation assumes the coil to be either completely dry or wet. This caused the model to over predict the pressure drop by as much as 20% when a few of the evaporator tubes, and therefore the entire coil, were incorrectly identified as wet.

Theoretical results included pressure drop effects due to friction of the finned surfaces, friction of the bare tubes, and momentum effects due to density changes associated with the change in air conditions across the coil. Un-modified correlations from the literature were used for all calculations, as described in subroutine *dPair_calc* with the exception of the fin friction coefficient. The latter was determined empirically for the wavy fins of coils A and B.

This choice was made for two reasons. First of all, fin friction accounts for most of the total air pressure drop, as indicated in Figure 5.18. In addition, complete information was not available on the exact nature and physical dimensions of the evaporator fins.

Whereas condensate formation effects were excluded from the calculations of air-side heat transfer coefficients, they were accounted for in those related to air pressure drop. Data from coil manufacturers [5] suggests that condensate formation may be responsible for air pressure drop increases in the order of 20%. This effect was accounted for in the analysis of wet data points with the choice of a constant enhancement factor, as described in subroutine *dPair_calc*.

5.3.1.4 Evaporator Superheat

Refrigerant superheat results for the mixed refrigerant data sets are shown in Figures 5.19a-b, with a majority of the simulation predictions within +/-3 °C (5.4 °F). of the experimental data.

Accuracy in the prediction of evaporator superheat was important in this study for two reasons. First of all, the irreversibility function used in the evaluation of exchanger performance was a strong function of the refrigerant outlet conditions. In addition, the implementation of the evaporator model in a full system model required a reliable prediction of evaporator superheat in order to avoid convergence problems. For most of the system analysis, the model was run at a fixed level of evaporator superheat, making this parameter a variable in the system solution.

5.3.1.5 Evaporator Refrigerant Temperature Profiles

Due to the importance of refrigerant temperature glide in this study, sixteen evaporator return bends were instrumented with surface thermocouples in order to validate the model predictions. Experimental and theoretical results were compared for multiple test conditions, some of which are shown in Figures 5.20a-f. For low refrigerant and tube wall resistances to heat transfer, the values of the return bend surface temperatures may be assumed to closely approach those of the refrigerant stream. Surface experimental measurements are referred to as experimental refrigerant temperatures in Figures 5.20a-f for simplicity.

In general, the agreement between the measured and calculated temperature profiles was quite encouraging, with local errors within the uncertainty of the measurement (1.8 °F or 1.0 °C). The absolute uncertainty of the return bend thermocouples was larger than that of other thermocouples for several reasons. First of all, only a representative channel from each panel was calibrated individually on a regular basis. Thus, errors may have been caused by fluctuations in the offset of each channel over time. The second source of error was due to the nature of the measurement itself, since surface thermocouples were used to instrument the return bends in order to avoid disturbing the refrigerant flow. Finally, axial conduction, along with heat leaks to the surrounding air space, may have introduced additional errors.

Regardless of their limitations in terms of absolute accuracy, the glide measurements confirmed the modeling assumption of a fairly constant specific heat in the two-phase region for zeotropes. It also served to locate the refrigerant phase transitions along the evaporator, which in most cases compared favorably with the model. Finally, the data eliminated any concerns about the elimination of the two-phase temperature glide due to refrigerant pressure drop effects. Both experimental and theoretical results showed a consistent positive slope, albeit much lower than that of the superheated refrigerant.

5.3.2 Thermal Resistance Model

The *thermal resistance model*, introduced in Chapter 4, was implemented in the evaporator model, and its results compared to those of the *discretized differential equations model*. The total rate of heat transfer was predicted with reasonable accuracy, as shown in Figures 5.21a-b.

Due to the inherent assumption of a linearized air path, however, the air outlet humidity ratio was consistently over predicted, resulting in significant errors in the latent load prediction. The air outlet humidity ratios and latent loads obtained with both the *discretized differential equations* and the *thermal resistance model* s, are compared in Figures 5.22a-b and 5.23a-b respectively.

The consistent bias between the two models may be explained with the help of Figure 5.24. Instead of lying on the imaginary line connecting the air inlet state and the average condensate saturated state, as assumed by the *thermal resistance model*, the actual air outlet state corresponds to a slightly higher humidity ratio due to the curvature of the air de-humidification path. Even though the air outlet enthalpy was predicted with sufficient accuracy, that was not the case for the air outlet state.

5.3.3 Equivalent Effectiveness Model

The *equivalent wet effectiveness model*, whose results are summarized in Figures 5.25 through 5.27, also assumes a linearized path. However, the average condensate saturation temperature is not a variable in the solution as in the *thermal resistance model*., and the slope of the air path must be evaluated based on the inlet condensate saturation temperature.

Even though the implementation of this and the *thermal resistance* model did not yield acceptable predictions of the latent rate of heat transfer, it did provide a number of helpful insights. The need to switch from one model to the next led to a restructuring of the evaporator simulation program which, along with its discretized nature, facilitated the testing of other combined heat and mass transfer models in the future.

In addition, the excellent agreement between the predicted rates of heat transfer for dry conditions with all three models was evidence of their correct implementation. This was further reinforced by the experimental validation, which served as an independent reference against which all three models could be measured.

The latent load calculations of both the *thermal resistance* and the *effectiveness* models were unsatisfactory. However, their ability to predict the total rate of heat transfer under both dry and wet operating conditions with reasonable accuracy, combined with the increased speed of their solution schemes, was an interesting observation.

The *effectiveness* model, developed as part of this study, was the fastest and most stable of all three methods. In order to further test its validity, its results associated with three evaporator coils of varying geometry were compared to those of the *discretized differential equations* model. The three coils considered had four, six and twelve rows, thirty-six tube passes and a cross-counterflow refrigerant circuitry. Total rates of heat transfer were calculated for a single operating condition (T_{ai} = 26 °C or 80 °F, and RH_{ai} = 50%), and the results of the *effectiveness* model were found to be within 10% of those of the *discretized differential equations* model for all coils.

5.4 Summary

An experimental facility was constructed as part of this study to collect the data required for the validation of the evaporator simulation program. Two different evaporator coils were tested with HCFC-22 and a zeotropic mixture of HFC-32/HFC-125/HFC-134a (23/25/52%). The first part of this chapter summarizes the main features of the facility, the coils tested, the data reduction methodology, and the data itself.

Three different combined heat and mass transfer models were implemented in the simulation. The *discretized differential equations* model was found to be the most accurate in its latent load predictions, as corroborated by the experimental data. This and other model predictions were compared to their experimental counterparts.

Theoretical results of the other two models, the *thermal resistance* and the *effectiveness,* were compared to those of the *discretized differential equations* model. While all three models were in perfect agreement as far as dry rates of heat transfer, only the *discretized differential equations* model was found to provide reliable latent load predictions.

5.5 References

[1] Nygaard, T.R., forthcoming M.S. Thesis, University of Illinois at Urbana-Champaign, 1995.

[2] "Standard Methods for Laboratory Airflow Measurement", ASHRAE Standard, ANSI/ ASHRAE 41.2-1987 (RA 92).

[3] Stoecker, W.F., and Jones, J.W., *Refrigeration and Air Conditioning*, Chapter 6, McGraw-Hill, New York, 1982.

[4] Corr, S. et al., "Trials with zeotropic refrigerants as replacements for R-22 in an instrumented glycol / water chiller", Intl. Refrigeration Conference at Purdue, 1994.

[5] Colmac Coil. Manufacturing Inc., "Type DX • 5/8 inch Direct Expansion Coils", Bulletin 5060, p. 7, 1993.

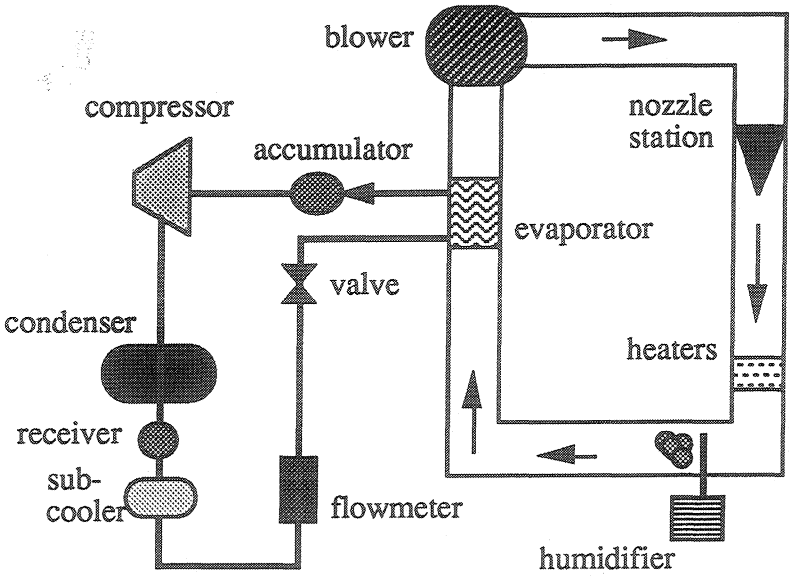

Figure 5.1 Schematic of the Experimental Test Facility

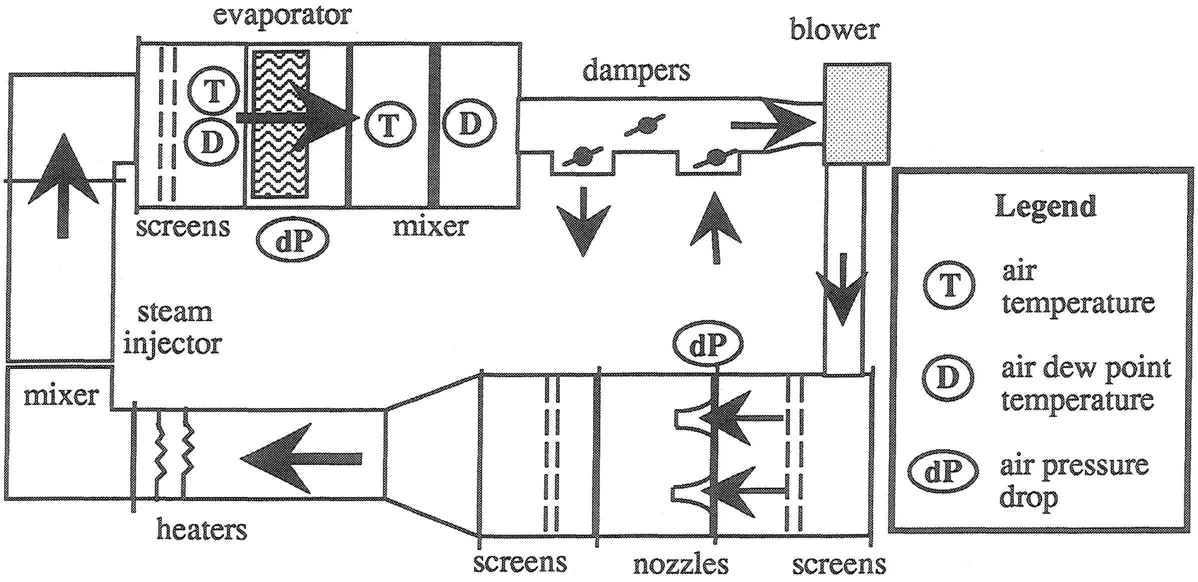

Figure 5.2 Top View of the Air Loop (scale 1:20)

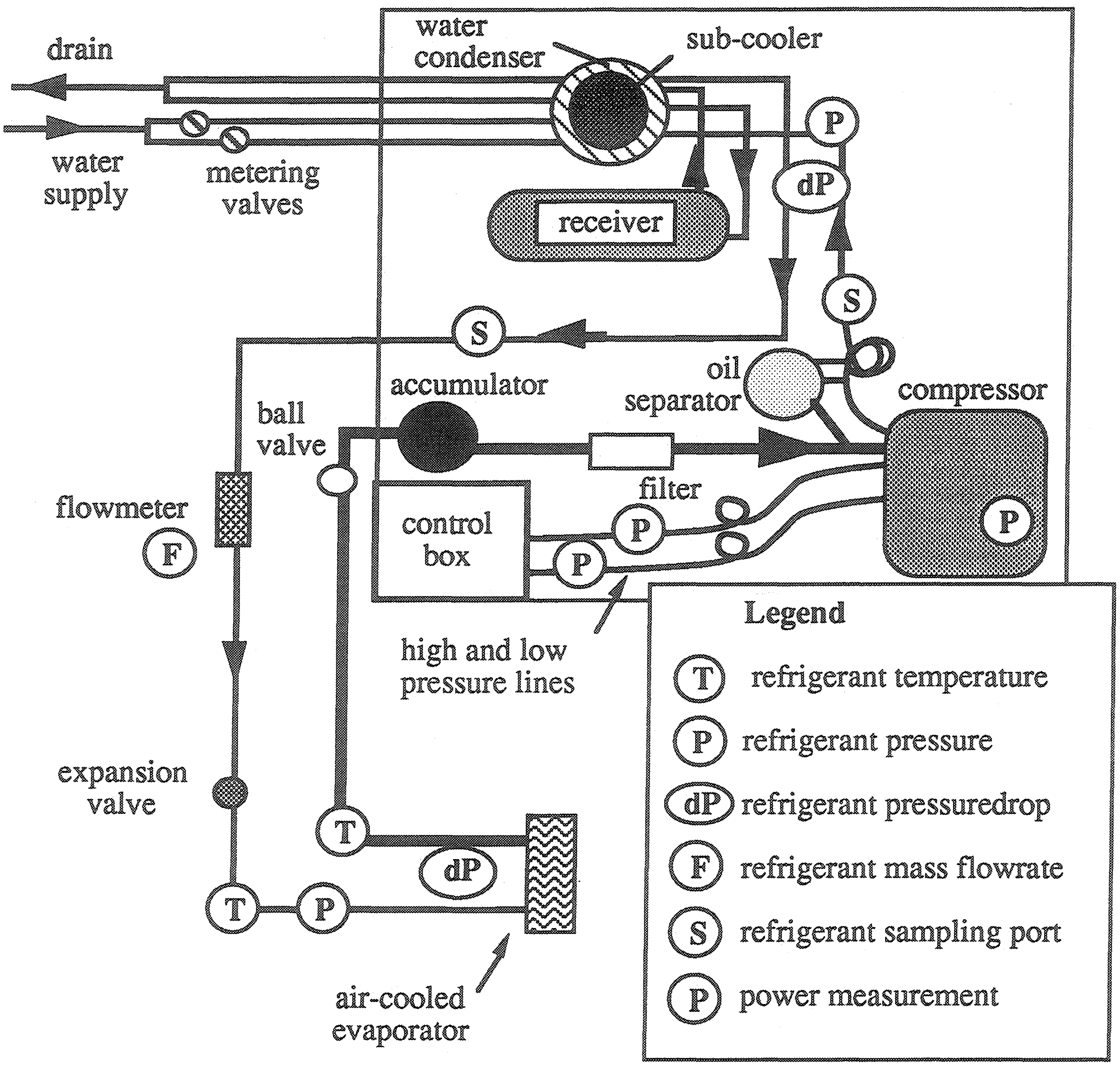

Figure 5.3 Schematic of the Refrigerant Loop

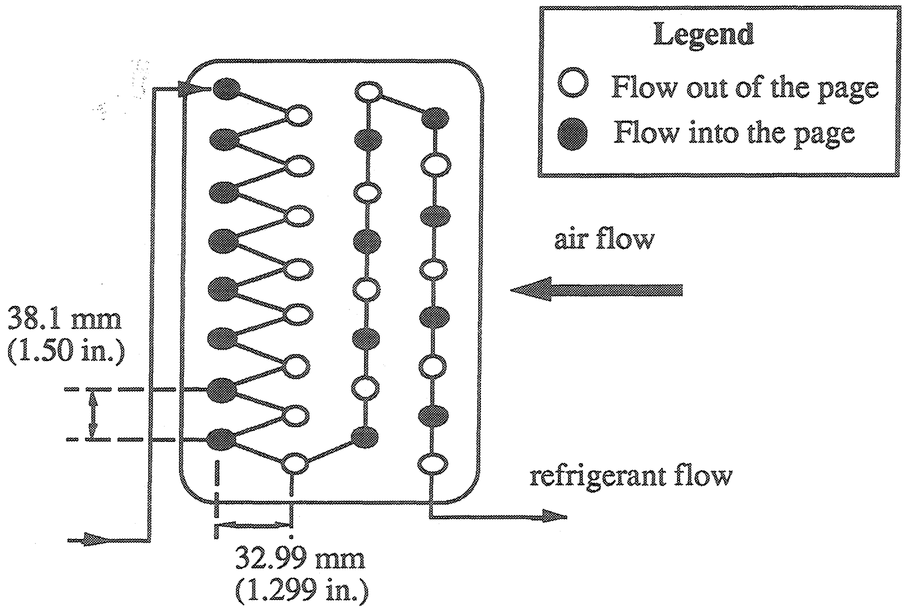

Figure 5.4a Refrigerant Circuitry for One Circuit of Evaporator Coil A

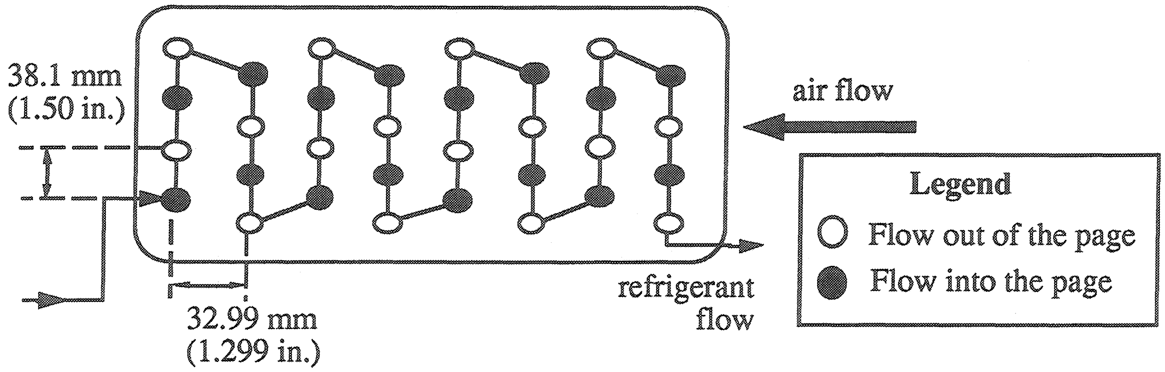

Figure 5.4b Refrigerant Circuitry for One Circuit of Evaporator Coil B

Legend

‖ Junction of dissimilar metals
A metal A (e.g. steel)
B metal B (e.g. copper)
C metal C (e.g. constantin)

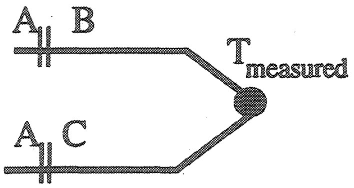

Figure 5.5a
Simple Junction

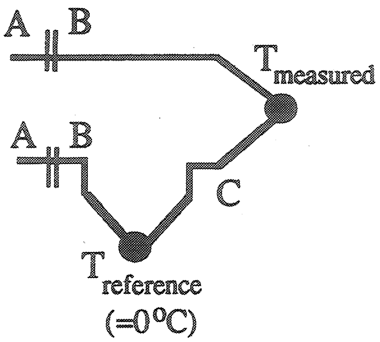

Figure 5.5b Physical
Comparison to Referenc Junction

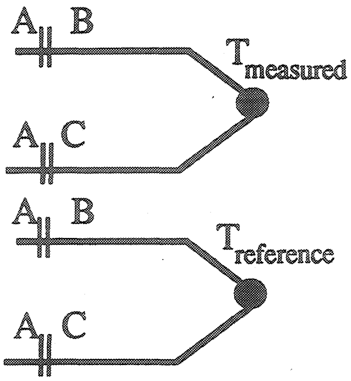

Figure 5.5c Mathematical
Comparison to Reference Junction

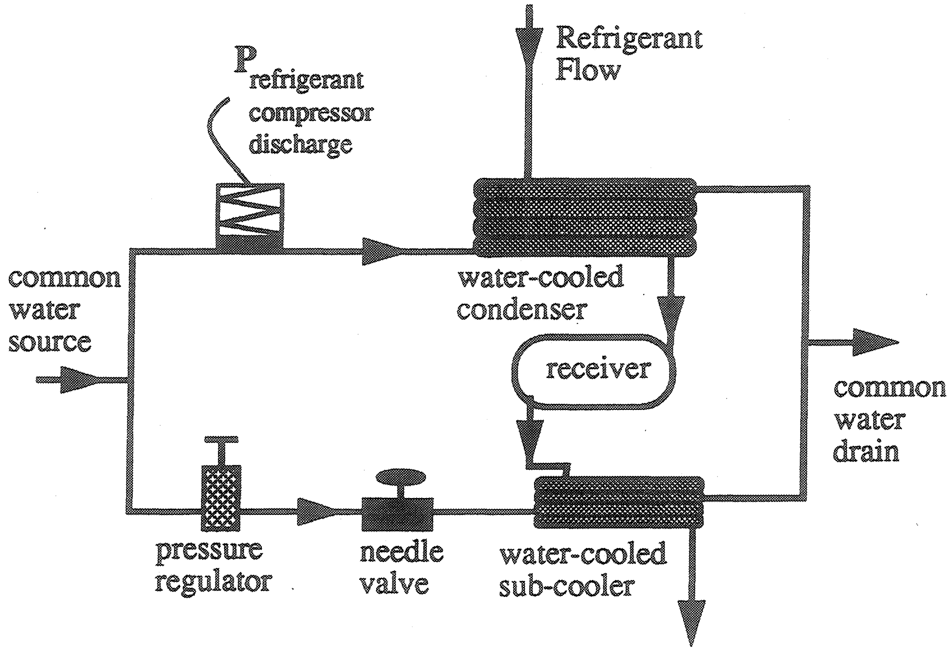

Figure 5.6 Refrigerant Condenser Pressure Control Mechanism

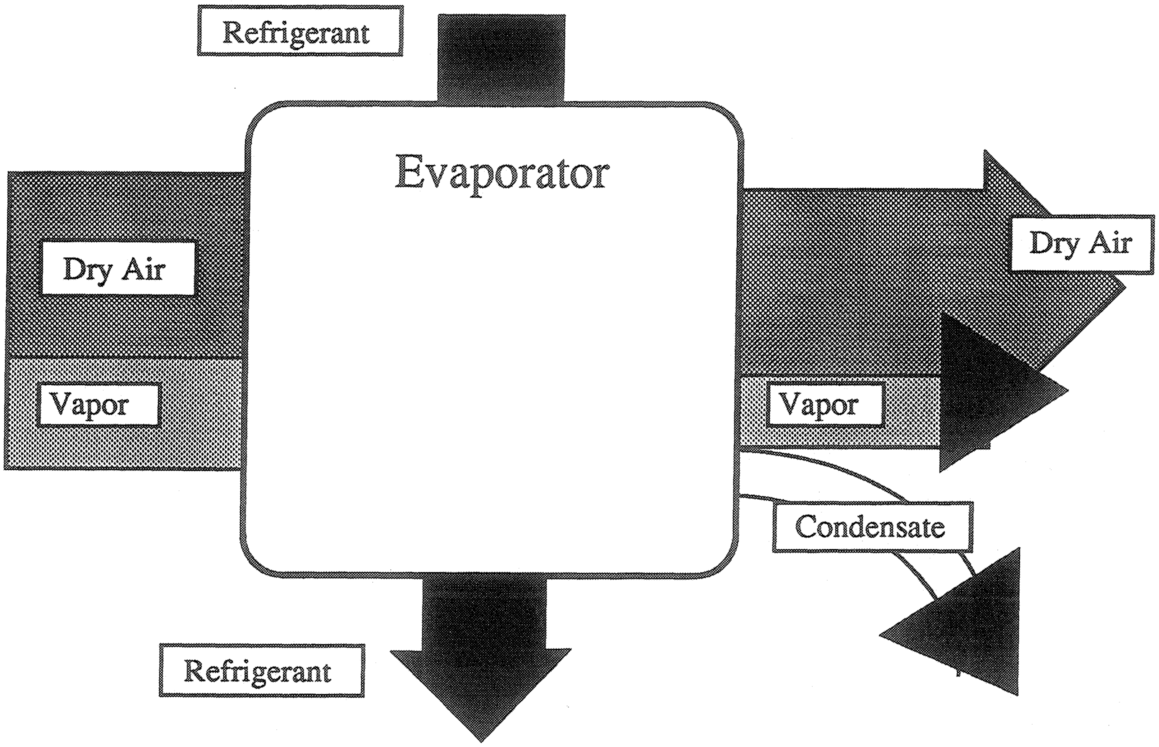

Figure 5.7 Control Volume for an Adiabatic Evaporator

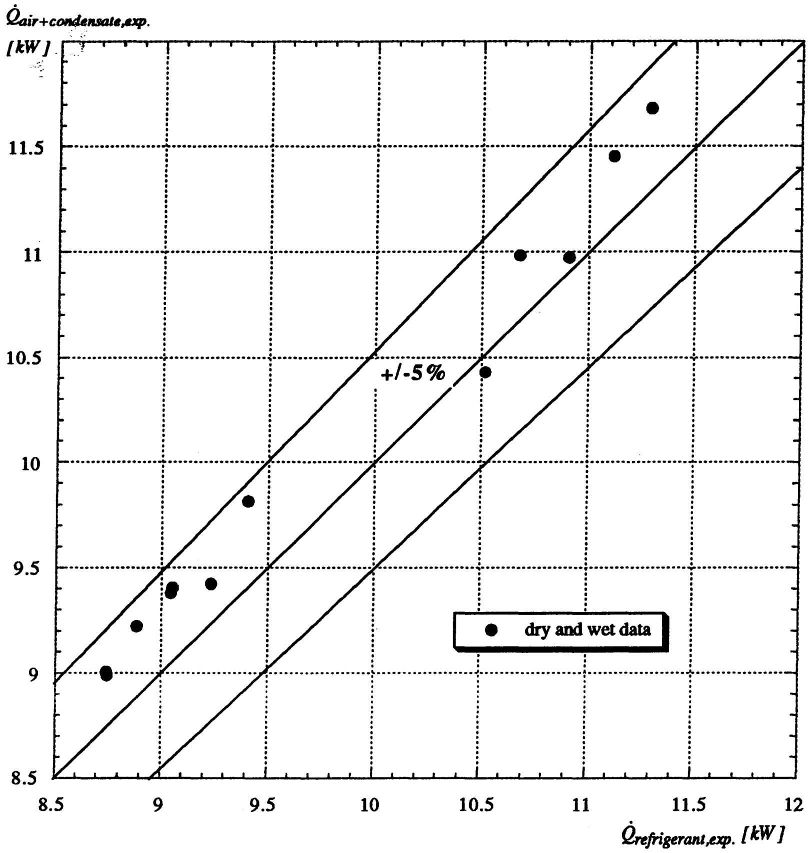

Figure 5.8a Experimental Heat Balance for Coil A and HCFC-22

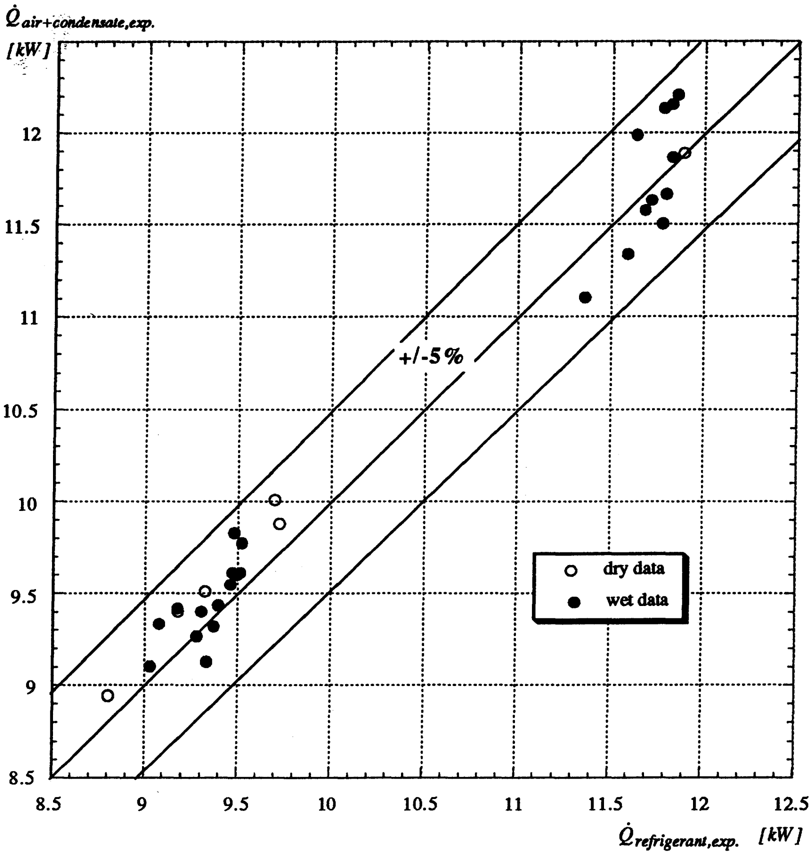

Figure 5.8b Experimental Heat Balance for Coil A and HFC-32/HFC-125/HFC-134a (23/25/52%)

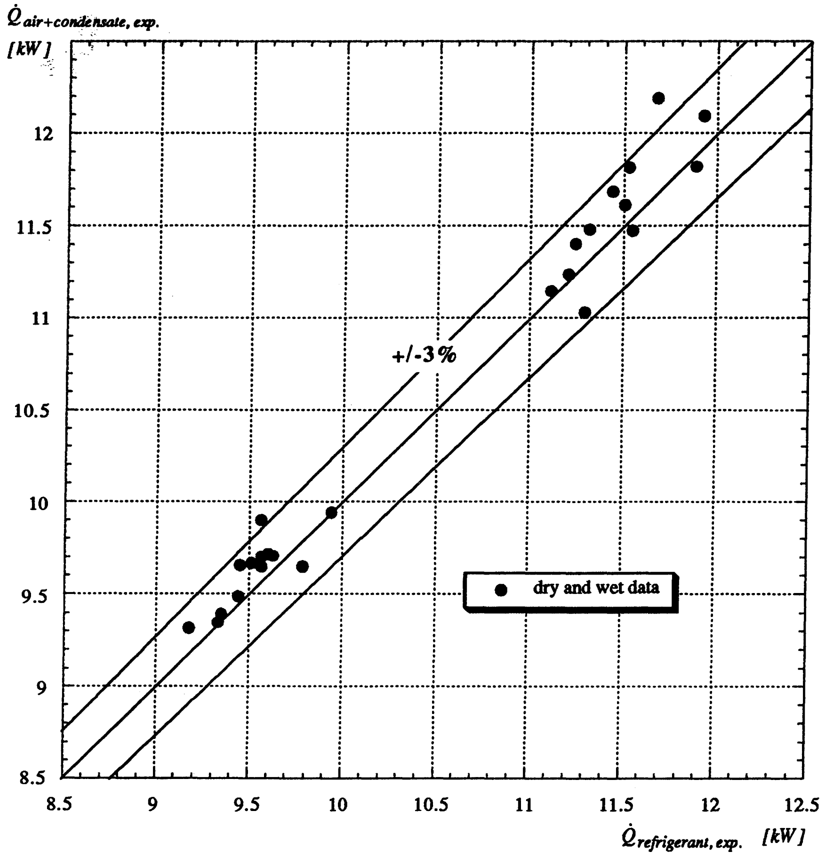

Figure 5.8c Experimental Heat Balance for Coil B and HFC-32/HFC-125/HFC-134a (23/25/52%)

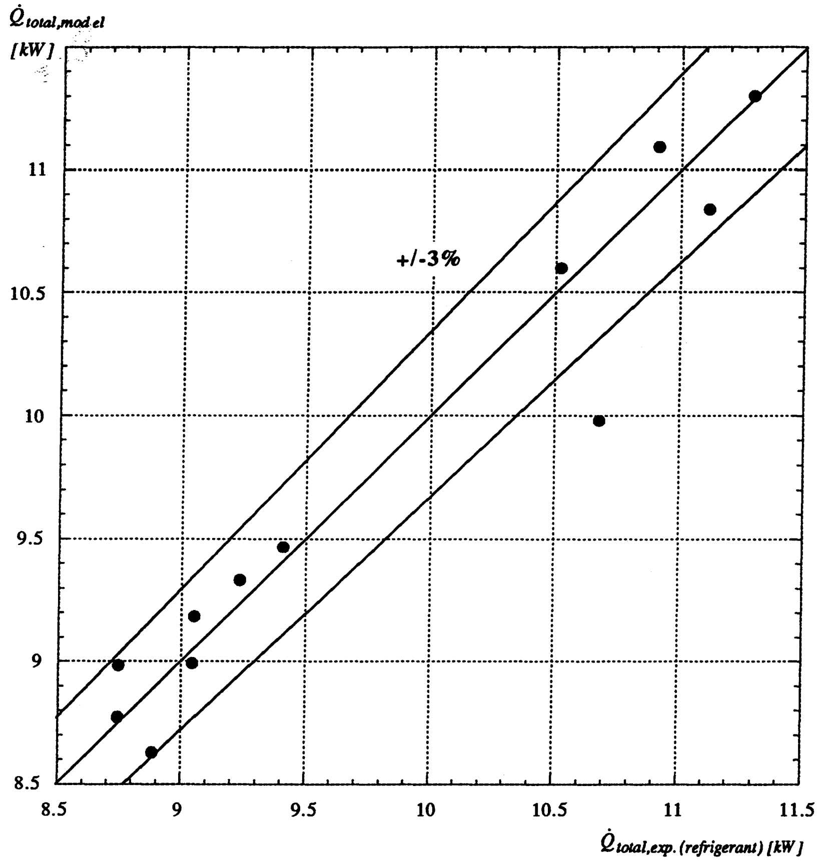

Figure 5.9a Theoretical and Experimental Total Rates of Heat Transfer for Coil A and HCFC-22 with the Discretized Differential Equations Model

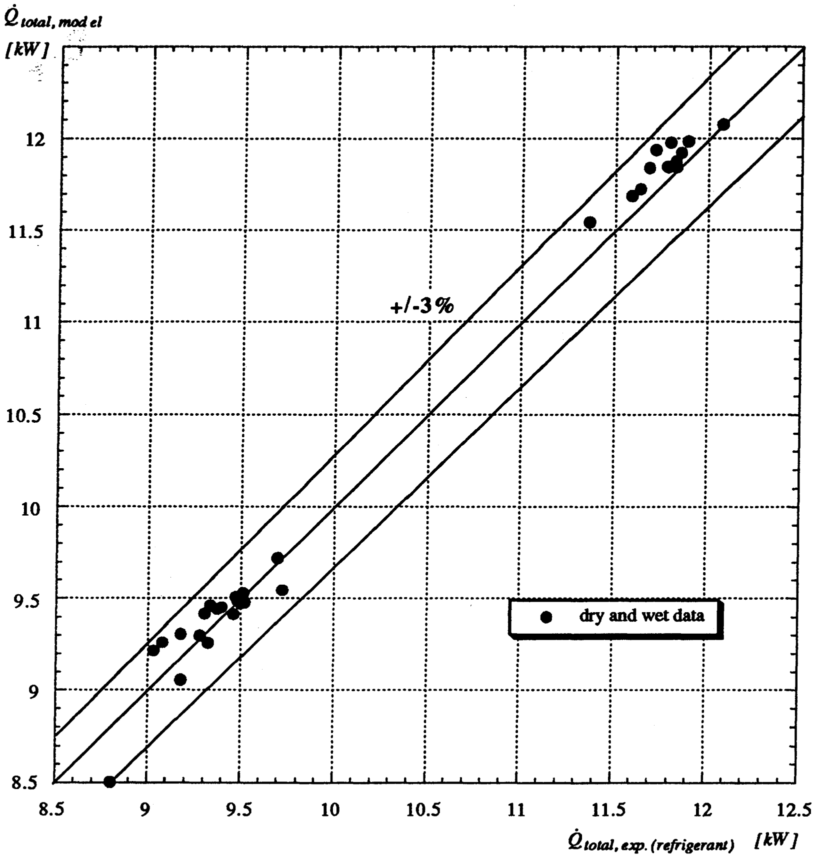

Figure 5.9b Theoretical and Experimental Total Rates of Heat Transfer for Coil A and HFC-32/HFC-125/HFC-134a (23/25/52%) with the Discretized Differential Equations Model

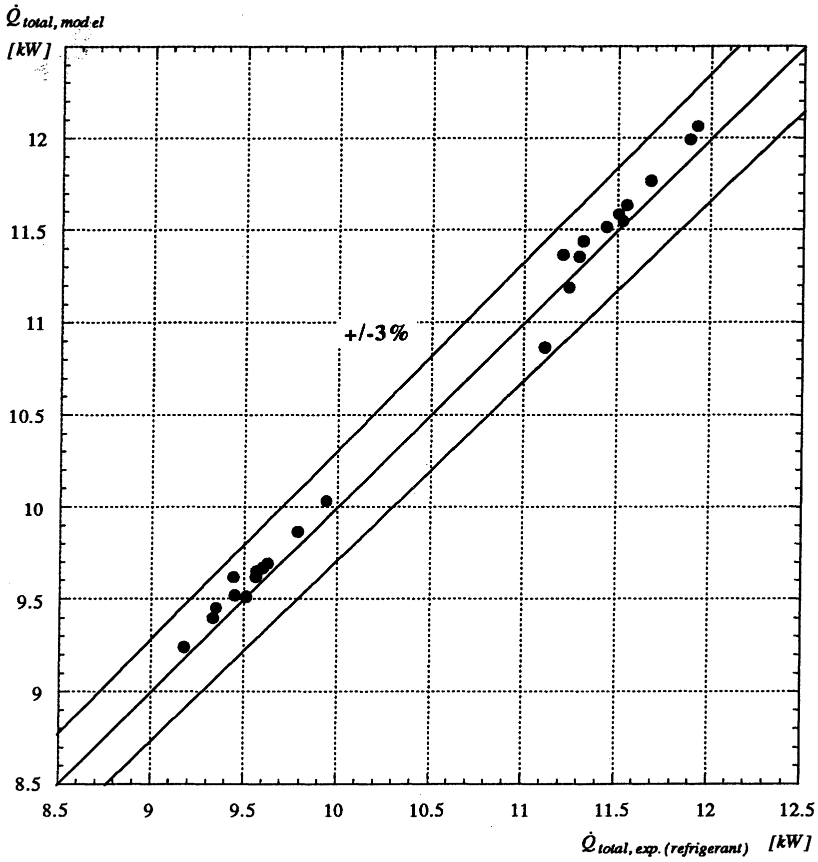

Figure 5.9c Theoretical and Experimental Total Rates of Heat Transfer for Coil B and HFC-32/HFC-125/HFC-134a (23/25/52%) with the Discretized Differential Equations Model

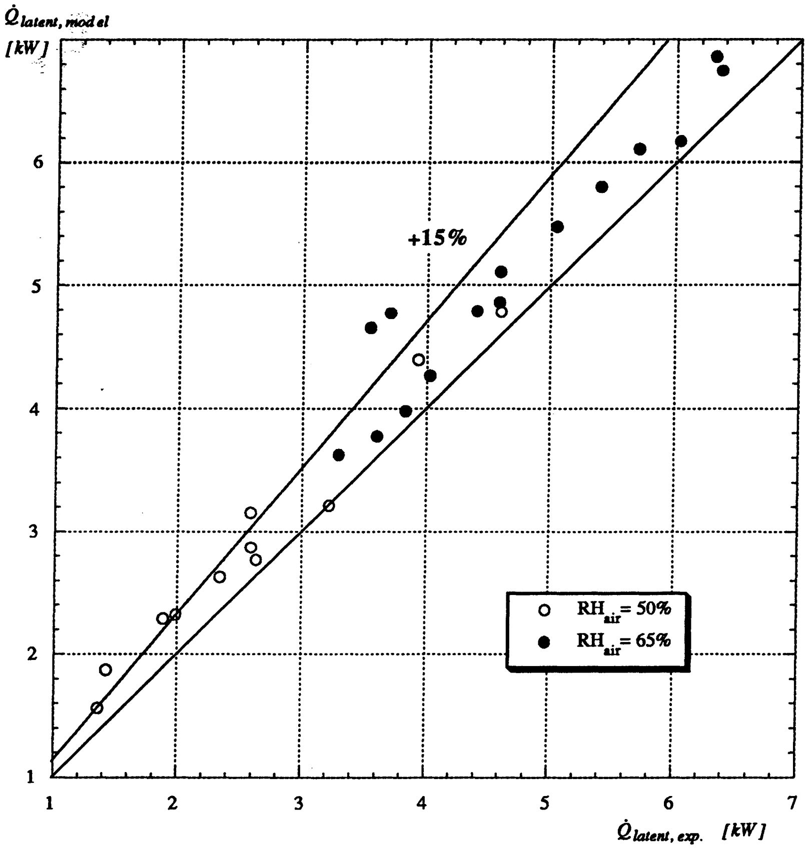

Figure 5.10a Theoretical and Experimental Latent Rates of Heat Transfer for Coil A and HFC-32/HFC-125/HFC-134a (23/25/52%) with the Discretized Differential Equations Model

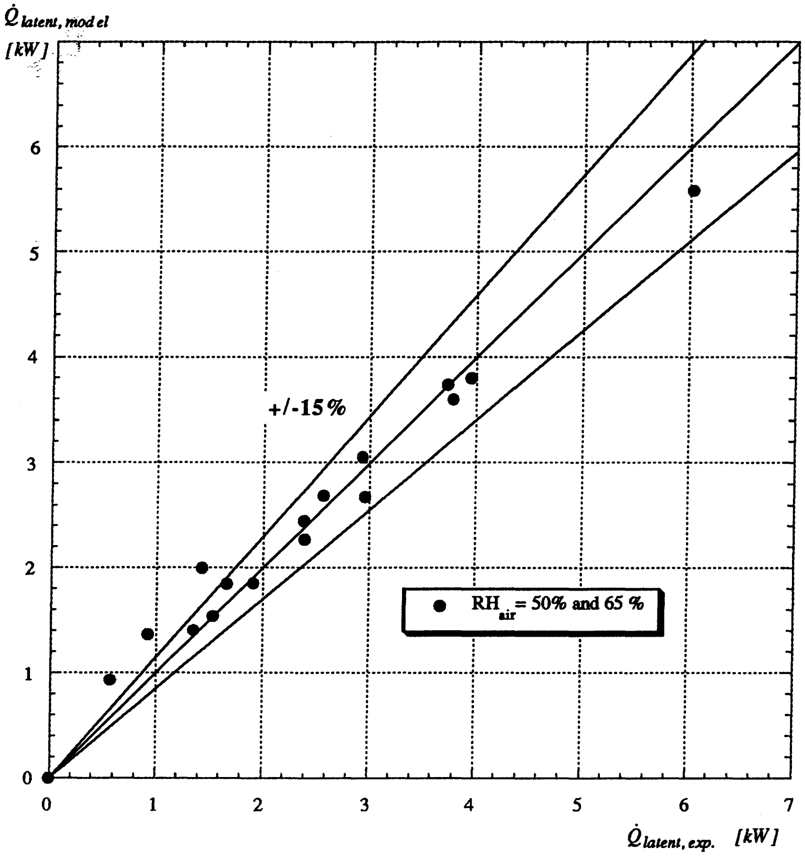

Figure 5.10b Theoretical and Experimental Latent Rates of Heat Transfer for Coil B and HFC-32/HFC-125/HFC-134a (23/25/52%) with the Discretized Differential Equations Model

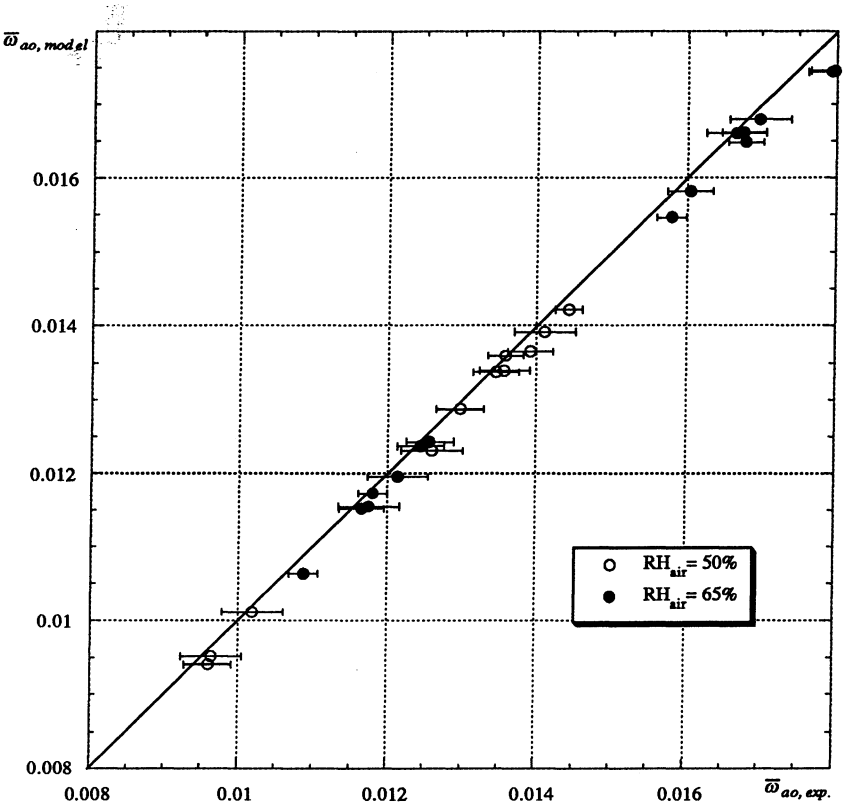

Figure 5.11a Theoretical and Experimental Average Air Outlet Humidity Ratios for Coil A and HFC-32/HFC-125/HFC-134a (23/25/52%) with the Discretized Differential Equations Model (including experimental uncertainty)

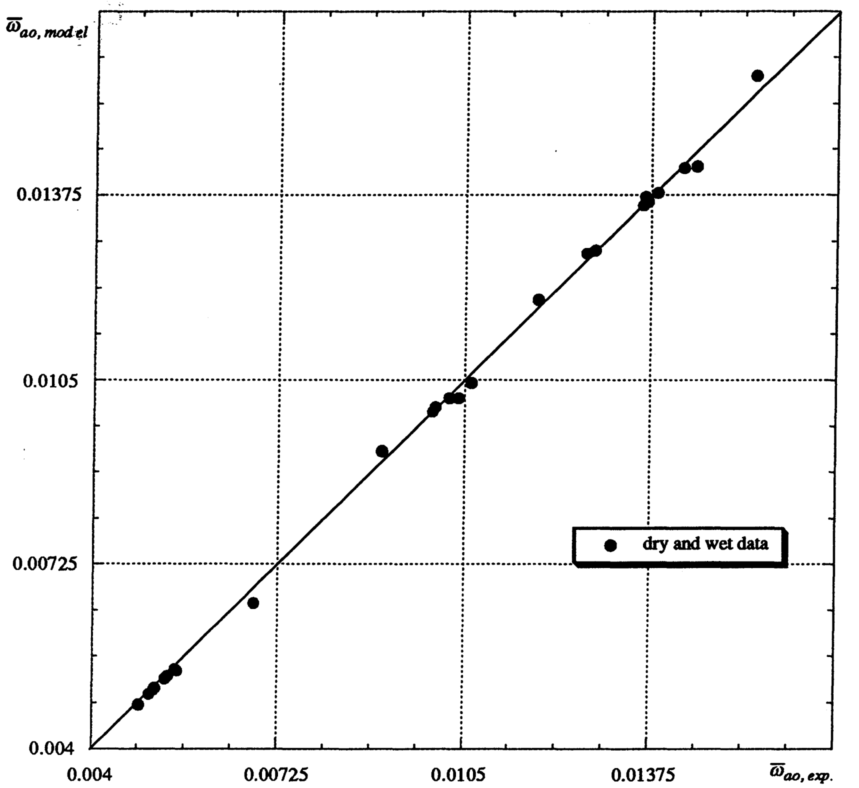

Figure 5.11b Theoretical and Experimental Average Air Outlet Humidity Ratios for Coil B and HFC-32/HFC-125/HFC-134a (23/25/52%) with the Discretized Differential Equations Model

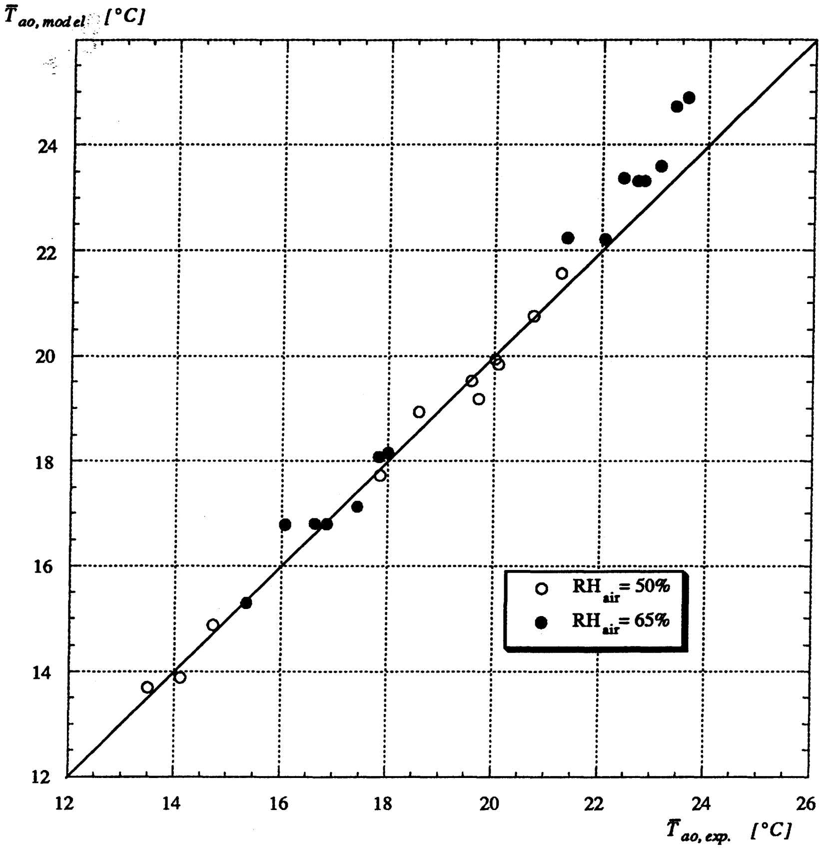

Figure 5.12a Theoretical and Experimental Average Air Outlet Temperatures for Coil A and HFC-32/HFC-125/HFC-134a (23/25/52%) with the Discretized Differential Equations Model

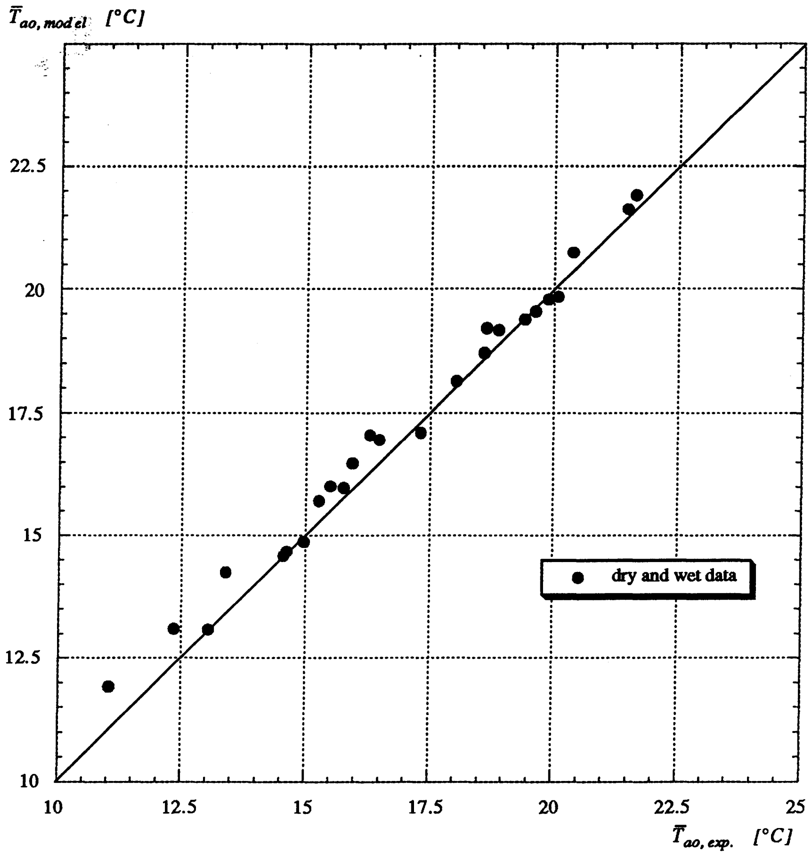

Figure 5.12b Theoretical and Experimental Average Air Outlet Temperatures for Coil B and HFC-32/HFC-125/HFC-134a (23/25/52%) with the Discretized Differential Equations Model

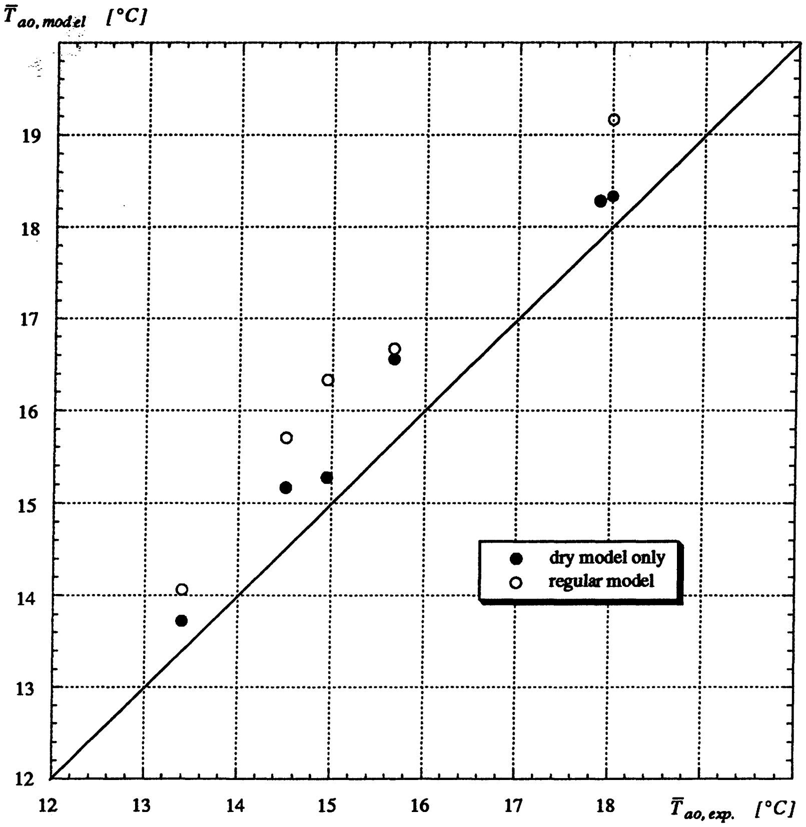

Figure 5.13 Theoretical and Experimental Average Air Outlet Temperatures for Coil A and HFC-32/HFC-125/HFC-134a (23/25/52%) with the Discretized Differential Equations Model (with and without Forced Dry Operation)

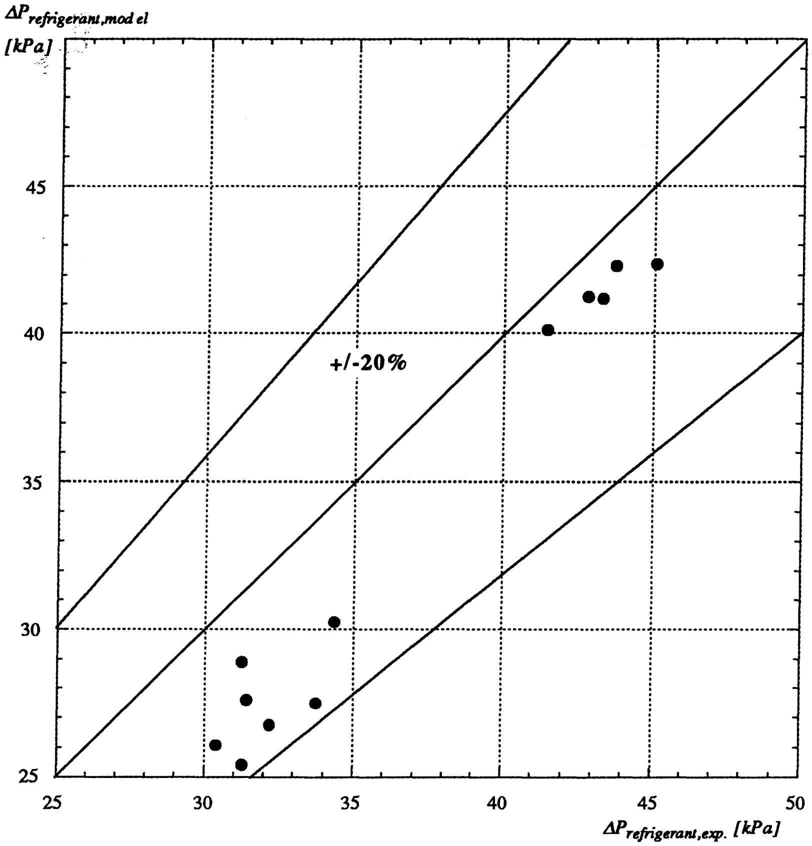

Figure 5.14a Theoretical and Experimental Refrigerant Pressure Drops for Coil A and HCFC-22

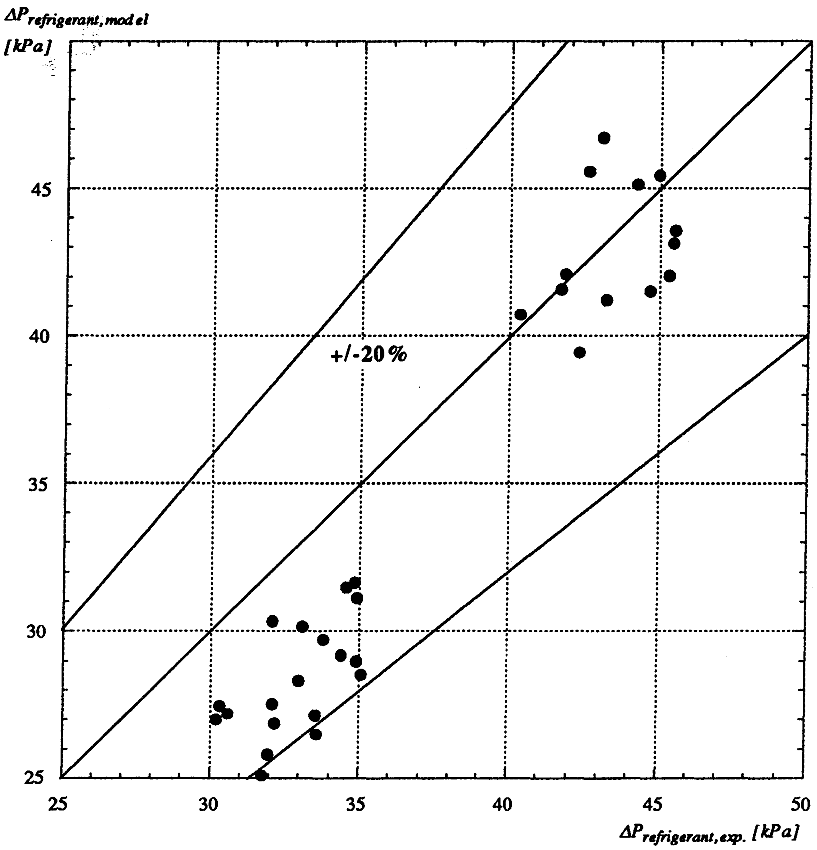

Figure 5.14b Theoretical and Experimental Refrigerant Pressure Drops for Coil A and HFC-32/HFC-125/HFC-134a (23/25/52%)

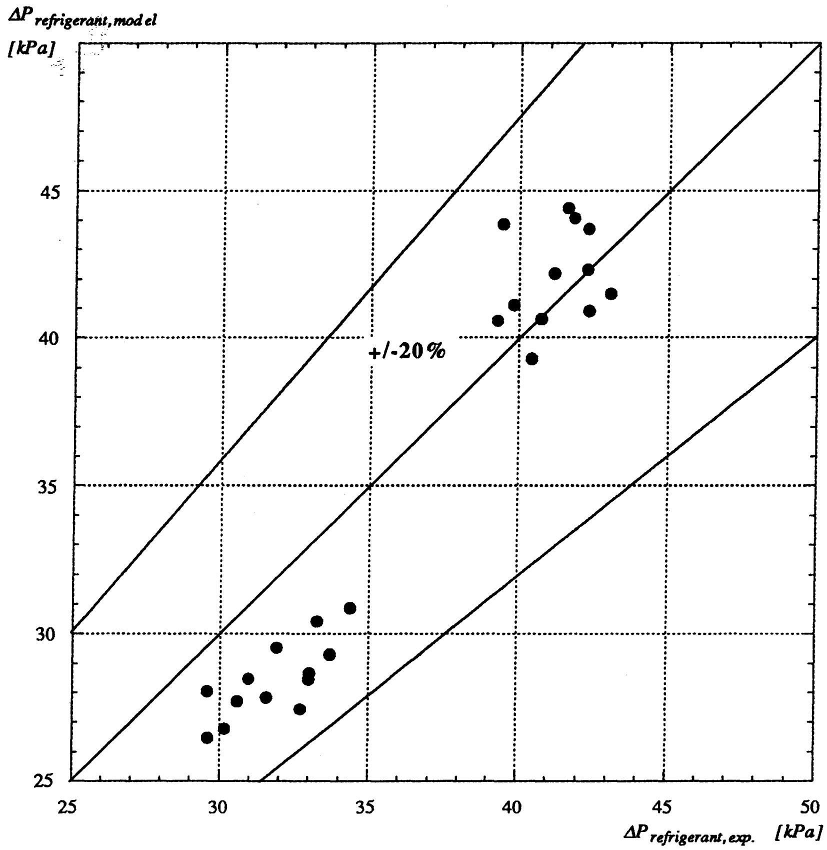

Figure 5.14c Theoretical and Experimental Refrigerant Pressure Drops for Coil B and HFC-32/HFC-125/HFC-134a (23/25/52%)

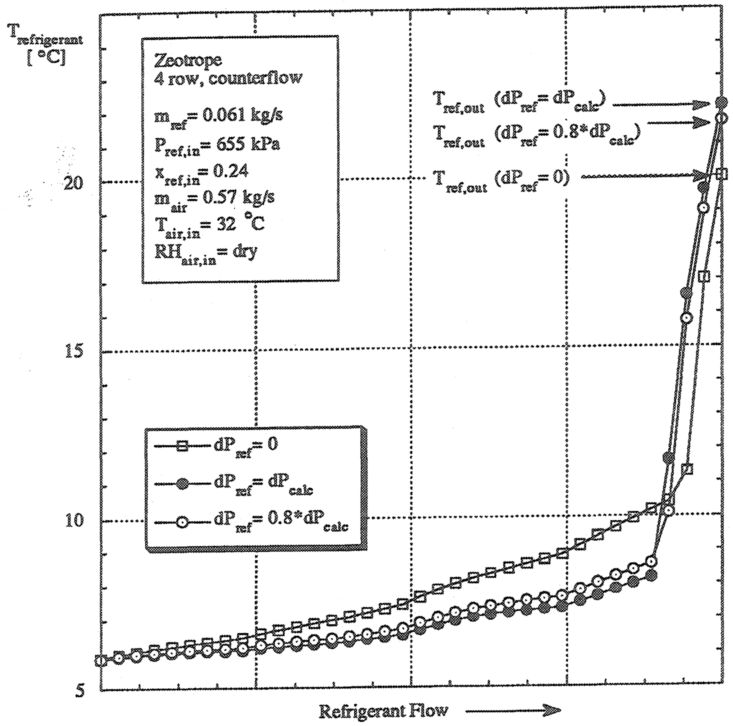

Figure 5.15 Effect of Refrigerant Pressure Drop on its Temperature Profile in a Cross-Counterflow Exchanger with HFC-32/HFC-125/HFC-134a (23/25/52%)

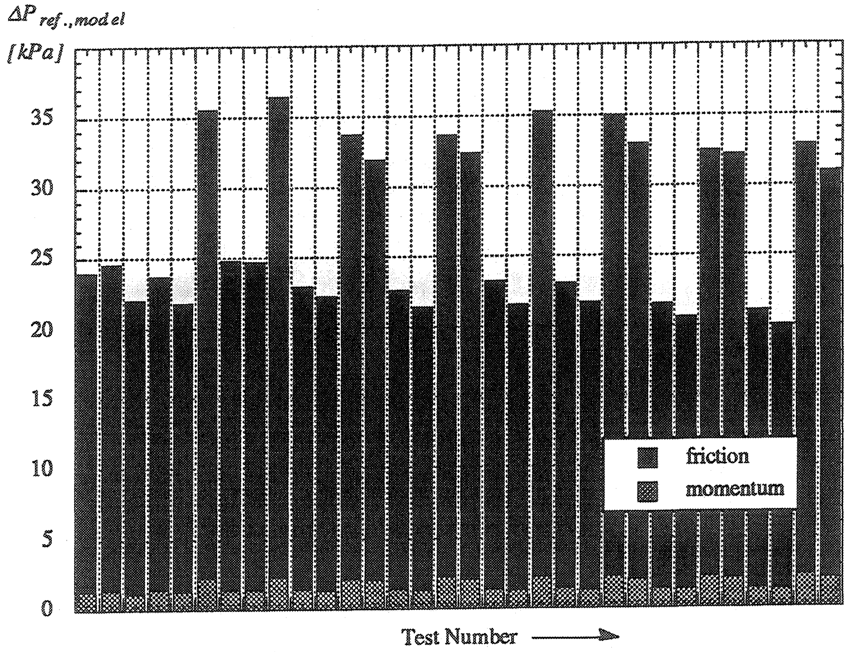

Figure 5.16 Main Contributions to the Total Refrigerant Pressure Drop for Coil A and HFC-32/HFC-125/HFC-134a (23/25/52%)

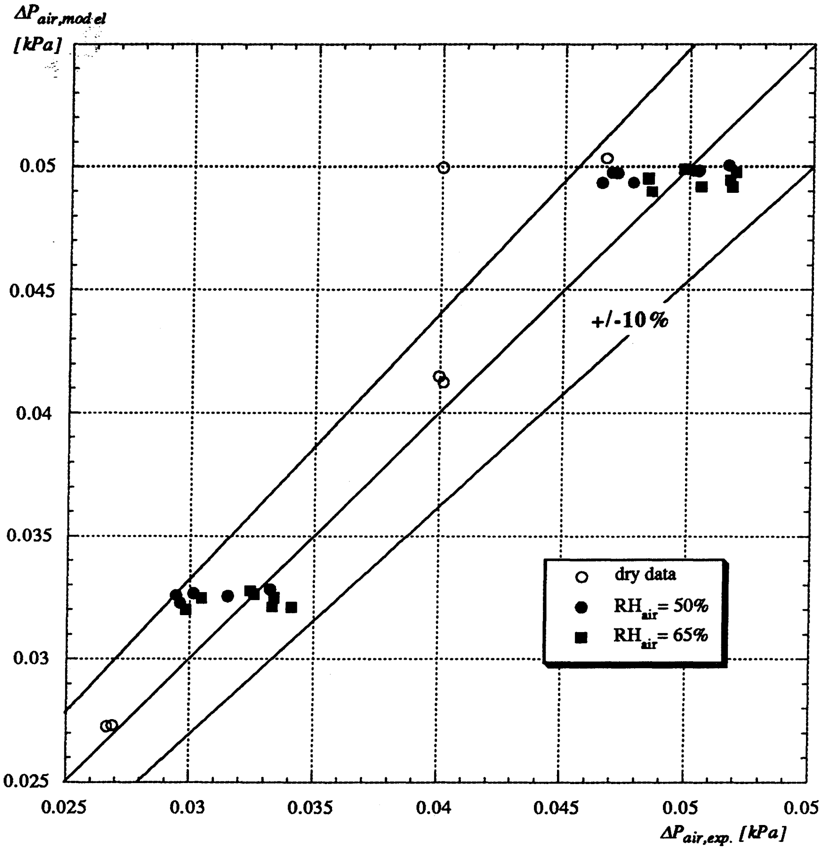

Figure 5.17 Theoretical and Experimental Air Pressure Drops for Coil A and HFC-32/HFC-125/HFC-134a (23/25/52%)

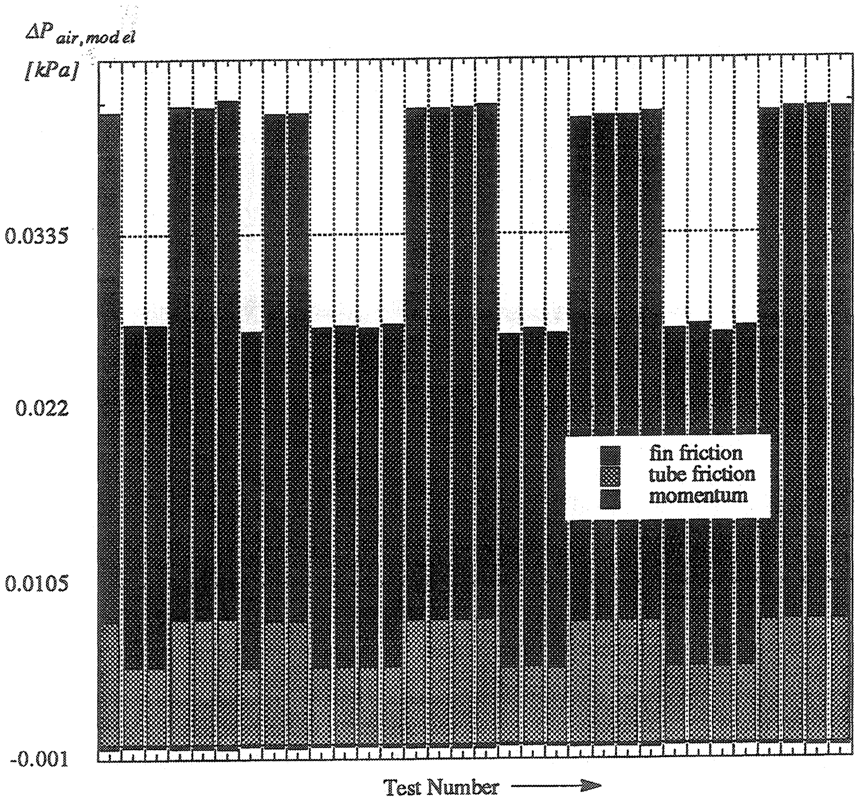

Figure 5.18 Contributions to the Total Air Pressure Drop for Coil A and HFC-32/HFC-125/HFC-134a (23/25/52%)

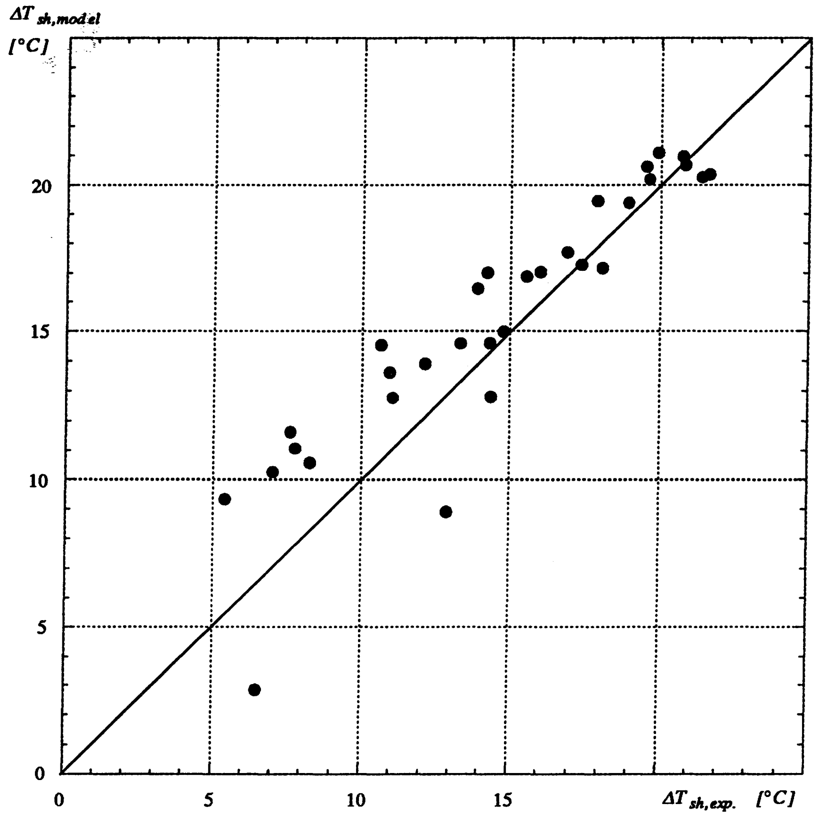

Figure 5.19a Theoretical and Experimental Refrigerant Superheat for Coil A and HFC-32/HFC-125/HFC-134a (23/25/52%)

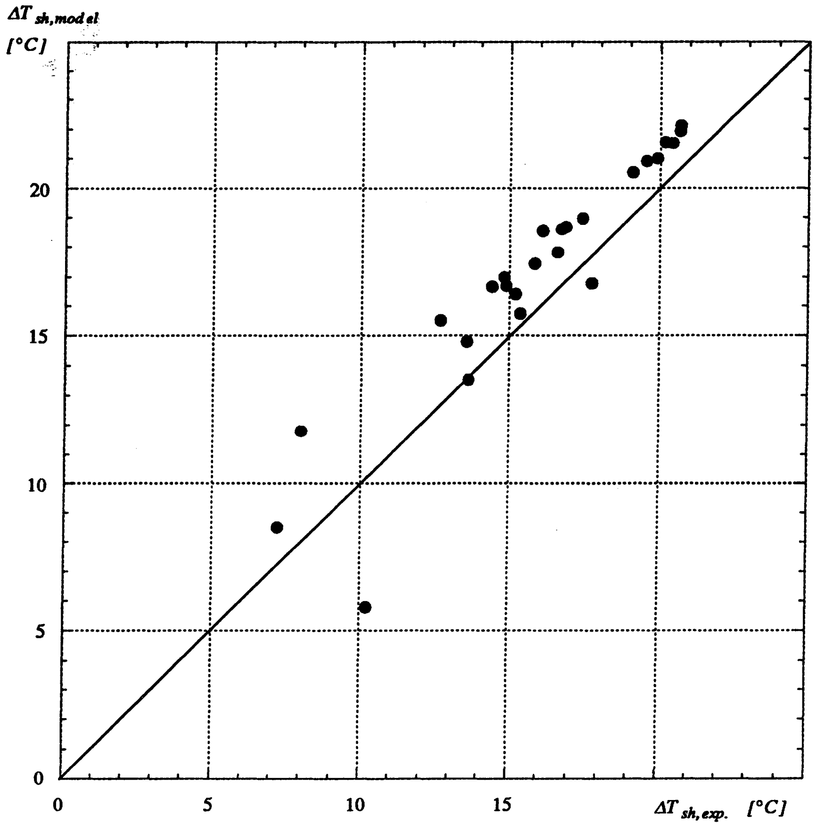

Figure 5.19b Theoretical and Experimental Refrigerant Superheat for Coil B and HFC-32/HFC-125/HFC-134a (23/25/52%)

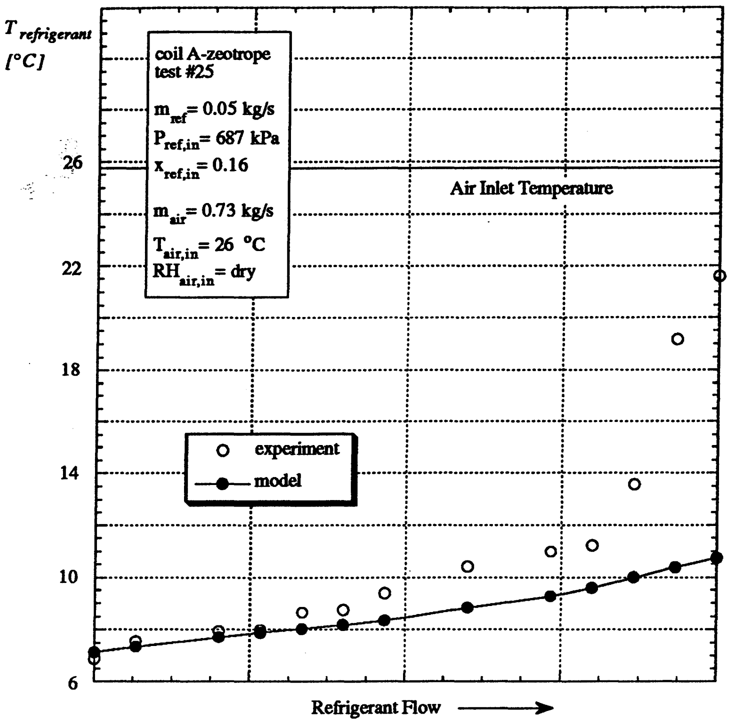

Figure 5.20a Evaporator Refrigerant Temperature Profiles for Coil A and HFC-32/HFC-125/HFC-134a (23/25/52%)

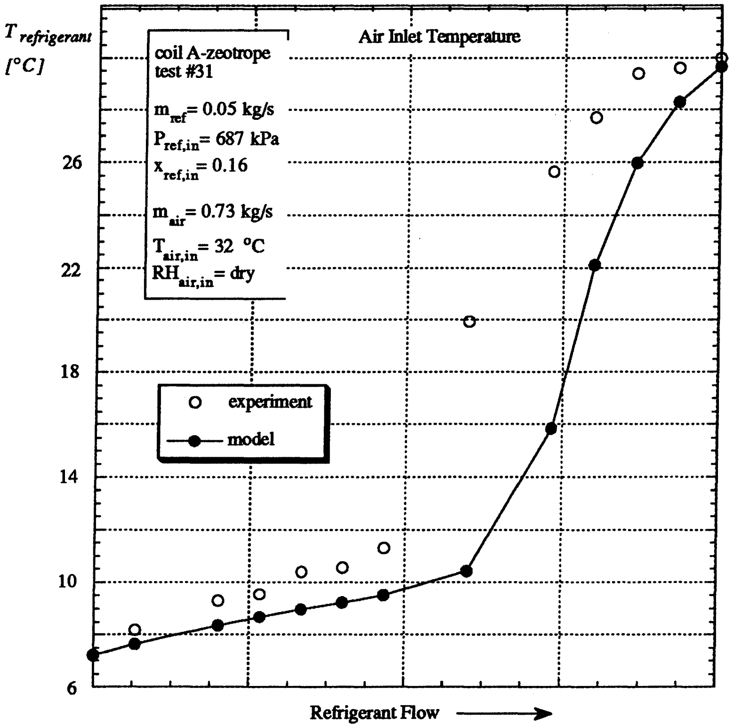

Figure 5.20b Evaporator Refrigerant Temperature Profiles for Coil A and HFC-32/HFC-125/HFC-134a (23/25/52%)

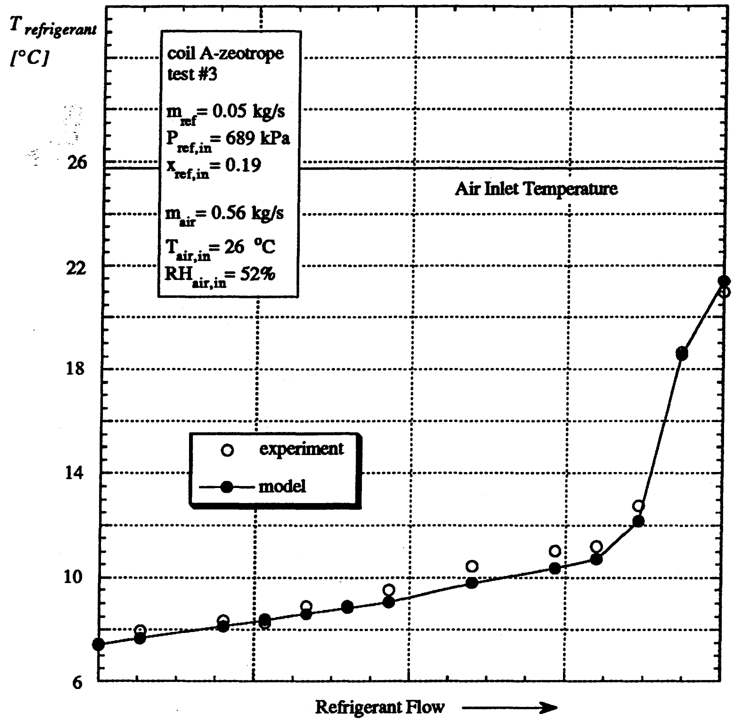

Figure 5.20c Evaporator Refrigerant Temperature Profiles for Coil A and HFC-32/HFC-125/HFC-134a (23/25/52%)

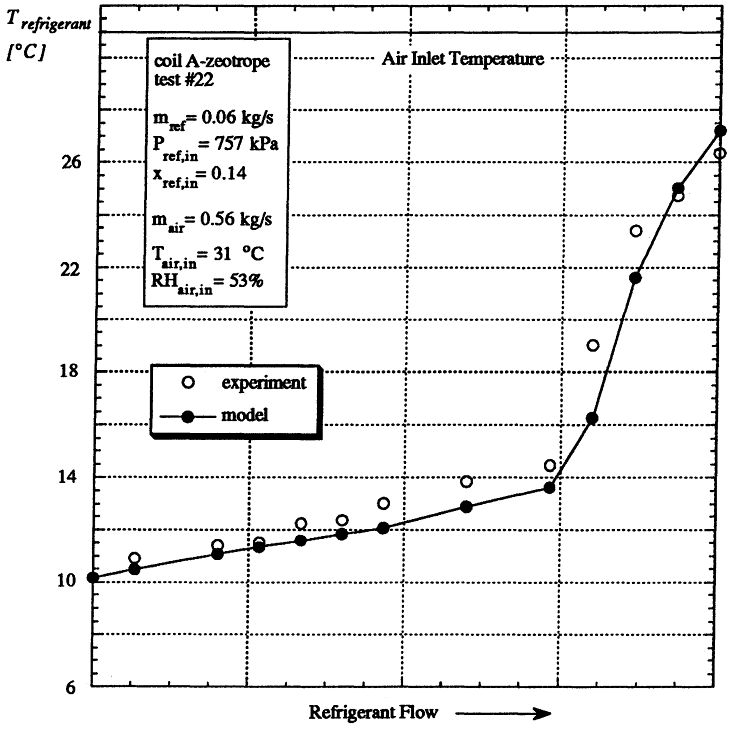

Figure 5.20d Evaporator Refrigerant Temperature Profiles for Coil A and HFC-32/HFC-125/HFC-134a (23/25/52%)

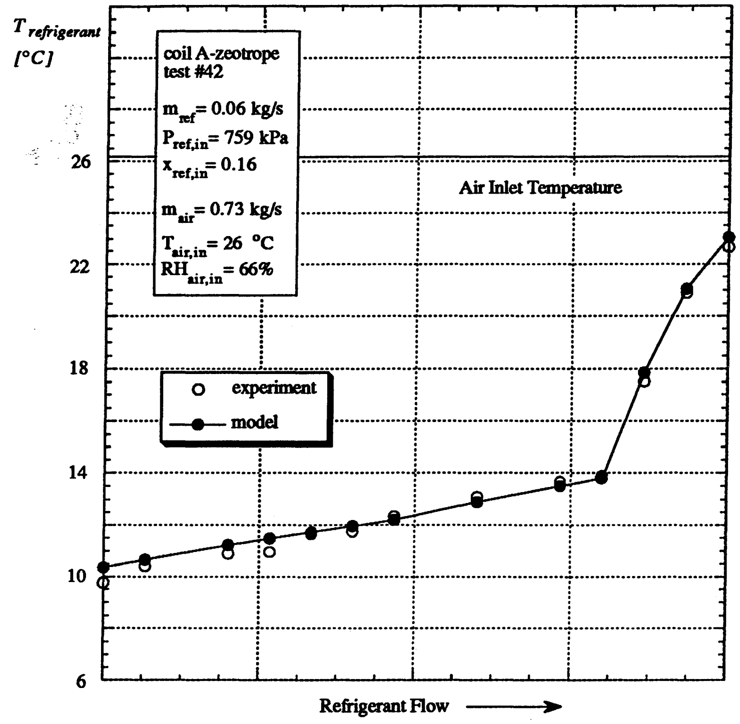

Figure 5.20e Evaporator Refrigerant Temperature Profiles for Coil A and HFC-32/HFC-125/HFC-134a (23/25/52%)

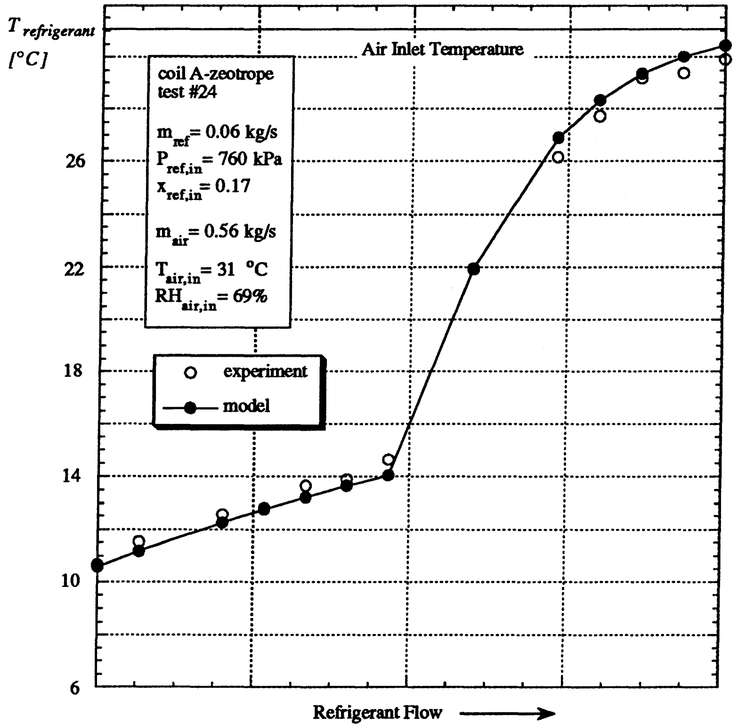

Figure 5.20f Evaporator Refrigerant Temperature Profiles for Coil A and HFC-32/HFC-125/HFC-134a (23/25/52%)

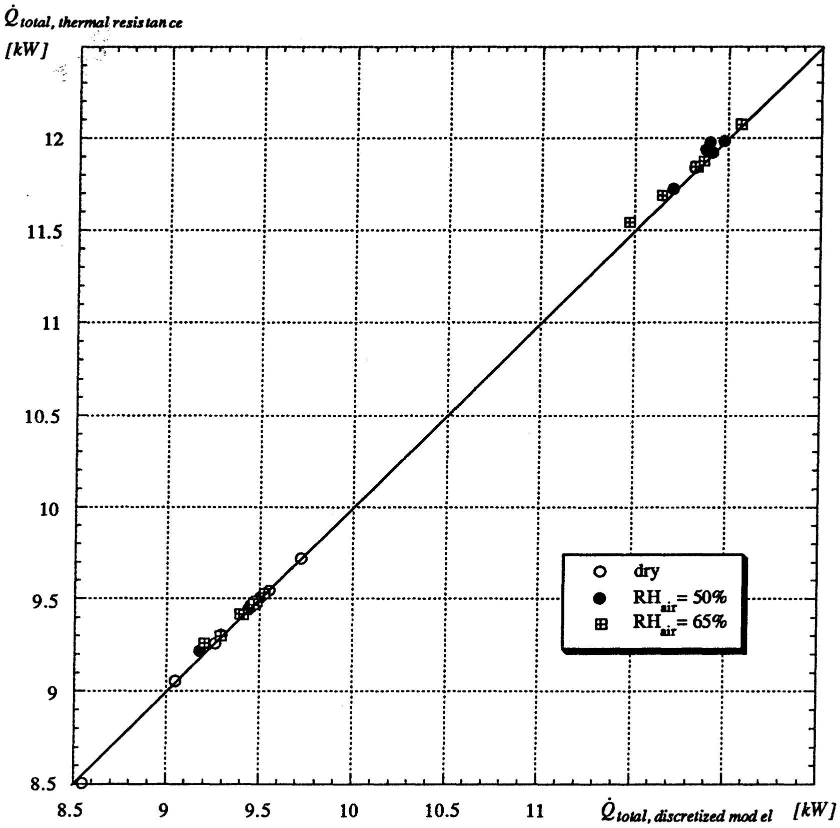

Figure 5.21a Theoretical Rates of Heat Transfer for Coil A and HFC-32/HFC-125/HFC-134a (23/25/52%) with the Discretized Differential Equations and Thermal Resistance Models

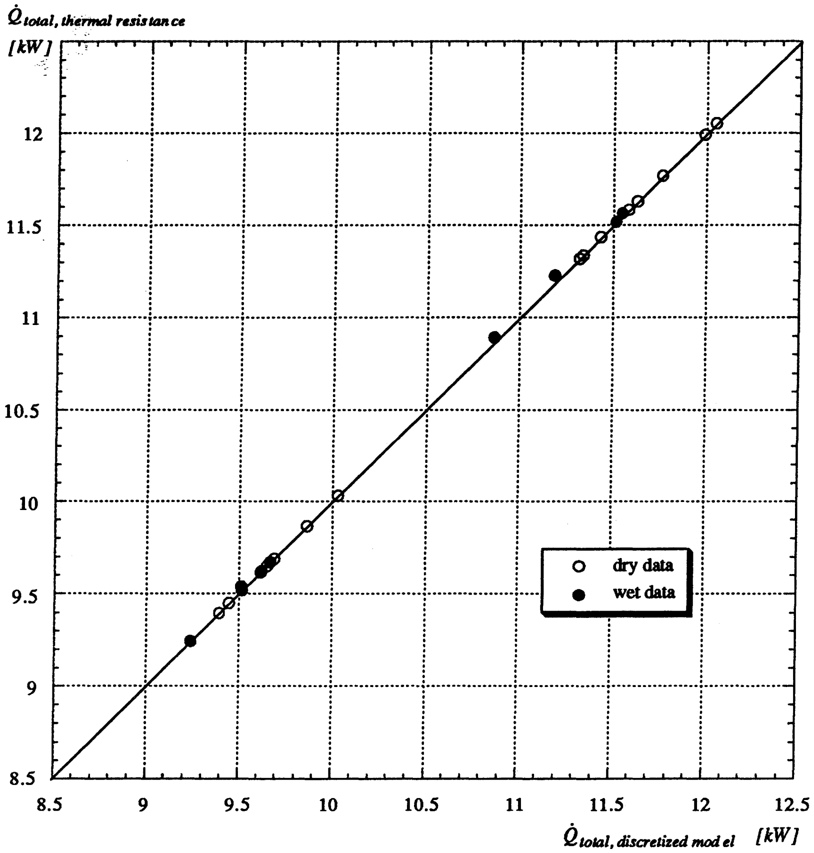

Figure 5.21b Theoretical Rates of Heat Transfer for Coil B and HFC-32/HFC-125/HFC-134a (23/25/52%) with the Discretized Differential Equations and Thermal Resistance Models

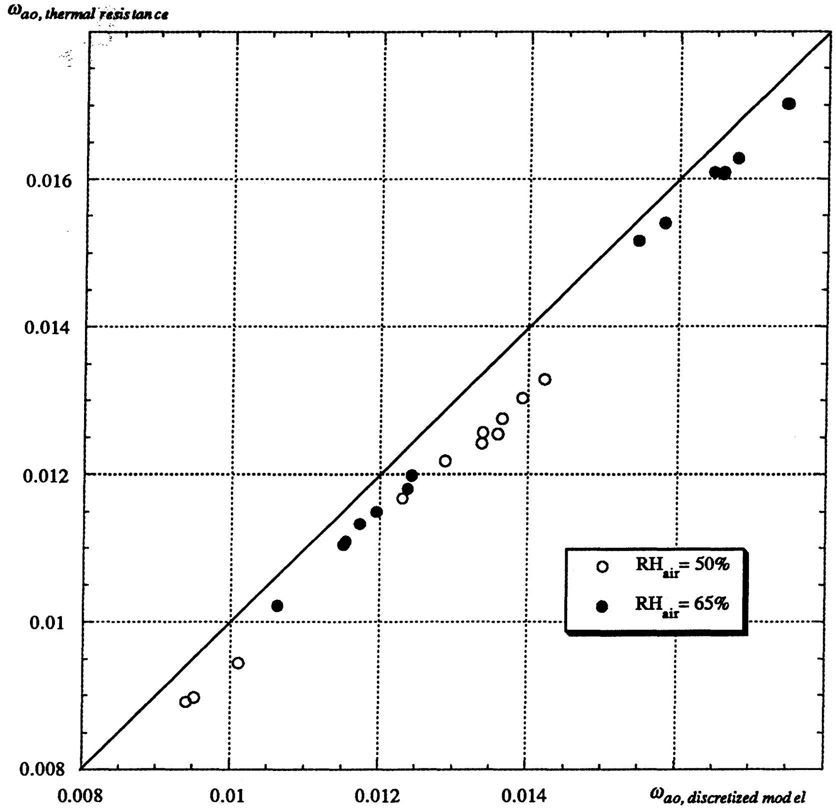

Figure 5.22a Theoretical Air Outlet Humidity Ratios for Coil A and HFC-32/HFC-125/HFC-134a (23/25/52%) with the Discretized Differential Equations and Thermal Resistance Models

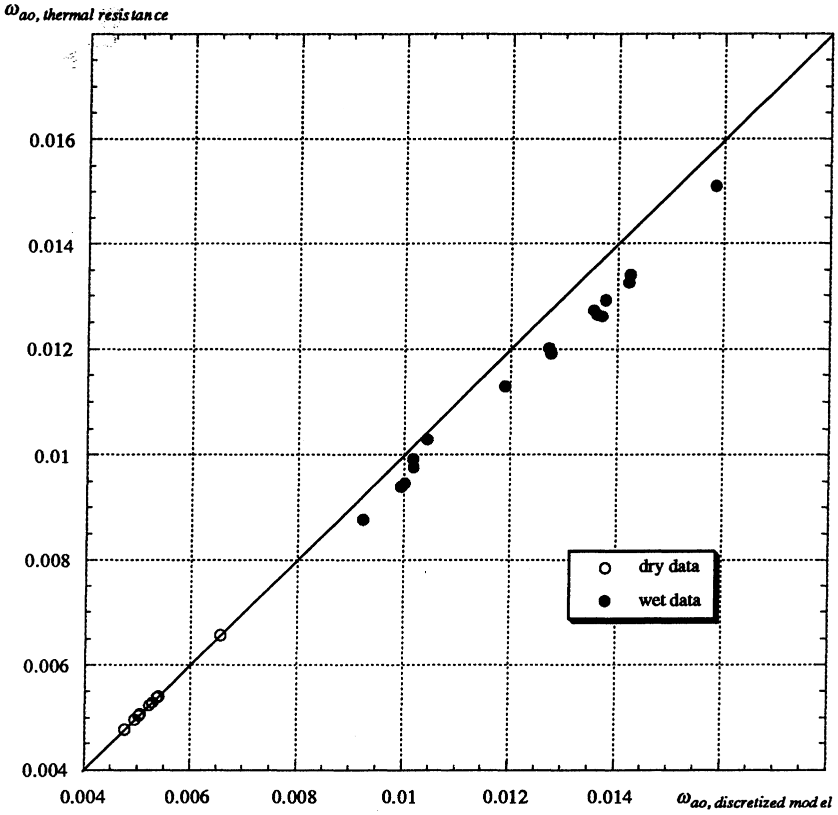

Figure 5.22b Theoretical Air Outlet Humidity Ratios for Coil B and HFC-32/HFC-125/HFC-134a (23/25/52%) with the Discretized Differential Equations and Thermal Resistance Models

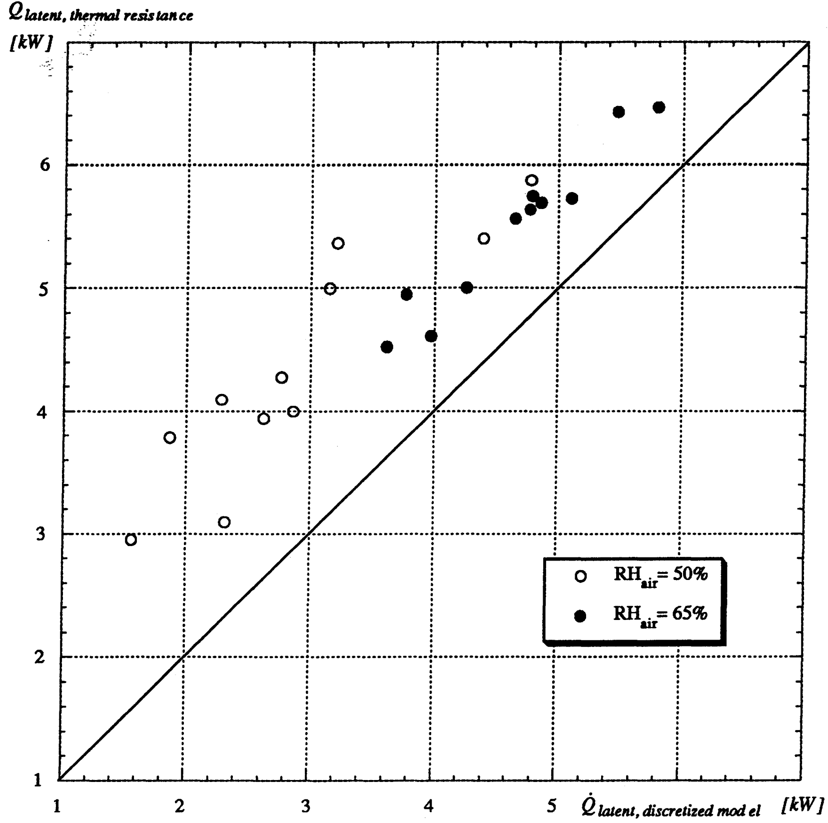

Figure 5.23a Theoretical Latent Rates of Heat Transfer for Coil A and HFC-32/HFC-125/HFC-134a (23/25/52%) with the Discretized Differential Equations and Thermal Resistance Models

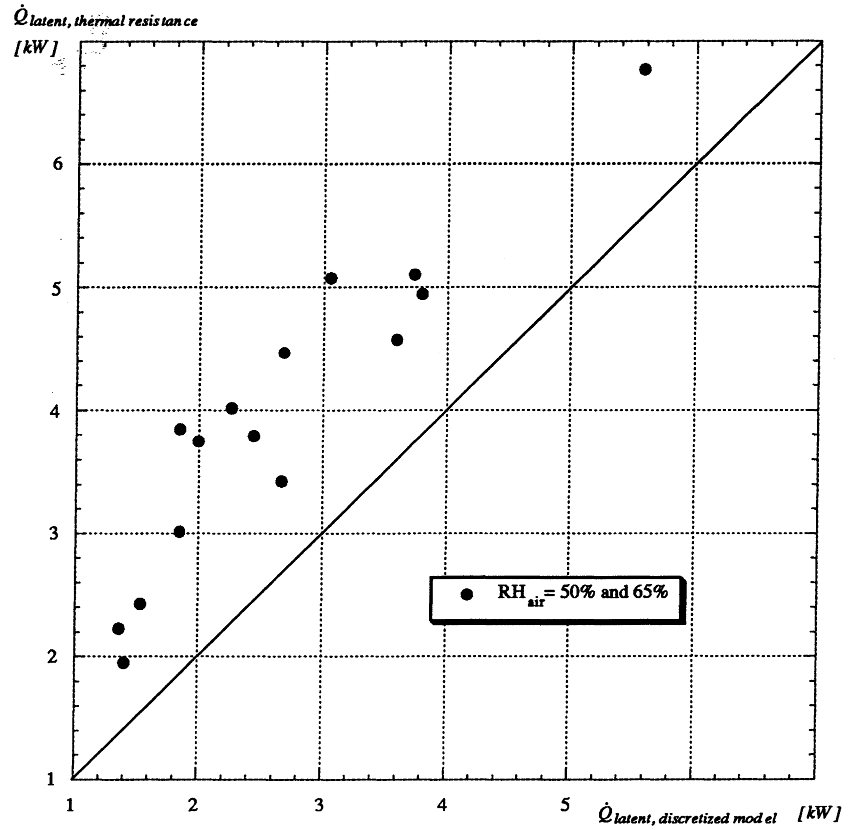

Figure 5.23b Theoretical Latent Rates of Heat Transfer for Coil B and HFC-32/HFC-125/HFC-134a (23/25/52%) with the Discretized Differential Equations and Thermal Resistance Models

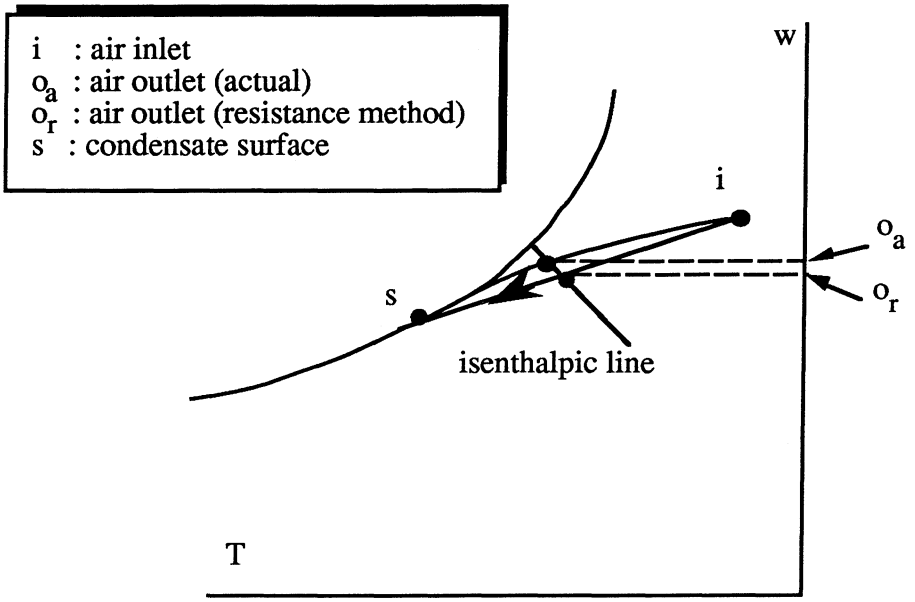

Figure 5.24 Linearized Air Path Assumption by the Thermal Resistance Model

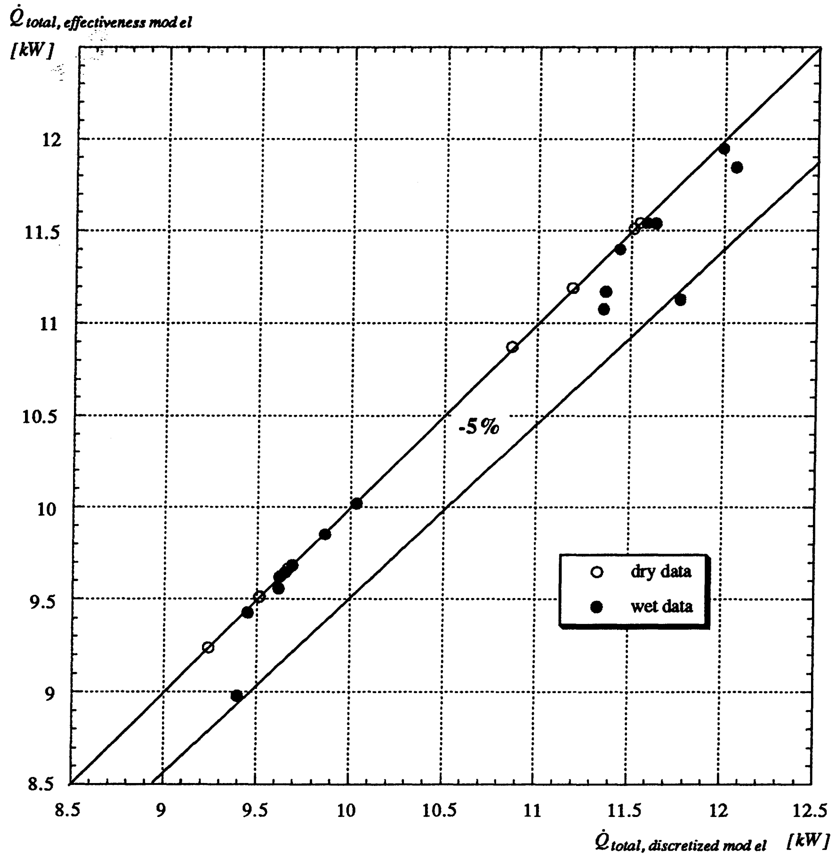

Figure 5.25 Theoretical Rates of Heat Transfer with the Discretized Differential Equations and the Effectiveness Models for Coil B and HFC-32/HFC-125/HFC-134a (23/25/52%)

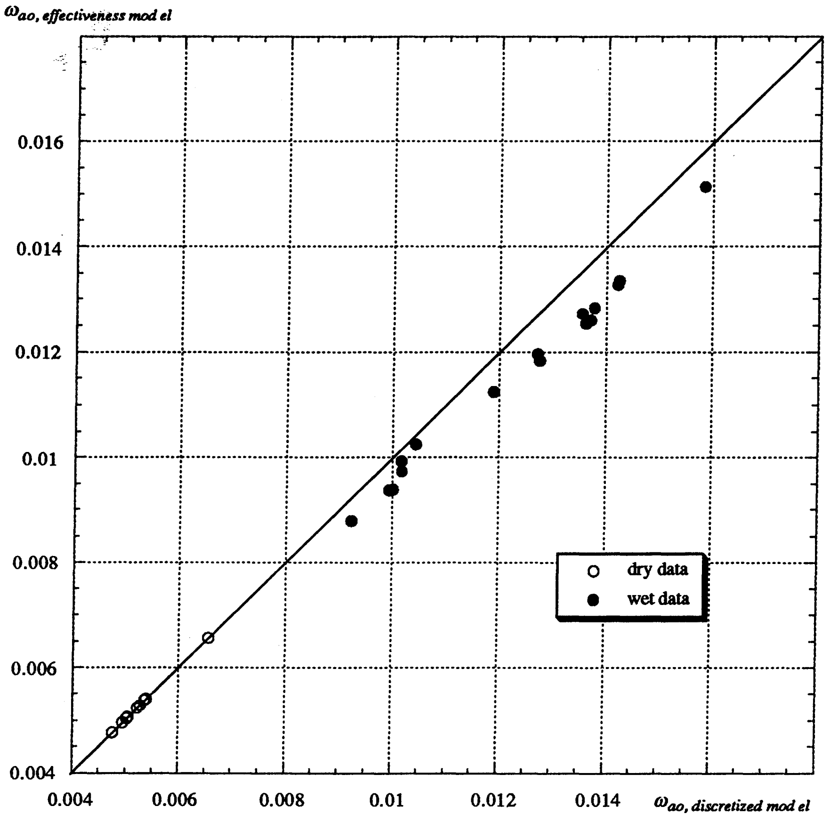

Figure 5.26 Theoretical Air Outlet Humidity Ratios with the Discretized Differential Equations and the Effectiveness Models for Coil B and HFC-32/HFC-125/HFC-134a (23/25/52%)

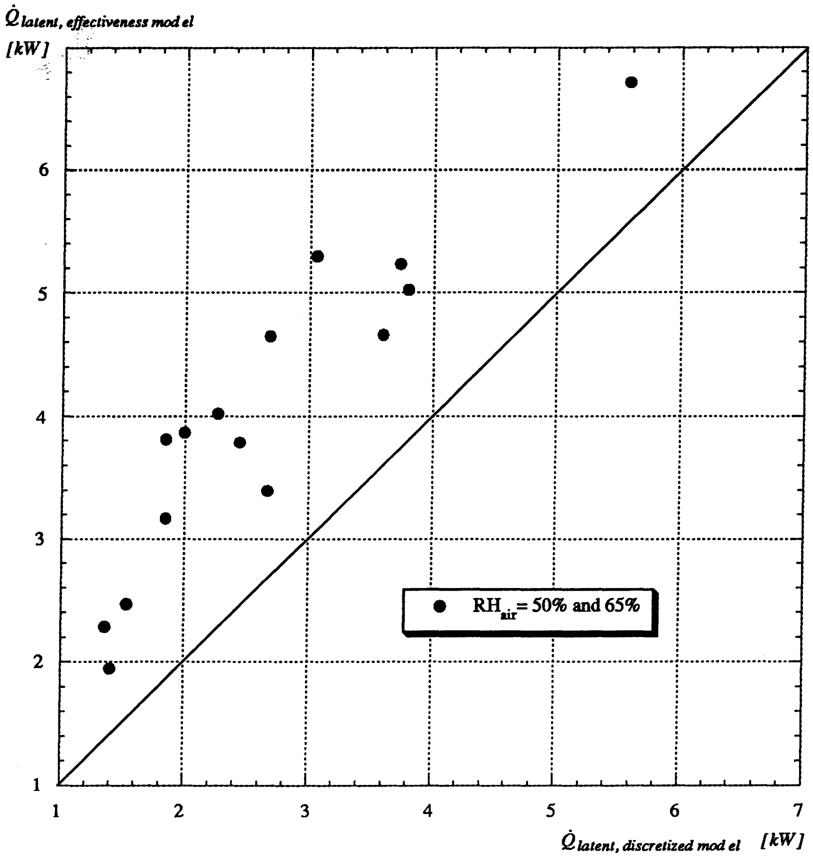

Figure 5.27 Theoretical Rates of Latent Heat Transfer with the Discretized Differential Equations and the Effectiveness Models for Coil B and HFC-32/HFC-125/HFC-134a (23/25/52%)

CHAPTER 6
OPTIMIZATION RESULTS

A design optimization study was conducted, using the evaporator model described in Chapter 4 in order to evaluate the entropy generation function defined in Chapter 3. The current chapter describes the evaluation of evaporator designs as part of an effort to determine the sensitivity of the irreversibility function on both design and operating parameters, and to search for a design that would maximize evaporator and system performances.

The first section discusses the accuracy of the model in predicting air and refrigerant outlet conditions, and its importance in terms of capturing the dependence of the generation function on operating conditions.

The second section presents an analysis aimed at quantifying the relative magnitude of irreversibilities caused by various processes within the exchanger. Both the nature and the accuracy of its results are discussed in this section as well.

The third, fourth, and fifth sections summarize the results of three types of sensitivity analysis of the entropy generation function, based on exchanger dimensions, tube arrangement, and refrigerant circuitry respectively. The importance of air and refrigerant temperature glide matching are considered in the sixth section.

Finally, the seventh section puts the potential efficiency gains in perspective, and discusses their implications on system performance.

6.1 Accuracy of the Entropy Generation Prediction

The ability of the evaporator model to predict the air and refrigerant outlet conditions with the accuracy needed to capture the irreversibility dependence on operating conditions was investigated. Figure 6.1 shows the net entropy generation function as calculated with Equation (3.19), based on theoretical and experimental results for the mixed refrigerant data sets collected with coil A.

The results were encouraging, indicating that the model predicted the irreversibility function with sufficient accuracy. It should be emphasized that the absolute error between modeling and experimental irreversibility results is not as important, as the fact that the model showed a significant sensitivity to the operating conditions for a fixed exchanger design.

The iterative nature of the model solution was a potential source of error in the calculation of the evaporator exergy loss. The small but finite discrepancy between the air and refrigerant-based rates of heat transfer was therefore evaluated for the case of a dry evaporator. When condensate formation is excluded from the analysis, the enthalpy components of the exergy function should cancel each other out in the calculation of the exergy loss, such that the latter becomes proportional to the net entropy change.

In equation form,

$$T_0\dot{S}_{gen} = \left[\dot{m}_{air}\cdot\left(h_{air,in} - h_{air,out}\right) + \dot{m}_{ref}\cdot\left(h_{ref,in} - h_{ref,out}\right)\right] - T_0\left[\dot{m}_{air}\cdot\left(s_{air,in} - s_{air,out}\right) + \dot{m}_{ref}\cdot\left(s_{ref,in} - s_{ref,out}\right)\right] \tag{6.1}$$

The magnitude of the first term, which should be equal to zero, was found to be less than 0.2% of the total exergy loss for typical operating conditions.

6.2 Separation of the Evaporator Irreversibility Components

In order to gain a better understanding of the changes in the total exchanger irreversibility with different coil designs, an effort was made to identify its various components. The approach chosen differed from that of earlier studies, in that the total irreversibility was not calculated by adding several independent terms, each one associated with a certain source of irreversibility. The net exergy loss within the exchanger, resulting from several irreversible processes, was based on the inlet and outlet conditions of all fluid streams. Following the convergence of the evaporator simulation, local variable information was used to estimate the magnitudes of the most significant irreversibilities. The sum of these contributions accounted for more than 90% of the total exchanger irreversibility in most cases.

6.2.1 Heat Transfer Irreversibilities

Irreversibilities due to heat transfer were calculated for each exchanger module, and summed to obtain the total heat transfer irreversibility contribution. The refrigerant within each module was assumed isothermal, at the mean refrigerant temperature, so that all heat transfer irreversibilities were produced within the air stream [1]. Figure 6.2 shows the control volume used to evaluate the heat transfer irreversibilities for an arbitrary exchanger module.

The total evaporator heat transfer irreversibilities were calculated with,

$$\dot{S}_{g,\Delta T} = \sum_{j=1}^{N_{modules}} \dot{m}_{a,j} \frac{\left(e_{ai,j} - e_{ao,j}\right)}{T_0} + \left(1 - \frac{T_0}{\overline{T}_{r,j}}\right)\frac{-\dot{Q}_j}{T_0} \tag{6.2}$$

and were found to be the most significant contribution to the total irreversibility for typical operating and design parameters.

6.2.2 Refrigerant Pressure Drop Irreversibilities

Since the refrigerant side of each exchanger module was assumed well mixed and isothermal, any irreversibilities within the refrigerant stream were attributed to pressure drop effects. Additional irreversibilities, such as those associated with concentration gradients, were excluded from the analysis.

Figure 6.3 shows the control volume used to evaluate the refrigerant pressure drop irreversibilities for an arbitrary exchanger module. As in the case of the heat transfer irreversibility, the total refrigerant pressure drop contribution was obtained by adding those associated with each and every exchanger module.

$$\dot{S}_{g,\Delta P_{ref.}} = \sum_{j=1}^{N_{modules}} \dot{m}_{r,j} \frac{\left(e_{ri,j} - e_{ro,j}\right)}{T_0} + \left(1 - \frac{T_0}{\overline{T}_{r,j}}\right)\frac{\dot{Q}_j}{T_0} \tag{6.3}$$

6.2.3 Air Pressure Drop Irreversibilities

While a strong coupling existed between the refrigerant pressure drop and heat transfer mechanisms, that was not the case on the air side. Changes in air pressure from one exchanger row to the next were neglected during the model solution, and the total air pressure drop was calculated after its convergence. Hence, the air pressure drop could be treated as an independent process, as shown in Figure 6.4.

The total air pressure drop contribution was calculated with,

$$\dot{S}_{g,\Delta P_{air}} = \frac{\dot{m}_{a,ev}}{T_0}\left(e\left(p_{a,ei},h_{a,eo}\right) - e\left(p_{a,eo},h_{a,eo}\right)\right) \tag{6.4}$$

6.2.4 Air Mixing Irreversibilities

Mixing of two or more separate air streams occurs within the evaporator, both in between rows and at the exchanger outlet. In order to obtain the average air conditions at the exchanger outlet, adiabatic mixing of the air streams leaving each of the tubes located in the last exchanger row was assumed. Irreversibilities associated with this mixing process were calculated with the help of the control volume shown in Figure 6.5, to determine their order of magnitude relative to that of other irreversibilities.

The air mixing irreversibility at the outlet to the evaporator was calculated with,

$$\dot{S}_{g,mix_{air}} = \frac{1}{T_0}\left(\left(\sum_{j=1}^{N_{tubes,last\ row}} \dot{m}_{a,j}e_{ao,j}\right) - \dot{m}_{a,ev}e_{ao,ev}\right) \tag{6.5}$$

In general, this term was found to be negligible relative to its heat transfer and pressure drop counterparts. For this reason, additional irreversibilities, associated with internal air mixing between various rows of the exchanger, were excluded from the analysis.

6.3 Entropy Generation Dependence on Exchanger Dimensions

The sensitivity of the irreversibility function to the physical dimensions of the exchanger was tested by varying the internal tube diameter, while keeping the total frontal area, tube spacing, and tube wall thickness constant for a given evaporator circuitry and tube arrangement. Figure 6.6 summarizes the results obtained for dry operating conditions.

All evaporators had thirty-six tube passes, four rows, and a cross-counterflow refrigerant circuitry. Evaporator capacity and superheat level in all cases were 10.55 kW (3 tons or 36,000 Btu/hr) and 5.56 °C (10 °F) respectively.

As expected, the irreversibility contributions associated with refrigerant pressure drop increased with a decreasing tube diameter, whereas those associated with heat transfer showed the opposite trend. Below a critical tube diameter, however, the refrigerant pressure drop increased dramatically, eliminating any potential gains due to improved internal heat transfer coefficients.

Irreversibilities associated with the air pressure drop were also affected by the change in tube diameter, since for a constant exchanger frontal area this implied a reduction in the minimum free flow area.

6.4 Entropy Generation Dependence on Tube Arrangement

The performance of several evaporator coils with an increasing number of rows was investigated, using a baseline coil with two identical two-row, thirty-six tube, refrigerant circuits. The total number of tube passes was held constant while increasing the number of rows, to ensure that the material and manufacturing costs remained unchanged. Figure 6.7 describes the circuitries of exchanger coils with two, three, four, six, nine, and twelve rows. Tube and fin material and spacing remained unchanged in all six coils.

For a fair comparison of the first and second-law performance of different coil designs, it was important to ensure that they operate under similar conditions. Table 6.1 describes some of the types of comparisons considered.

Table 6.1 Performance Comparison among Different Coil Designs

Variable (s) Fixed	Variable (s) Adjusted	Comments
$\dot{Q}_e$	$\dot{m}_{a,e}$	Air mass flowrate constrained by fan characteristics
$\dot{Q}_e$	$P_{r,ei}$	Coils operating with different superheat levels
ΔT_{sh}	$P_{r,ei}$	Convergence problems for certain superheat values with a discretized model; coils operating with different exchanger loading
ΔT_{sh} & $\dot{Q}_e$	$P_{r,ei}$ & $\dot{m}_{r,e}$	Actual operation of an evaporator in a system with a thermostatic expansion device and a compressor designed for a given evaporator capacity [2]

All results presented in this section were obtained with the last criteria listed in Table 6.1, that is holding both evaporator capacity and superheat level constant. The main disadvantage of this approach was the increased level of complexity in the evaluation of the unknown variables. The first three cases of Table 6.1 were handled by the design mode of the model, described in Chapter 4, which is based on the Newton-Raphson method [3] to solve for the unknown operating variable (air mass flowrate or evaporator inlet refrigerant pressure). The residual equations corresponding to each of these cases are,

$$Case\ 1: \quad \dot{Q}_{e,set} - \dot{Q}_{e,mod}(\dot{m}_{a,e}) \overset{?}{=} 0 \tag{6.6}$$

$$Case\ 2: \quad \dot{Q}_{e,set} - \dot{Q}_{mod}(P_{r,ei}) \overset{?}{=} 0 \tag{6.7}$$

$$Case\ 3: \quad \Delta T_{sh,set} - \Delta T_{sh,mod}(P_{r,ei}) \overset{?}{=} 0 \tag{6.8}$$

An unsuccessful attempt was made to solve the fourth case with the Newton-Raphson method, with evaporator inlet refrigerant pressure and refrigerant mass flowrate as unknowns in the two coupled residual equations listed below,

$$\begin{aligned} \mathit{Case\ 4:}\quad & \dot{Q}_{e,set} - \dot{Q}_{e,mod}(P_{r,ei}, \dot{m}_{r,e}) \overset{?}{=} 0 \\ & \Delta T_{sh,set} - \Delta T_{sh,mod}(P_{r,ei}, \dot{m}_{r,e}) \overset{?}{=} 0 \end{aligned} \tag{6.9}$$

Due to the discretized nature of the model, there were combinations of evaporator capacity and superheat for which no exact solution existed. A Marquardt search routine written by VanderZee [4], which seeks to minimize a single objective function, was found to give better results. The objective function was based on both superheat and capacity error terms relative to set values, weighted in a manner similar to that chosen by Orth [5] in her analysis of condensers.

$$\begin{aligned} \mathit{Case\ 4:}\quad F_{obj} = 0.9 \cdot \left| \dot{Q}_{e,set} - \dot{Q}_{e,mod} \right| + \\ 0.1 \cdot \left| \Delta T_{sh,set} - \Delta T_{sh,mod} \right| \end{aligned} \tag{6.10}$$

The performance of the six coils described in Figure 6.7 was simulated for various dry and wet operating conditions. The resulting figures, summarized in Table 6.2, correspond to an air mass flowrate of 0.5675 kg/s (4500 lbm/hr), and a condenser refrigerant pressure of 1825.8 kPa (265 psi) with 5.56 °C (10 °F) of sub-cooling. All evaporators were assumed to operate in a system with an isenthalpic expansion device, such that the constant condenser pressure assumption corresponded to a constant refrigerant enthalpy at the evaporator inlet. This resulted in slightly different evaporator inlet qualities with a changing evaporator pressure, which along with a varying refrigerant mass flowrate contributed to variations in the refrigerant pressure drop.

Table 6.2 Performance Analysis of Various Coil Designs

Figure	**Refrigerant**	**Capacity**	**Superheat**	**Air Inlet Temperature**	**Air Inlet Humidity**
6.8	HCFC-22	10.55 kW (3 tons)	5.56 °C (10 °F)	32 °C (90 °F)	dry
6.9	HCFC-22	10.55 kW (3 tons)	5.56 °C (10 °F)	27 °C (80 °F)	50%
6.10	HFC-32/ 125/ 134a (23/25/52%)	10.55 kW (3 tons)	5.56 °C (10 °F)	27 °C (80 °F)	dry

Figure	Refrigerant	Capacity	Superheat	Air Inlet Temperature	Air Inlet Humidity
6.11	HFC-32/ 125/ 134a (23/25/52%)	10.55 kW (3 tons)	5.56 °C (10 °F)	27 °C (80 °F)	50%
6.12	HFC-32/ 125/ 134a (23/25/52%)	10.55 kW (3 tons)	5.56 °C (10 °F)	32 °C (90 °F)	dry
6.13	HFC-32/ 125/ 134a (23/25/52%)	10.55 kW (3 tons)	5.56 °C (10 °F)	32 °C (90 °F)	50%

The level of irreversibility is indicated by the lost work in the evaporator, which is plotted as a percentage of the total evaporator capacity. All coils were found to perform less irreversibly with the zeotropic refrigerant than with HCFC-22 for equivalent operating conditions, as seen by comparing Figures 6.8 and 6.12, and 6.9 and 6.11 respectively.

Two competing effects, air pressure drop and heat transfer, influenced the trend in the total exchanger irreversibility as the exchanger became deeper and produced an optimum design for each set of operating conditions. Even though heat transfer irreversibilities decreased with an increasing number of evaporator rows with both the pure and mixed refrigerants, that effect appeared to be slightly more pronounced with the mixed refrigerant. Eventually, as the number of rows exceeded its optimum value pushing the exchanger free flow area further down, air pressure drop become the dominant source of irreversibility.

When combined heat and mass transfer were present, the irreversibility function ceased to be a glide dominated phenomenon, but was also affected by the enhanced exchanger conductance due to the latent contribution to the air-side heat transfer coefficient. As shown in Figures 6.11 and 6.13, the optimum number of exchanger rows decreased in the presence of moisture removal, as a larger fraction of the total evaporator load was handled by those rows closest to the entering air stream [6].

6.5. Entropy Generation Dependence on Refrigerant Circuitry

Most of the irreversibility trends, observed for both pure and mixed refrigerants with varying tube arrangements, were controlled by the air side heat transfer and pressure drop dependence on the air Reynolds number. Both the air heat transfer coefficients and friction pressure drop increased as the coils become deeper, in response to the reduction in the minimum free flow area of the exchanger, and the associated increase in air Reynolds number (for a constant air mass flowrate). These results were supported by the theoretical observations that the total resistance to heat transfer was dominated by its air side component, and that friction effects were the major contributors to the total air pressure drop.

In addition to air side effects, the total exchanger irreversibility was also affected by reductions in the exchanger mean temperature differences associated with air to refrigerant temperature glide matching. In order to further isolate these effects, six coils with two, three, four, six, nine, and twelve rows (described in Figure 6.7), were evaluated with both pure cross-parallel and cross-counterflow refrigerant circuitry arrangements. All irreversibility results, summarized in Figure 6.14, correspond to dry operating conditions with an air inlet temperature of 27 °C (80 °F), and a total rate of heat transfer of 10.55 kW (3 tons or 36,000 Btu/hr). In addition, all refrigerant pressure drop contributions were neglected, and the refrigerant exit conditions were kept near saturation conditions.

Three types of exchanger operation may be identified for comparison from Figure 6.14. Refrigerant HCFC-22 was chosen as the baseline case, with an isothermal refrigerant temperature profile in the absence of both superheat and refrigerant pressure drop. In agreement with the sensitivity analysis on tube arrangement presented in the previous section, a minimum in the total irreversibility level was found for a given number of exchanger rows, as determined by the trade-off between air side heat transfer and pressure drop.

Exchanger performance with the isothermal pure refrigerant was independent of refrigerant circuitry, and slight discrepancies between the parallel and counterflow results may be attributed to the discretized nature of the model, as well as deviations from the imposed constant capacity constraint. With the zeotropic refrigerant, on the other hand, performance was found to be noticeably influenced by the direction of refrigerant flow. In the cross-counterflow case, the slopes of the air and refrigerant temperature glides were equal in sign, if not in magnitude. The associated reduction in mean temperature difference between the two fluids resulted in improved exchanger performance, as evidenced by the lower irreversibility levels, relative to those of HCFC-22.

When the zeotropic refrigerant was circuited in a cross-parallel flow fashion, however, the temperature glides of both fluids had opposite slopes, penalizing its performance. Thus, the best and worst possible cases of positive and negative zeotropic temperature glides were considered in this study, in addition to the no-glide HCFC-22 baseline case. As expected, the irreversibility levels obtained with the pure refrigerant were between those of the best and worst cases for every tube arrangement under consideration.

Another interesting observation was the slight increase in the difference between the irreversibility levels of the parallel and the counterflow cases for the mixed refrigerant with an increasing number of rows. As the evaporator became deeper, the cross-parallel and counterflow arrangements approached their pure parallel and counterflow limits.

6.6 Entropy Generation Dependence on Temperature Glide Matching

The analysis presented in the previous section highlighted the role of refrigerant temperature glide on irreversibility reduction. In all cases considered, however, the temperature glide of the air was much greater than that of the refrigerant. An effort was made to quantify the importance of air and refrigerant glide matching, by evaluating exchanger performance with the zeotropic refrigerant under operating conditions resulting in matched and unmatched fluid temperature glides.

Figure 6.15 summarizes the results of this study. The dry operation of two cross-counterflow evaporators, with three and six rows respectively, were simulated with constant capacity constraints of 10.55 kW (36,000 Btu/hr) and 2.64 kW (9,000 Btu/hr). The air inlet temperature and mass flowrate were kept at 27 °C (80 °F) and 0.5675 kg/s (4500 lb/hr), the refrigerant outlet conditions were kept near saturation, and the effects of refrigerant pressure drop were neglected.

In the absence of moisture removal, the high and low constant capacity constraints corresponded to high and low air temperature glides (for a constant air mass flowrate). Whereas for the 10.55 kW case the air glide was much higher than its refrigerant counterpart, both glides were of nearly the same magnitude for the 2.64 kW case. As expected, an increase in the number of exchanger rows resulted in a reduction in the heat transfer irreversibilities in both cases, mostly due to the reduction in the required mean temperature difference associated with the increased exchanger overall conductance.

An additional reduction in the mean temperature difference could be attributed to the ability of the refrigerant temperature glide to match that of the air, an effect which should become more significant as the glides of both fluids are not only of the same sign, but of the same slope as well. Even though the results of Figure 6.15 indicate a slightly improved sensitivity of the heat transfer irreversibility reduction to tube arrangement with improved fluid glide matching, the magnitude of that improvement was found to be very small.

It should be emphasized that Figure 6.15 compares the rate of change of the heat transfer irreversibilities. Their absolute magnitude did decrease with a decreasing constant capacity constraint, as the same heat transfer area was used to exchange less heat across a lower mean temperature difference. In addition, the significance of heat transfer irreversibilities as a percentage of the total evaporator irreversibilities was also reduced with a lower capacity constraint. For a constant air mass flowrate, air pressure drop became the dominant source of irreversibility with an increasing ratio of exchanger heat transfer area to exchanger capacity.

Figures 6.16a-e show the air and refrigerant temperature profiles corresponding to a moderate capacity constraint for the five cross-counterflow coils with two, three, four, six, and nine rows described in Figure 6.7. As expected, the mean temperature difference did decrease with an increasing number of rows, and an increasing refrigerant pressure.

6.7 Evaporator Irreversibility and System Performance

All the results presented in the preceding sections appeared to suggest the existence of an optimum evaporator design for a given set of operating conditions. A major assumption in the analysis, however, was the thermodynamic isolation of the evaporator from the rest of the air-conditioning system.

In order to better understand the correspondence between the optimization results obtained at the component level, and their implications in terms of system performance, all six coils described in Figure 6.7 were implemented in the system simulation presented in Chapter 4. The effect of a changing coil design on the pumping power requirements of both the compressor and the air fan, for fixed superheat and capacity levels under dry and wet operating conditions, are shown in Figure 6.17a-b. As the coils became deeper, improved glide matching allowed for higher refrigerant evaporating pressures, which for a fixed condenser pressure resulted in reduced compressor work. At the same time, the pumping power of the air fan did increase with an increasing air pressure drop.

The trade-off between the thermodynamic benefits and penalties of the compressor and the air fan, however, did not necessarily result in the same optimum coil design as predicted by the component analysis. System performance was determined by the irreversibility level of the entire system, requiring a closer look at the irreversibility trends of all components with a changing coil design, as well as to their interaction.

The effect of a changing evaporator tube arrangement on the lost work associated with both the evaporator and the compressor was evaluated for dry and wet operating conditions, and is presented in Figures 6.18a-b. As the number of rows increased, the evaporator lost work went through a minimum, associated with the trade-off between heat transfer and air pressure drop irreversibilities. For a fixed refrigerant condensing pressure, different refrigerant evaporator pressures and mass flowrates resulted in different compressor inlet and outlet states, and therefore different compressor irreversibilities. The operation of the compressor became less irreversible as it had to pump less refrigerant across a smaller pressure gap.

The drop in compressor lost work, observed for the same increase in the number of evaporator rows, is an indication of the unavoidable interaction between the irreversibility levels of various system components. This explains the difference between the theoretical evaporator and system performance trends observed for a changing evaporator design under dry operating conditions. In the presence of moisture removal, on the other hand, the constant capacity constraint resulted in a weaker dependence of refrigerant evaporating pressure on evaporator design. As a result, the change in compressor exergy loss with a changing evaporator design became less pronounced, leading to improved agreement between system and component performance predictions.

6.8 Summary

A design optimization study was conducted using the evaporator model described in Chapter 4 to evaluate the entropy generation function defined in Chapter 3. The ability of the model to accurately predict the fluid inlet and outlet conditions used in the evaluation of this function was confirmed with experimental data.

The relative magnitude of the various irreversibility components were quantified, in order to better understand changes in the overall exchanger irreversibility. Refrigerant pressure drop irreversibilities were found to depend strongly on tube diameter below a critical value of that parameter. In addition, the effects of tube arrangement on the generation function were investigated. The optimum number of exchanger rows was mainly controlled by the trade-off between air pressure drop and heat transfer irreversibilities, both dominated by air side effects.

A comparison of cross-parallel and counterflow refrigerant circuitries highlighted the effect of refrigerant temperature glide on exchanger performance. Slightly lower mean temperature differences were observed for operating conditions resulting in better matched temperature glides of the air and the zeotropic refrigerant streams.

Finally, the interaction between evaporator and compressor irreversibilities was considered, as part of an effort to understand the relationship between system and component performance. Whereas the general trends predicted by both sets of results were in agreement, a complete system exergy analysis was found to be necessary for the accurate selection of an optimum evaporator design.

6.9 References

1 Hurlburt, E., Personal Communication, 1994.
2 Bullard, C.W., Personal Communication, 1995.
3 Stoecker, W.F., *Design of Thermal Systems*, 3rd ed., McGraw-Hill Book Co., New York, 1984.
4 VanderZee, J, "Semi-Theoretical Steady-State and Transient Modeling of a Mobile Air Conditioning Condenser", M.S. Thesis, University of Illinois at Urbana-Champaign, 1993.
5 Orth, L.A., "Predicting Refrigerant Inventory of HFC 134a in Air-Cooled Condensers", M.S. Thesis, University of Illinois at Urbana-Champaign, 1993.
6 Hrnyak, P., Personal Communication, 1995.

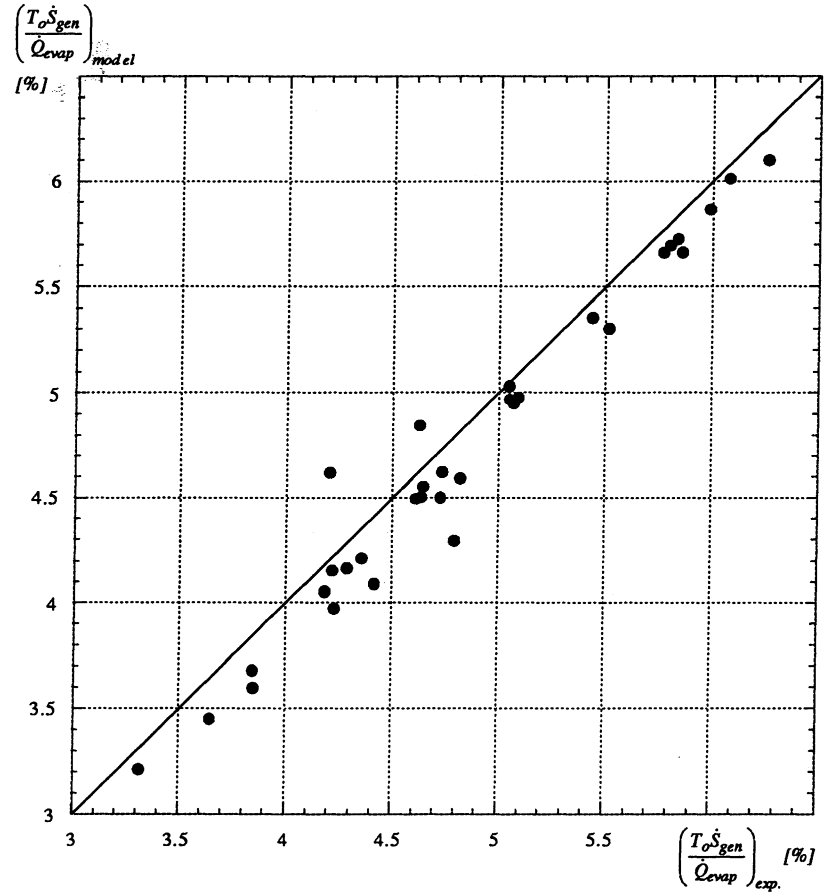

Figure 6.1 Theoretical and Experimental Net Entropy Generation as a Percentage of Total Evaporator Capacity for Coil A and HFC-32/HFC-125/HFC-134a (23/25/52%)

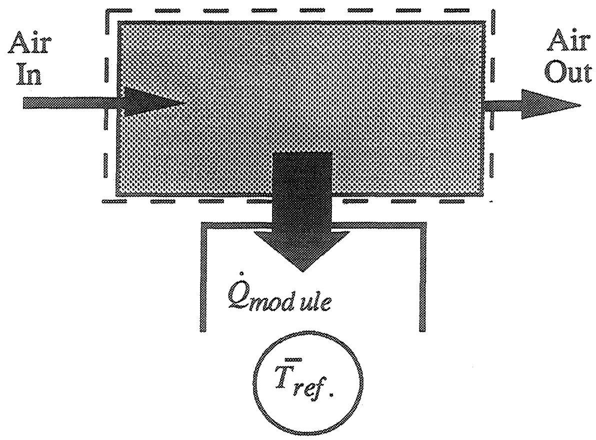

Figure 6.2 Irreversibilities due to Heat Transfer within an Exchanger Module

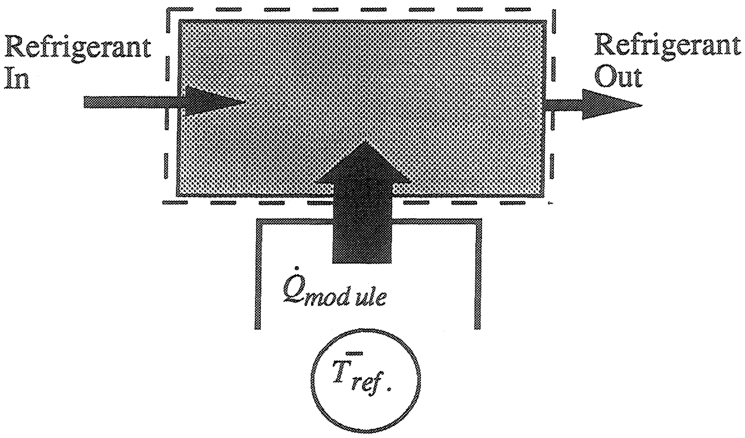

Figure 6.3 Irreversibilities due to Refrigerant Pressure Drop within an Exchanger Module

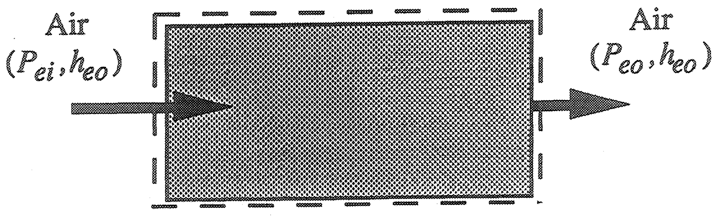

Figure 6.4 Irreversibilities due to Air Pressure Drop within the Evaporator

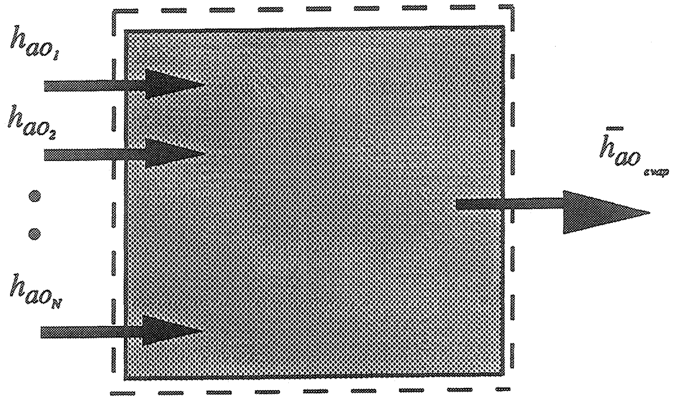

Figure 6.5 Irreversibilities due to Air Mixing at the Outlet to the Evaporator

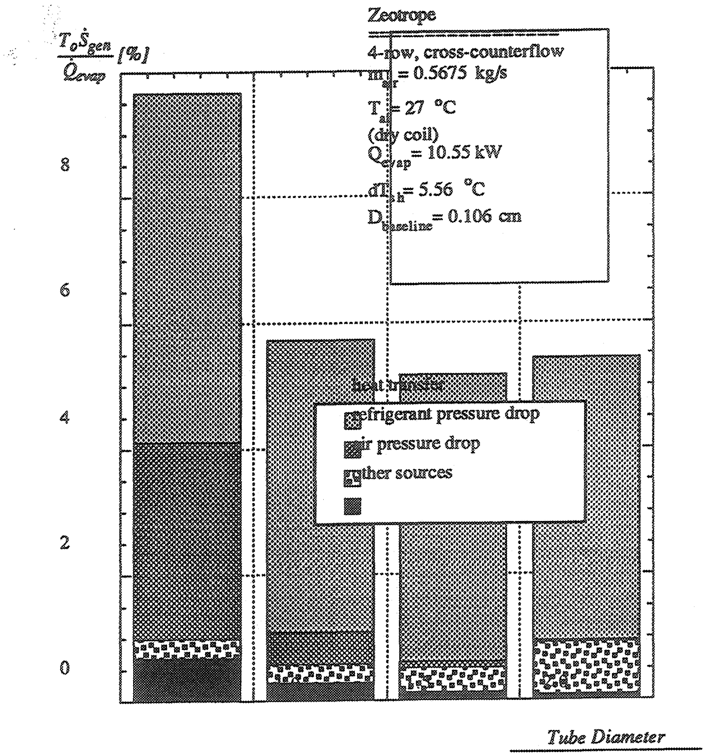

Figure 6.6 Effect of Tube Diameter on Evaporator Irreversibility for HFC-32/HFC-125/HFC-134a (23/25/52%)

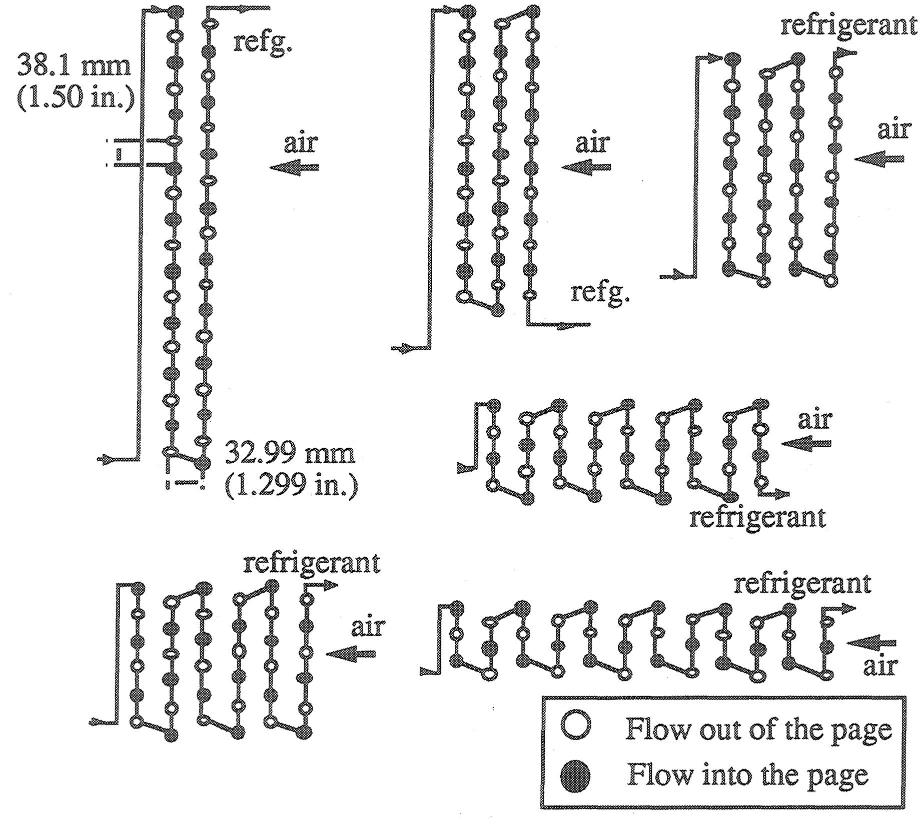

Figure 6.7 Circuitries of Cross-counterflow Evaporator Coils with 2, 3, 4, 6, 9, and 12 Rows

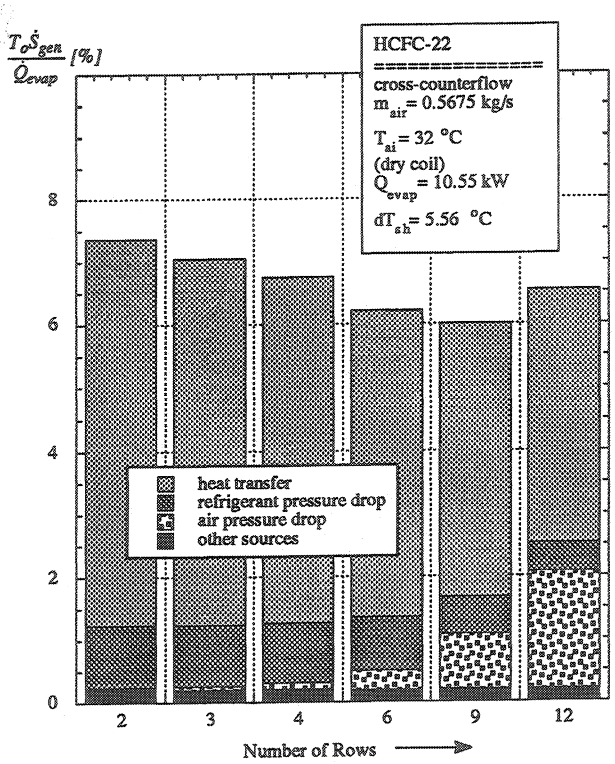

Figure 6.8 Effect of Tube Arrangement on Evaporator Irreversibility for HCFC-22

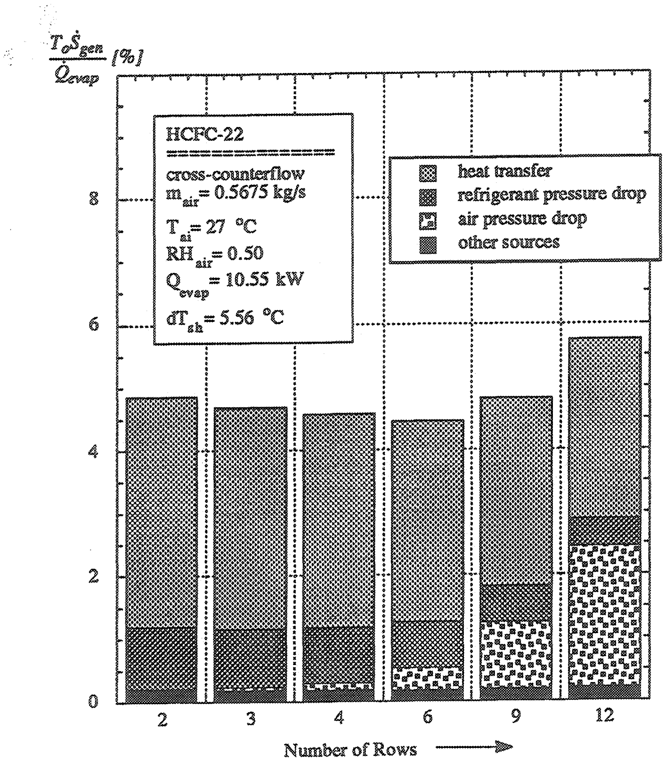

Figure 6.9 Effect of Tube Arrangement on Evaporator Irreversibility for HCFC-22

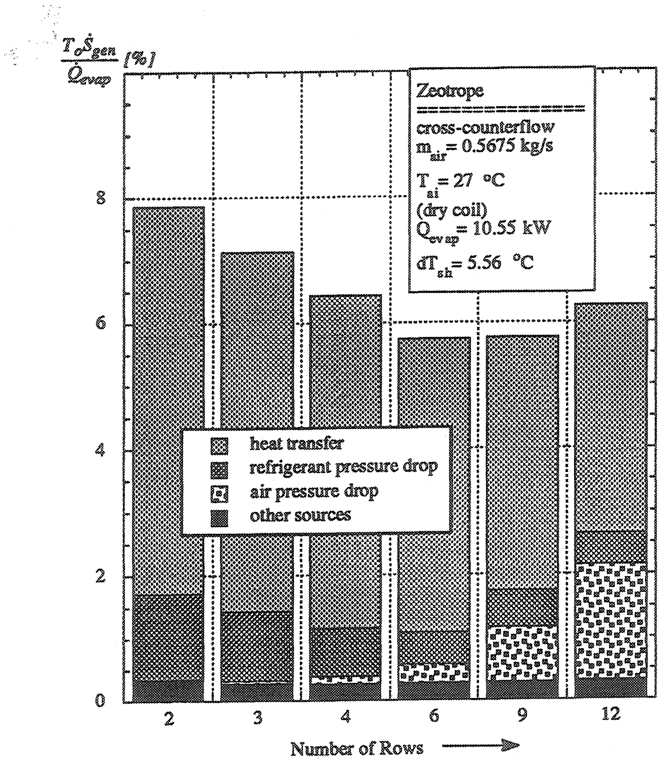

Figure 6.10 Effect of Tube Arrangement on Evaporator Irreversibility for HFC-32/HFC-125/HFC-134a (23/25/52%)

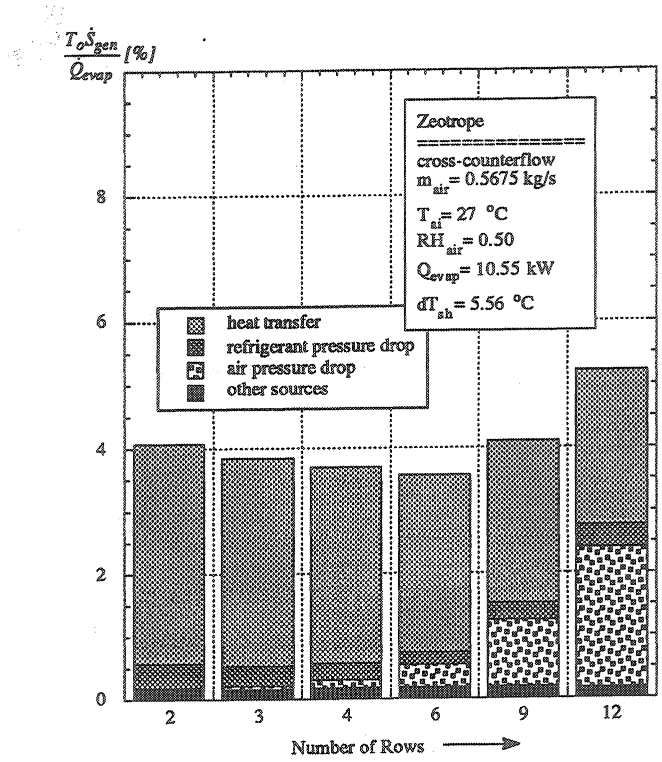

Figure 6.11 Effect of Tube Arrangement on Evaporator Irreversibility for HFC-32/HFC-125/HFC-134a (23/25/52%)

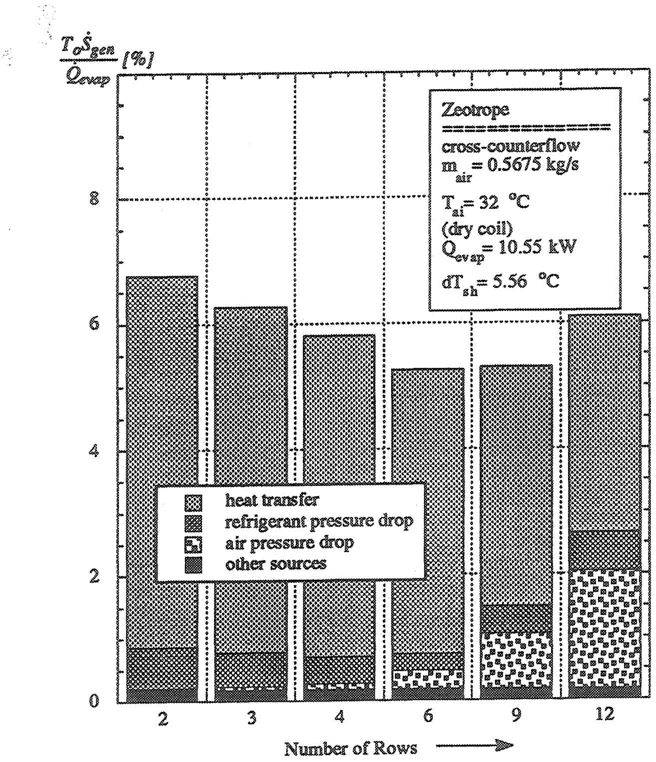

Figure 6.12 Effect of Tube Arrangement on Evaporator Irreversibility for HFC-32/HFC-125/HFC-134a (23/25/52%)

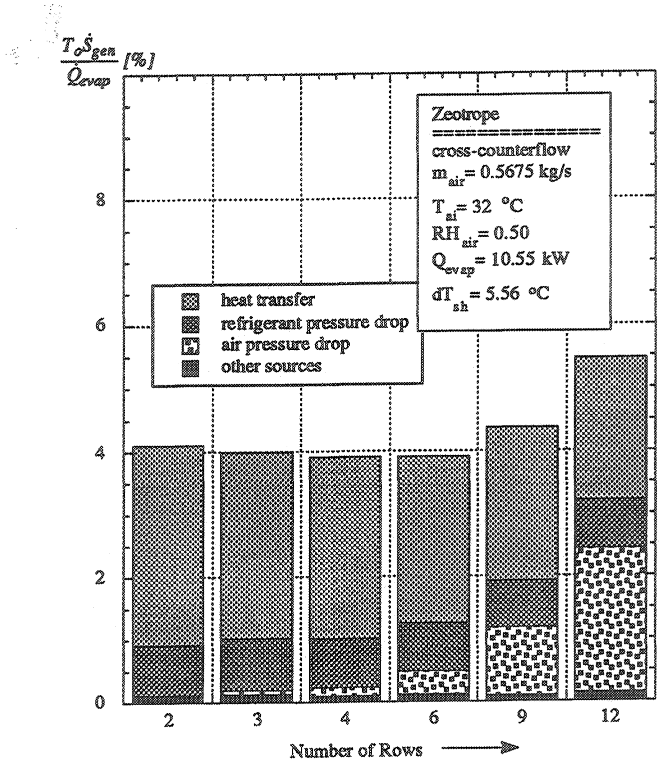

Figure 6.13 Effect of Tube Arrangement on Evaporator Irreversibility for HFC-32/HFC-125/HFC-134a (23/25/52%)

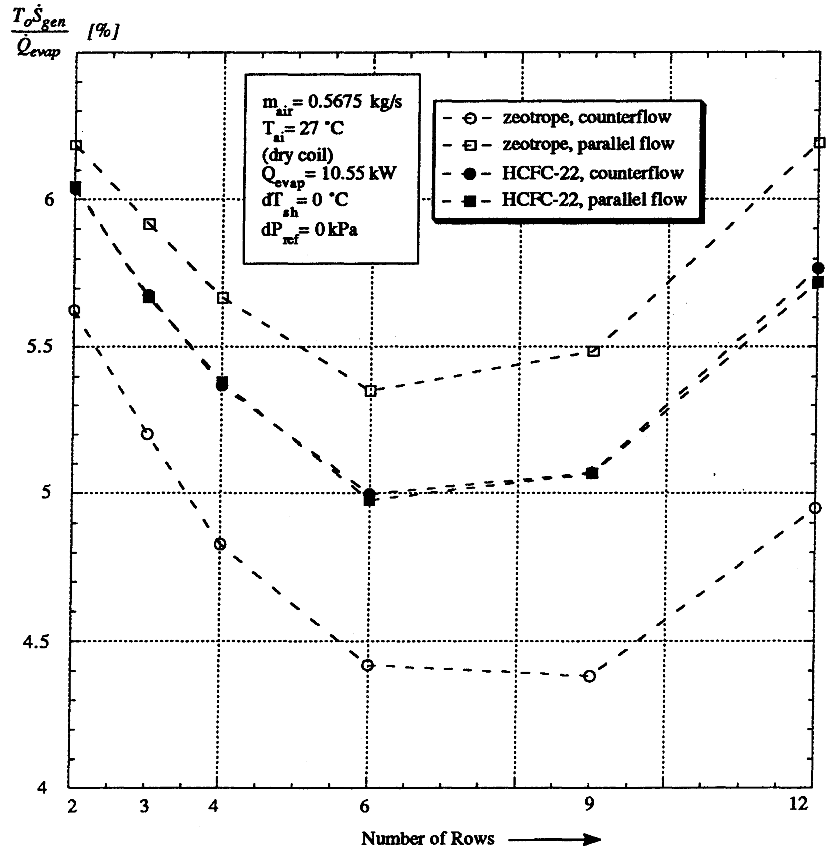

Figure 6.14 Effect of Refrigerant Circuitry on Evaporator Irreversibility for HCFC-22 and HFC-32/HFC-125/HFC-134a (23/25/52%)

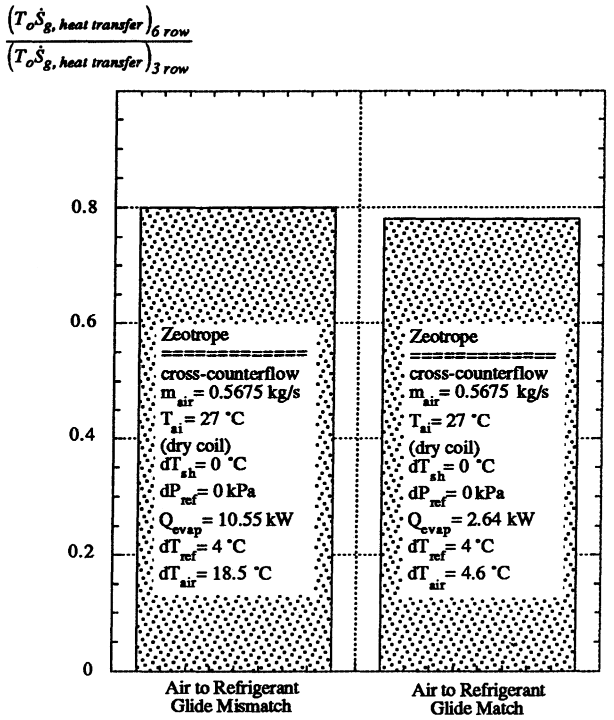

Figure 6.15 Effect of Air to Refrigerant Temperature Glide Matching on the Sensitivity of the Heat Transfer Irreversibilities to Tube Arrangement for HCF-32/HFC-125/HFC-134a (23/25/52%)

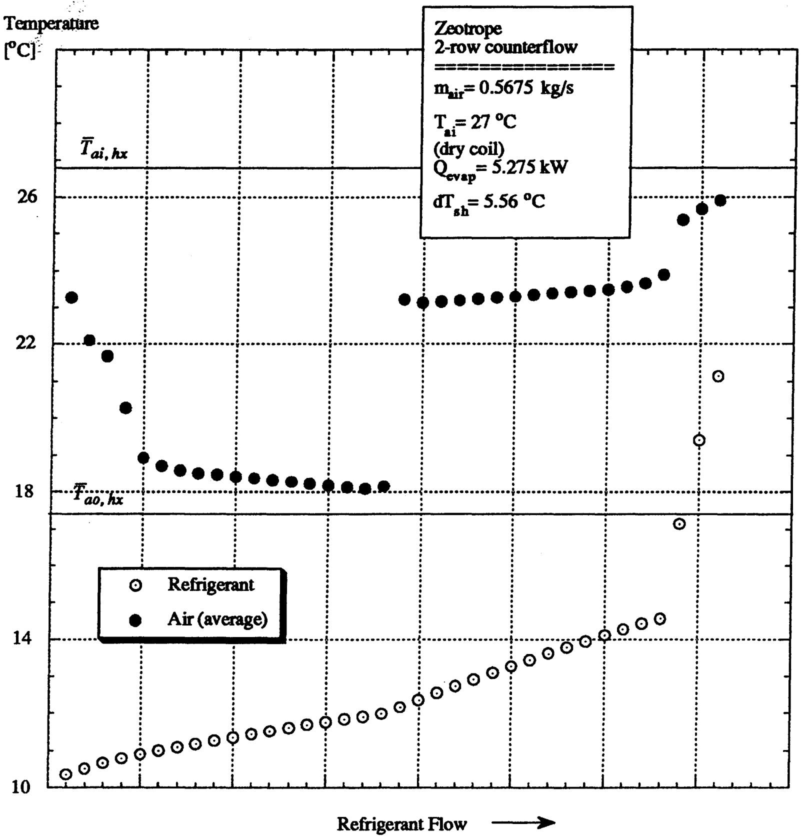

Figure 6.16a Air and Refrigerant Temperature Glides for a 2-Row Cross-Counterflow Dry Evaporator with HFC-32/HFC-125/HFC-134a (23/25/52%)

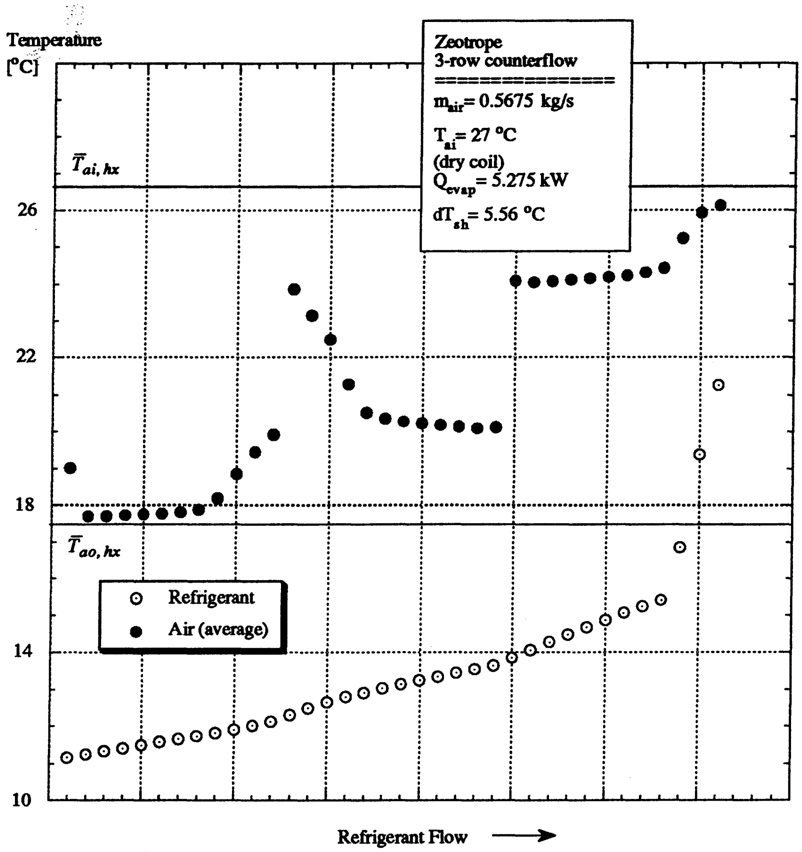

Figure 6.16b Air and Refrigerant Temperature Glides for a 3-Row Cross-Counterflow Dry Evaporator with HFC-32/HFC-125/HFC-134a (23/25/52%)

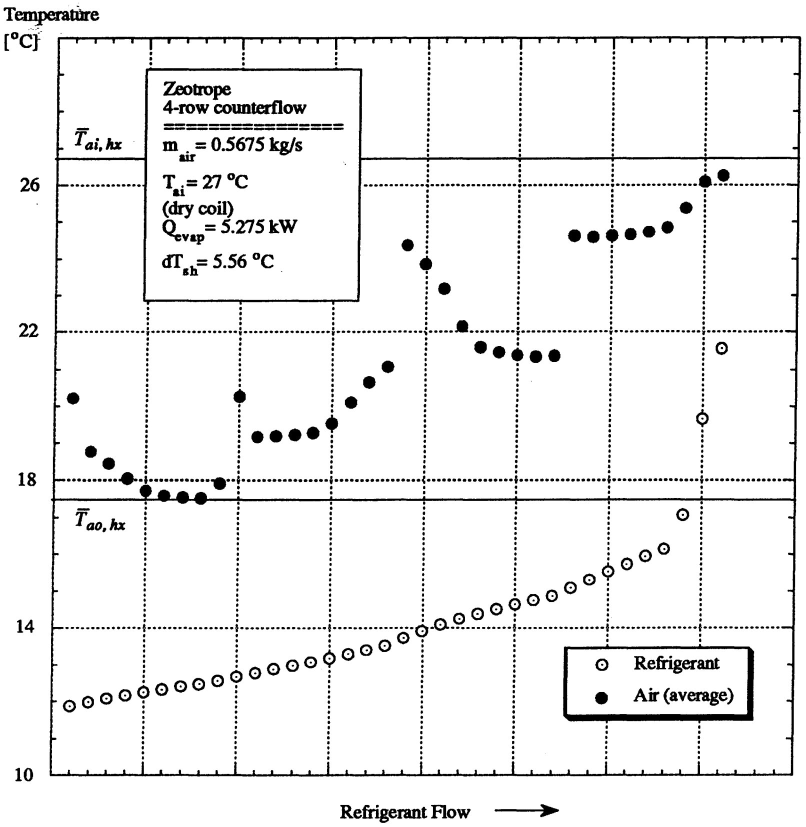

Figure 6.16c Air and Refrigerant Temperature Glides for a 4-Row Cross-Counterflow Dry Evaporator with HFC-32/HFC-125/HFC-134a (23/25/52%)

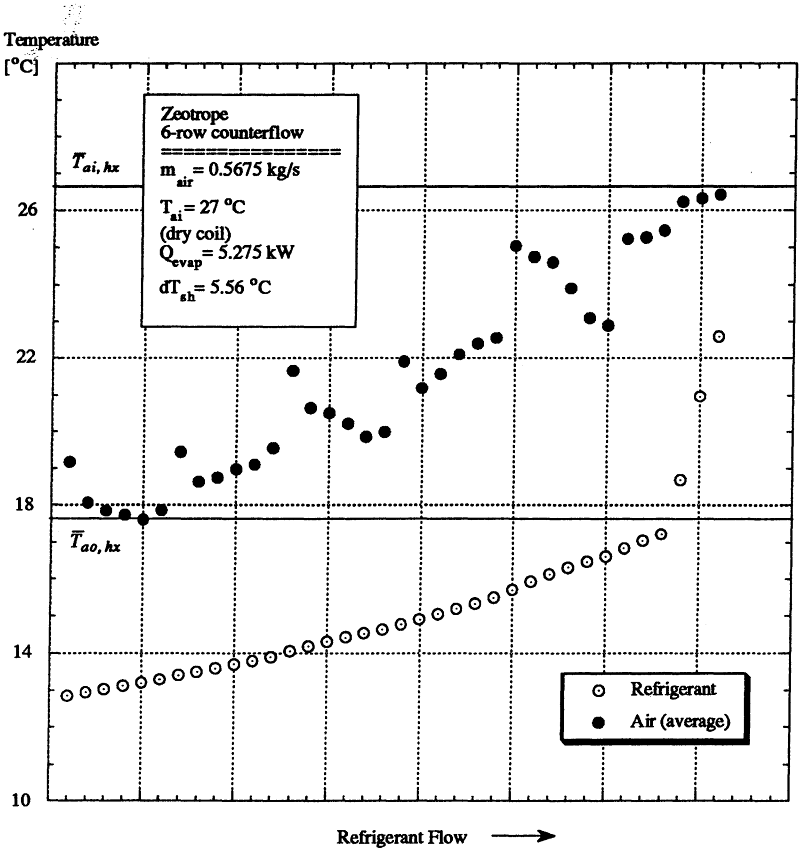

Figure 6.16d Air and Refrigerant Temperature Glides for a 6-Row Cross-Counterflow Dry Evaporator with HFC-32/HFC-125/HFC-134a (23/25/52%)

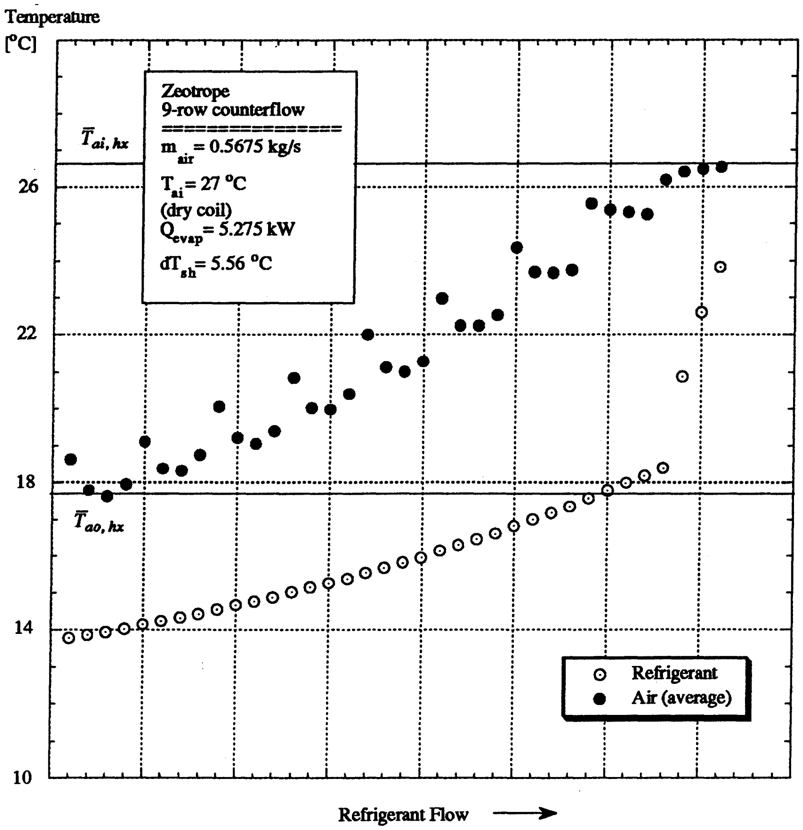

Figure 6.16e Air and Refrigerant Temperature Glides for a 9-Row Cross-Counterflow Dry Evaporator with HFC-32/HFC-125/HFC-134a (23/25/52%)

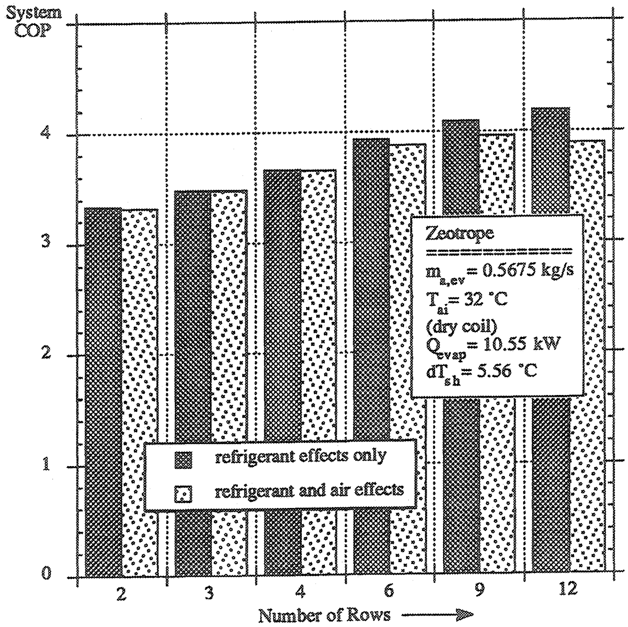

Figure 6.17a System Performance with and without Air Side Effects for Different Evaporator Designs with HFC-32/HFC-125/HFC-134a (23/25/52%)

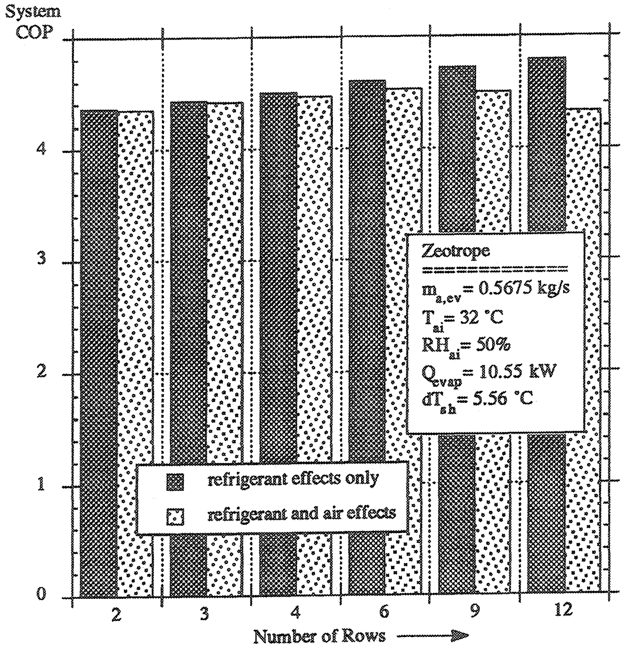

Figure 6.17b System Performance with and without Air Side Effects for Different Evaporator Designs with HFC-32/HFC-125/HFC-134a (23/25/52%)

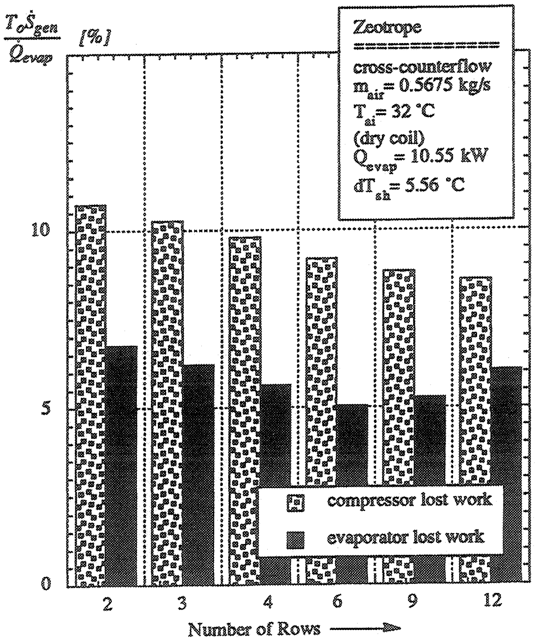

Figure 6.18a Evaporator and Compressor Lost Works for Dry Operation of Various Evaporator Designs with HFC-32/HFC-125/HFC-134a (23/25/52%)

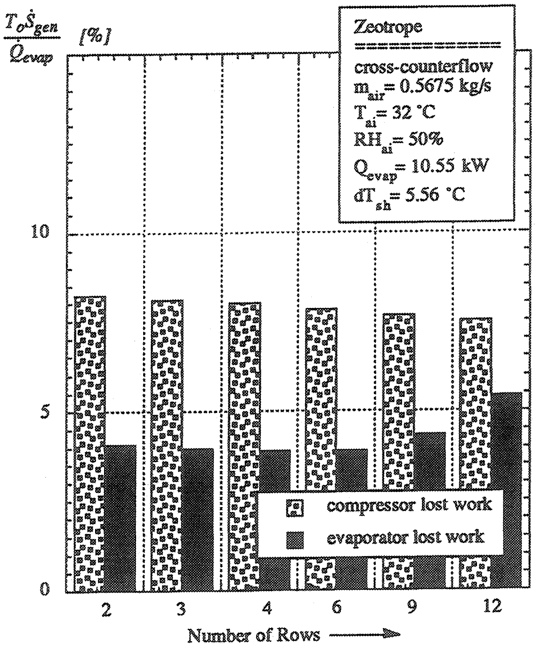

Figure 6.18b Evaporator and Compressor Lost Works for Wet Operation of Various Evaporator Designs with HFC-32/HFC-125/HFC-134a (23/25/52%)

CHAPTER 7

CONCLUSIONS AND RECOMMENDATIONS

This chapter summarizes the main results of this study. The first section reviews the project motivation, and its objectives. Next, the choice of a thermodynamic optimization methodology is reexamined.

The third section briefly summarizes the main features of the evaporator model developed as part of this study, as well as its experimental validation. Finally, the results of the optimization study are discussed, and their implications on future evaporator design with zeotropic refrigerants. The chapter concludes with suggestions for future work.

7.1. Motivation for the Study

The approaching phase-out of refrigerant HCFC-22, due to environmental concerns, has led to a search for its replacement by the air-conditioning industry. Zeotropic blends are favored among the possible substitutes because, in addition to having low *ODP* and *GWP*, they also experience a variable temperature glide during an isobaric phase change which could improve cycle efficiency.

This project was conducted in order to investigate the effect of evaporator design changes on its performance, using an irreversibility-based function to quantify the penalties associated with various designs. A computer simulation of the evaporator was developed as part of this study, to evaluate the irreversibility function under various operating conditions and exchanger designs. Several combined heat and mass transfer models were implemented in the simulation program, and experimental data was collected with two different coil designs, with pure and mixed refrigerants, in order to validate the model predictions.

7.2. Exchanger Thermodynamic Optimization

The thermodynamic performance of heat exchangers was evaluated based on an irreversibility analysis. The level of irreversibility in this and all other components of an air-conditioning cycle is important, because of its effect on system performance.

A methodology was proposed for the design optimization of evaporators with gliding refrigerants, operating with combined heat and mass transfer. It was used to determine the effect of various design changes on the thermodynamic performance of the evaporator, as well as that of other components, and of the full system.

7.3. Evaporator Model

An evaporator simulation program was developed to evaluate the irreversibility objective function, used to quantify exchanger performance. Three combined heat and mass transfer models (*discretized differential equations*, *thermal resistance*, and *equivalent effectiveness*) were implemented in the simulation, and their results were validated with experimental data collected with both pure and mixed refrigerants.

All three models were in good agreement in their prediction of the total rate of heat transfer, under both dry and wet operating conditions. In the presence of moisture removal, however, only the *discretized differential equations* model was found to properly account for the sensible heat ratio. Further testing of the *equivalent effectiveness* model, developed as part of this study, is recommended to determine its applicability to arbitrary exchanger designs.

7.4. Optimization Results

A design optimization study was conducted using the evaporator model to compare the thermodynamic performance of various evaporator designs. The accuracy of the model predictions in terms of the fluid inlet and outlet conditions was found to be sufficient for the evaluation of the objective function, as confirmed by experimental data.

The relative magnitudes of the various irreversibility components were quantified, in order to better understand trends in the overall exchanger irreversibility, and the sensitivity of exchanger performance to multiple design and operating parameters was investigated. Some of the most significant observations are summarized below.

[1] Under typical operating conditions, heat transfer was the dominant source of irreversibility for the two evaporators used in the experimental validation.

[2] The trade-off between heat transfer and refrigerant pressure drop irreversibilities, corresponding to improved refrigerant side heat transfer coefficients and increased refrigerant pressure drop with a decreasing tube inside diameter, became dominated by a sudden increase in refrigerant pressure drop irreversibilities below a critical tube diameter.

[3] Air pressure drop irreversibilities increased drastically with air velocity, indicating the impracticality of increasing exchanger rows beyond a certain number.

[4] The pure refrigerant was consistently more irreversible than its zeotropic replacement, for all capacity and superheat levels considered.

[5] As a constant number of exchanger tubes were rearranged to increase the number of exchanger rows, trends in the irreversibility function were dominated by air side effects. The trade-off between improved air heat transfer coefficients, due to higher air velocities, and increased air friction pressure drop, resulted in an optimum number of exchanger rows.

[6] The optimum number of rows was dependent on the operating conditions. In the presence of moisture removal, the optimum number of rows was lower than for otherwise similar dry conditions.

[7] For a given set of air operating conditions, the same rate of heat transfer was transferred more reversible in the absence of superheat.

[8] For fixed air side conditions, (i.e. a given air mass flowrate and evaporator tube arrangement), the level of irreversibility was independent of refrigerant circuitry for the pure refrigerant (in the absence of superheat and refrigerant pressure drop).

[9] Under similar conditions, the zeotropic mixture was more and less irreversible than the pure refrigerant with cross-parallel and cross-counterflow refrigerant circuitries respectively. The influence of refrigerant circuitry became slightly more pronounced with an increasing number of rows.

[10] Perfect matching of the slope of the air and refrigerant temperature glides did not appear to be necessary, since it had a smaller effect than the reduction of mean temperature difference through increased heat transfer coefficients. Further, given the realities of superheated evaporator exit conditions, and wet coils, it is not possible to match slopes over the whole range of conditions. Evaporators operating with the zeotropic mixture were slightly more responsive to tube arrangement when air to refrigerant temperature glides were matched, rather than unmatched.

[11] Improvements in the thermodynamic efficiency of the evaporator due to reductions in heat transfer irreversibilities were accompanied by similar reductions in the air to refrigerant mean temperature difference.

[12] Reductions in the lost work of the evaporator, small relative to the magnitude of the total evaporator rate of heat transfer, resulted in noticeable improvements in the system coefficient of performance.

[13] Reductions in the heat transfer irreversibilities of the evaporator were matched by similar reductions in compressor irreversibilities. This interaction between the thermodynamic efficiency of various components had two effects. First, it resulted in system performance gains greater than those predicted by the component analysis alone. In addition, such interaction explained the discrepancy between system and component results in terms of identifying an optimum evaporator design.

7.5. Future Work

Two main objectives were accomplished with this study. First, a computer simulation was developed to accurately predict the heat transfer and pressure drop performance of evaporators of arbitrary geometric characteristics operating with both pure and mixed refrigerants, and with combined heat and mass transfer.

In addition, a methodology was implemented to quantify the thermodynamic performance of evaporators. Whereas a first-law trade-off between heat transfer and pressure drop may be sufficient for the evaluation of some design modifications, such as internal tube enhancements, a second-law analysis provided a valuable measure of exchanger performance for other changes, such as refrigerant circuitry.

The final choice of an HCFC-22 replacement is yet to be made, and so a means to evaluate the maximum potential of each candidate through component design modifications is of great value. The following suggestions provide a guide for future work in this field.

[1] Expand the capabilities of the computer simulation to handle all potential HCFC-22 replacement refrigerants.

[2] Modify the approach used to separate the heat transfer and refrigerant pressure drop irreversibilities in order to handle high glide refrigerants.

[3] Develop detailed component models to investigate the effect of design changes on their respective exergy losses.

[4] Implement simpler component models into a full system simulation in order to gain a better understanding on the interaction between the irreversibility of various components, as well as between component irreversibilities and system performance.